Petrography and geochemistry of oceanic crust: Provenance of sedimentary detritus, Macquarie Island

Melissa Jean Murphy

Thesis submitted in partial fulfilment of the requirements for the degree of Bachelor of Science (Honours)

Department of Earth and Planetary Sciences
Division of Environmental Life Sciences
Macquarie University
June, 2008

Statement of Originality

All the work submitted in this thesis is the original work of the author except where otherwise acknowledged. No part of this thesis, in whole or in part, has been previously submitted to any other university or institution.

Melissa Jean Murphy
4th June, 2008

Acknowledgements

The past 10 months have been some of the most challenging and rewarding of my last five-and-a-half years of university, and without the knowledge, assistance and support from some truly exceptional people, I would never have completed this honours thesis.

First I would like to thank my supervisors - Dr. Nathan Daczko and Dr. Norm Pearson, whose doors were always open, and a seemingly unending supply of patience. Without their knowledge, and "cracking-of-the-whip", I would never have finished this project.

From commencement to completion of this project, I have received continual assistance and support from my room-mate, 'the sedimentology hotline' - Ryan Portner. From collection of samples, assistance with rock cutting and billet polishing, dreaded point counting, ARC-GIS and Adobe Illustrator, cultivating the geo-fantasies, and predicting weather patterns, Ryan has always made the time, for which I am so grateful.

This research was supported in part by grants from the Australian Research Council and the Australian and Antarctic Division. The research was conducted on GEMOC instrumentation. The research presented here was also fuelled in part by caffeine, in all its glorious forms – coffee, V, no-doz.

Throughout the course of this research, assistance has been provided by other individuals who are listed below, and is gratefully acknowledged: Steve Craven and Manal Bebbington, who provided assistance with preparation of polished thin- and thick-sections, and also Steve prepared my heavy mineral grain mounts and trained me in rock crushing techniques, thank you for being a good friend as well; Shelley Allchurch, who trained me in the preparation and digitising of my zircon grain mounts, and educated me on how to use the LA-ICP-MS and perform the data reduction of zircons; Peter Wieland, who unfailingly exchanged Ar gas bottles every time I used an instrument and assisted with GLITTER software. I would also like to Elena Belousova whose patience and insights have greatly contributed to my understanding of U-Pb geochronology and trace-element geochemistry. A big thanks to all of the academic

staff and fellow students and post-docs for their assistance, especially John and Christoph for Endnote tips.

On a personal note, I would like to thank: my science parents, Mary and Andrew Foldes, who have supported my scientific progress for many years now, Steve and Linda Mondy, Jean and Cliff McNeil, who likewise have supported me throughout my education; my mātua whāngai, Judy and Tima; the Goodwin family (especially James) – for support and the delicious meals; Chris McRae, for pushing me in the direction of research; Chris Walker – for keeping the dream alive; Dan and Sarah – for realigning my 'flafaccus'; my Castle Hill Rotarians (especially Jeff) for the flowers and kisses.

To all my good friends who have cheered me along the way; Lucinda, Nishen, Shelley, Chuck, Belinda, DJ Fez, Claire, Michael, Doug, Luke, Sarah, Sohnee, Anthony, Alexander, Palmy, B-man, Jay Dub, Chongy, Mic, Ajay, Jeff, Kev, and to those who I have failed to mention, thanks for your support.

I have saved my greatest appreciation for those closest to me. To my family, who may not have always understood what it is that I do, but have provided unconditional love and unwavering support, and have believed in me, despite rarely seeing me the past few months, and doubting whether I was still alive. A special thanks to Cio for getting me out of bed in the mornings.

To my beautiful best friend Jo Mondy, who has been there for me when it was easier to give up, and has listened to me moan and groan, and has now skipped the country in order to escape me and finally allowing me to get some work done.

Lastly, to Marty J Wilkins, for his long-suffering patience and being understanding beyond measure. Of those who have touched me, you have left a fingerprint on my heart. I Love you.

Mel

Abstract

Macquarie Island, located 1500 km southeast of Australia, is a sub-aerial exposure of Miocene oceanic crust/upper mantle situated within the oceanic basin in which it formed.

The seafloor spreading related 'Finch – Langdon fault' juxtaposes upper mantle serpentinised peridotites, gabbro and sheeted dolerite dykes in the northern quarter of the island with volcanic rocks (pillow basalts, tabular basalts, hyaloclastites and minor sedimentary rocks) that form the southern part of the island.

Interbedded within the extensive volcanic sequences are volcaniclastic sedimentary units containing gabbro and dolerite clasts, indicative that lower oceanic crust was exposed near the mid-ocean ridge during active volcanism.

Through a combination of petrography, major and trace-element clinopyroxene and zircon geochemistry, and U-Pb geochronology, this thesis investigates the provenance of the sedimentary units produced at an active mid-ocean ridge.

The high abundance of hydrothermal monomineralic clasts including chlorite, epidote, prehnite, quartz, carbonates and zeolites, and clasts of fault rock within the sedimentary rocks is consistent with a fault-scarp derived provenance. The unusually large volume of sedimentary rocks exposed on Macquarie Island suggests a large plate boundary scale transform fault is likely in order to produce the large volume of sediment. The long offset transform that links the Miocene 'A2/P2 – A4/P4' seafloor spreading corridor to the Australia-Antarctic-Pacific triple junction is the most proximal and therefore most likely source.

Detrital clinopyroxene major and trace-element geochemistry shows little overlap with clinopyroxene grains within the interbedded volcanic sequences, excluding the proximal volcanism as a likely source for the sediment. A lack of peridotite signature in clinopyroxene clasts suggests that it is likely that wasting of the nearby exposed or any other upper mantle provided very little (if any) input to the sediment. Overlapping clinopyroxene geochemical affinities between the gabbro and sheeted dolerite dyke sequences from Macquarie Island with the clinopyroxene clasts in the sedimentary rocks may suggest a lower crustal rock derived provenance.

U-Pb geochronology of detrital zircons yielded ages of ~27 Ma, which is *ca* 20 Ma older than published ages of the island. This demonstrates a significantly more distal provenance than has previously been proposed for these sedimentary rocks, and excludes the island as the source of the zircons. Overlapping detrital zircon REE patterns indicate the zircons in the sedimentary rocks from across the island were all derived from a similar oceanic rock type. The most proximal crust of the appropriate age is crust that formed at the South East Indian Ridge (SEIR) on the western side of the Australia-Pacific plate boundary. Furthermore, it is unlikely that the clinopyroxene clasts in the volcaniclastic sedimentary rocks of this study were derived from the exposed lower crust on Macquarie Island, given the total lack of zircons of appropriate age. Therefore it is likely that the clinopyroxene clasts were also derived from a fault scarp along a long offset transform that uplifted and exposed SEIR crust.

These results, combined with recently published paleogeographic reconstructions favour the SEIR crust as the most likely potential source area for the Macquarie Island volcaniclastic sandstones.

Key Words:

Macquarie Island, Mid-ocean ridge, Oceanic crust, Provenance, Clinopyroxene, Zircon

Abbreviations

BSE/CL: Back-Scattered Electron/ Cathodoluminescence

CHUR: Chondritic Unfractionated Reservoir

DM: Depleted Mantle

EMP: Electron Microprobe

GEMOC: Geochemical Evolution and Metallogeny of Continents

GLITTER: GEMOC Laser ICPMS Total Trace Element Reduction

HFS: High Field Strength elements (Zr, Ti, Y, Hf)

HREE: Heavy Rare Earth Elements (Gd – Lu)

LA-ICP-MS: Laser Ablation - Inductively Coupled Plasma - Mass Spectrometry

LILE: Large Ion Lithophile Elements (Rb, K, Ba, Sr)

LOI: Loss on ignition

LREE: Light Rare Earth Elements (La – Sm)

MORB: Mid Ocean Ridge Basalt

MRC: Macquarie Ridge Complex

MSWD: Mean Square Weighted Deviation

N.D.: Not Determined

PMSR: Proto-Macquarie Spreading Ridge

REE: Rare Earth Elements (La – Lu)

SEIR: South East Indian Ridge

Table of Contents

List of Tables

List of Figures

Chapter 1 Introduction

1.1 Geological Context

Ophiolites are recognised as fragments of oceanic crust, and have played a significant role in increasing our understanding of geological processes occurring at mid-ocean ridge environments. Studies of sedimentological processes in mid-ocean ridge environments have been limited by the many difficulties associated with deep-sea research, or are studies of highly deformed ophiolites that may lack direct tectonic context.

Associated with mid-ocean ridge environments is the deposition of pelagic, fault-derived volcaniclastic and volcanogenic sediments. Unlike other well-known and well-studied ophiolites (i.e. Cypress, Oman) that are emplaced on continental crust and have suffered inevitable deformation in the process, Macquarie Island represents an *in-situ* uplifted section of Miocene oceanic crust generated at the Proto-Macquarie Spreading Ridge (PMSR). This unique setting provides invaluable insight into the sedimentologic processes operating within mid-ocean ridges.

1.2 Review of previous studies on Macquarie Island

1.2.1 Regional Setting

Macquarie Island forms a subaerial exposure of the Macquarie Ridge Complex (MRC) (2000). The MRC consists of an irregular series of bathymetric troughs and ridges that are present along the boundary between the Australian and Pacific plates (Massell et al., 2000). Located approximately 1500 km southeast of Australia, (Figure 1.1) Macquarie Island consists of a series of tilted, faulted blocks exposing several partial sections of oceanic crust and upper mantle formed at the PMSR. The PMSR crust formed between ~40 – 6 Ma at a slow to intermediate (half rates of 4.4 – 28 mm yr^{-1}) spreading ridge system, and has been uplifted to its present location due to transpression between the Australian and Pacific plates (Daczko et al., 2003; Mosher and Massell-Symons, 2008).

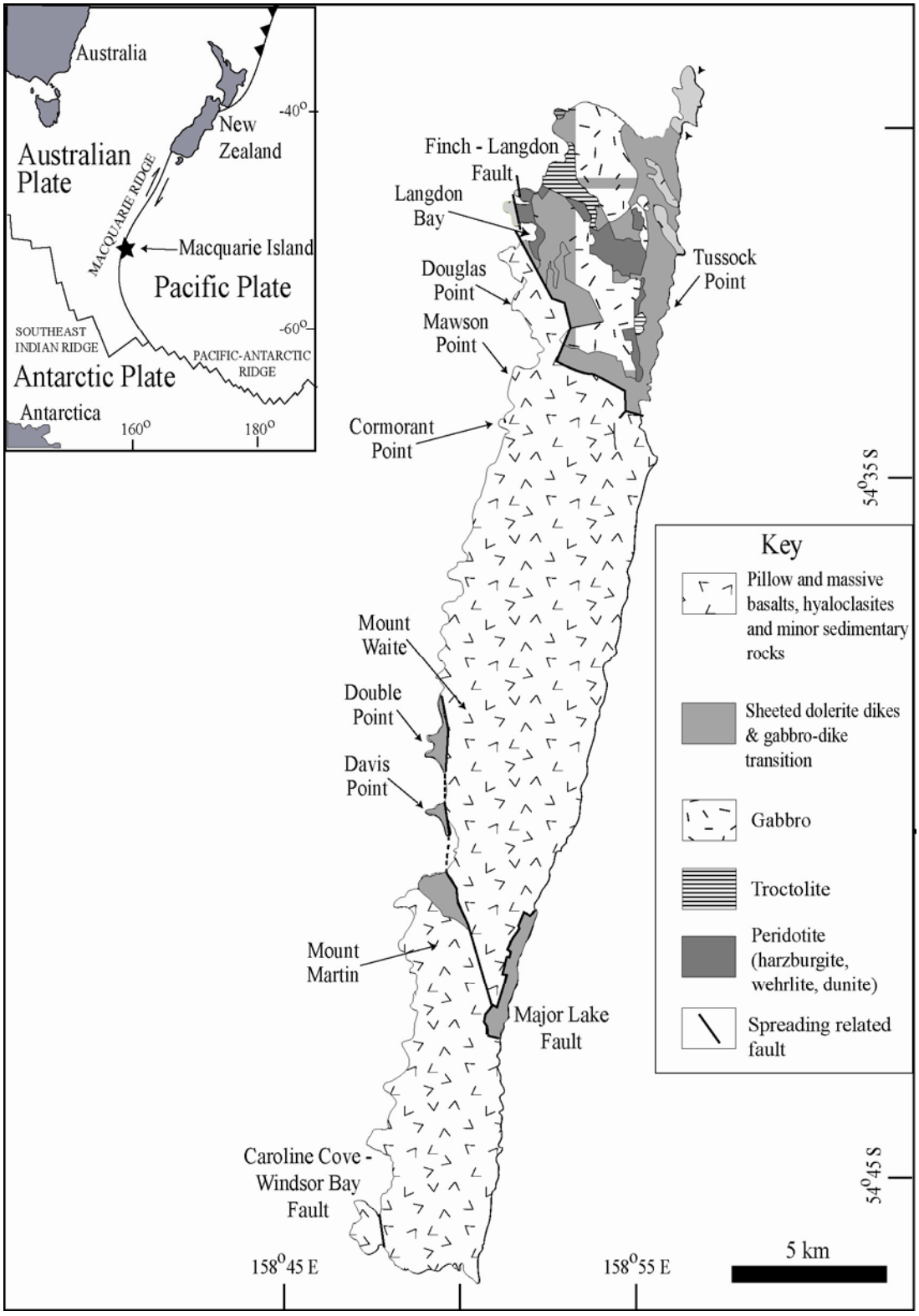

Figure 1.1 Generalised geological map of Macquarie Island, after Goscombe and Everard (1998). The seafloor spreading related 'Finch – Langdon fault' juxtaposes the serpentinised peridotite (harzburgite, wehrlite and dunite), gabbro and sheeted dolerite dykes that dominate the northwest quarter of the island with the volcanic rocks (pillow basalts, tabular basalts, hyaloclastites and minor sedimentary rocks) that form the southern part of the Island. Inset shows the location of Macquarie Island relative to the Australian–Pacific plate boundary, from Wertz (2003).

1.2.2 Regional Geology

The geology of Macquarie Island has been described in detail by several authors, most notably the petrology of the pillow basalt and sheeted dolerite by Griffin and Varne (1980); the age and distribution of the igneous rocks by Duncan and Varne (1988); and a more detailed geologic study was presented by Christodoulou et al. (1984). Most recently, the geology of Macquarie Island has been mapped at scales of 1:10,000 by Mineral Resources Tasmania and the Australian Antarctic Division (Goscombe and Everard, 1998).

Goscombe and Everard (1998) identified eight major rock associations on Macquarie Island, starting with upper mantle harzburgite at the base, which is overlain by a transitional association of dunite and harzburgite. Above lies plagioclase wehrlite, which gradually progresses through layered troctolite into a massive coarse-grained gabbro association. A transitional microgabbro association overlies the massive gabbro sequence, followed by a sheeted dolerite dyke sequence. Overlying is an extrusives and sediment association, consisting of extensive pillow basalt and tabular basalt sequences interbedded with hyaloclastites and minor sedimentary rocks which include volcaniclastic pebble and cobble breccia, sandstone, siltstone, limestone and rare chert.

Macquarie Island is dissected by pervasive faulting, both by older seafloor spreading related faults, and younger faults that formed during the transform motion and subsequent uplift of the island. The most significant of seafloor spreading related faults is the Finch – Langdon fault (see Figure 1.1), which juxtaposes serpentinised peridotite (harzburgite, wehrlite and dunite), gabbro and sheeted dolerite dykes that dominate the northwest quarter of the island with the volcanic rocks (pillow basalts, tabular basalt, hyaloclastites and minor sedimentary rocks) that form the southern three-quarters of the island.

Sedimentary rocks are rare on Macquarie Island, constituting less than 1 % of the geology. The greatest volume and highest density of sedimentary rocks exposed on Macquarie Island lie directly adjacent to the Finch – Langdon fault, and are interbedded with volcanic rocks. Some of the sedimentary rocks contain clasts of gabbro and dolerite, which indicate that lower oceanic crust was exposed at the mid-ocean ridge during active volcanism. The Major Lake fault shows less apparent throw, contrasting zeolite facies metamorphosed volcanic rocks and sheeted dolerite dykes at the north of the fault with lower greenschist facies rocks at the southern end of the fault. The Major

Lake fault is flanked by less extensive, but more laterally continuous, finer-grained sedimentary rocks than the Finch – Langdon fault. The shorter Caroline Cove – Windsor Bay fault segment juxtaposes greenschist facies metamorphosed volcanic rocks of the same crustal level, and adjacent sedimentary rocks within 500 m of the fault. Given the close proximity of the sandstones to the major seafloor spreading related faults, it has been suggested that the sandstones were produced by the physical disintegration and tectonic abrasion of oceanic crust in the adjacent fault zones (Daczko et al., 2005).

Other sedimentary rocks include rare hyaloclastic units, composed of medium to fine-grained glassy volcanic clasts.

1.2.3 Tectonic and Structural History

Three distinct tectonic phases are recognised on Macquarie Island. D_1 is characterised by north-south extension associated with the Proto-Macquarie Spreading Ridge (PMSR), and the initial crustal formation of Macquarie Island (Goscombe and Everard, 2001).

D_2 involved northeast-southwest extension at the PMSR. After volcanism and extension along the PMSR ceased about 5.9 Ma, D_3 dextral strike-slip transcurrent motion began, followed by ~200 km of dextral transpression at the Australian-Pacific plate boundary, which continues to the present day (Goscombe and Everard, 2001).

Paleogeographic reconstructions of the plate boundary created using the PLATES software at The University of Texas at Austin Institute for Geophysics from 33.3 Ma to the present day (Figure 1.2), adapted from Meckel (2003) show the relative movement of the Australian, Pacific and Antarctic plates. The reconstructions use the finite Euler rotation poles of Cande and Stock (2004). The figure shows a progressive rotation of the PMSR orientation from east-west extension to north-south extension between 33.3 Ma and 5.9 Ma. Transpression has dominated the Australian-Pacific plate boundary since approximately 5.9 Ma, however the initiation of transpression predates ~10.9 Ma along some segments of the plate boundary (Meckel et al., 2005).

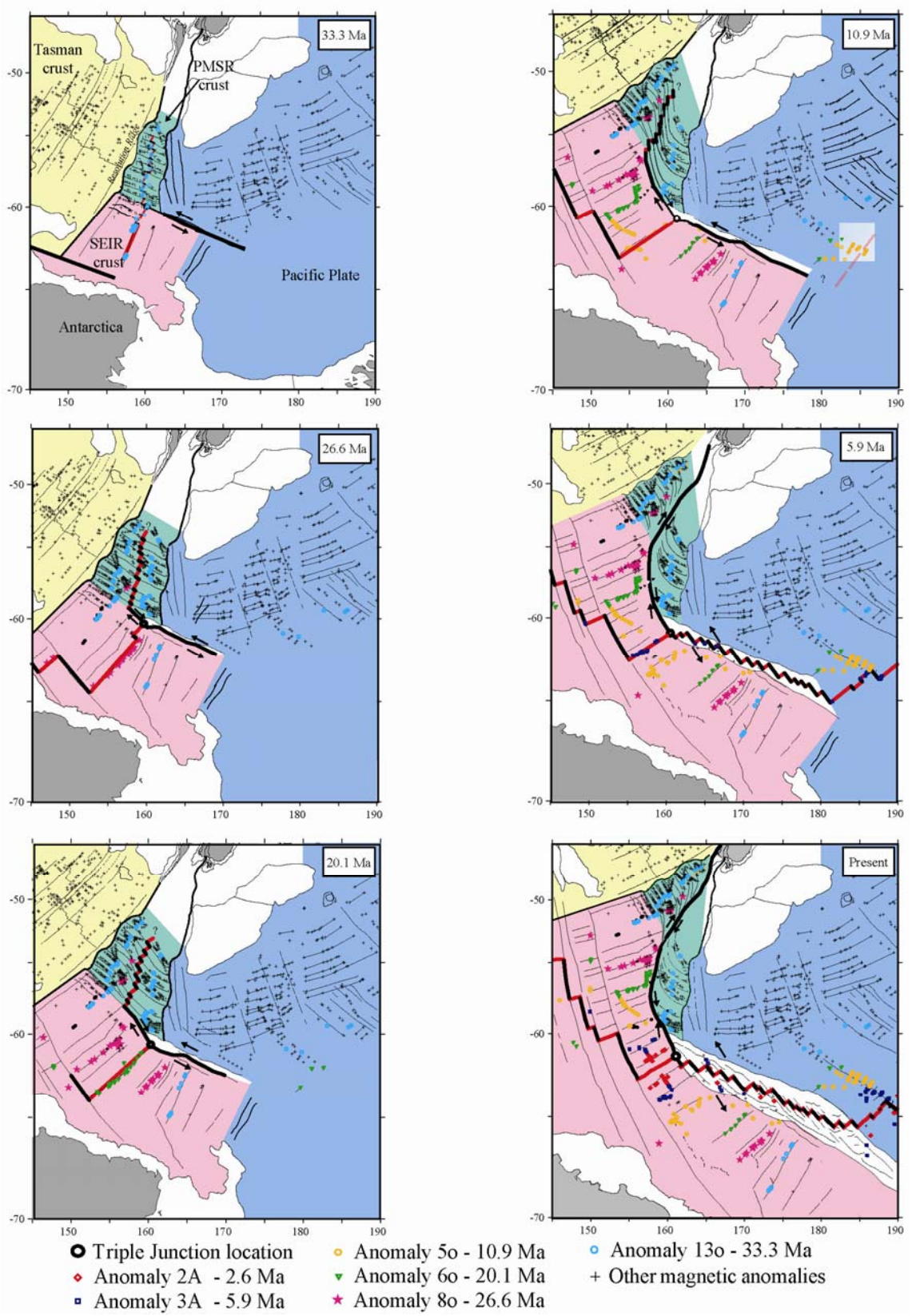

Figure 1.2 Paleogeographic reconstructions of the plate boundaries created using PLATES reconstruction software (University of Texas at Austin, Institute for Geophysics) and the Cande and Stock (2004) finite poles of rotation, adapted from Meckel, (2003). Pale yellow colour indicates crust created >52 Ma at the now extinct Tasman Sea spreading centre. Pink colour indicates crust formed at the presently active Southeast Indian Ridge SEIR. Blue shading represents crust formed at the Antarctic - Pacific spreading ridge. Green shading indicates crust formed at the PMSR. Black arrows indicate approximate relative plate motion.

1.2.4 Ages of Macquarie Island Rocks

There exists few radiometric ages for rocks from Macquarie Island that constrain the age of crust formation. Early K-Ar and $^{40}Ar/^{39}Ar$ ages determined by Duncan and Varne (1988) for basalts range from 9.7-11.5 Ma. An $^{40}Ar/^{39}Ar$ age of 6.1 ± 0.009 Ma was determined by Wertz (2003) for basaltic glass. Recent U-Pb isotopic dating of zircon grains separated from phlogopite pegmatoids yield ages of 8.4 ± 0.3, 8.5 ± 0.2 and 8.8 ± 0.2 Ma (Armstrong et al., 2004). Murphy et al. (2008) report detrital zircon ages from modern colluvium that range between approximately 7.5 to 9 Ma (n = 84), indicating a middle to late Miocene age for formation of Macquarie Island crust.

Microfossils identified within calcareous sediment interstitial to pillows include early to middle Miocene foraminifera and coccoliths (Varne et al., 1969; Quilty et al., 1973). Quilty et al. (1973) report *Globigerina bulloides*, *Globigerinoides trilobus*, *Neogloboquadrina pachyderma,* and *Coccolithus pelagicus*, which indicate a late Miocene or younger age, and tentatively identified *Reticulofenestra pseudoumbilica* that suggests a late Miocene to early Pliocene age for the samples. Recent studies by Quilty and Crundwell (2004) report ages from bolboform microfossils from within sediments intercalated with pillow lavas, with *Bolboforma metmacheri* ages of 8.78-9.01 Ma and *Bolboforma graciliriuclata* ages of 9.75-9.61 Ma that constrain the age of the seafloor spreading that formed the pillow lavas.

1.3 Provenance

Provenance analysis of sedimentary rocks aims to reconstruct the original source rock assemblages, and assist with determining the conditions and specific tectonic setting of the source terrain. Early provenance analysis concentrated on modal point count analysis of detrital frame-work grains (Dickinson and Suczek, 1979) or whole-rock geochemistry (Bhatia and Crook, 1986) to constrain the provenance and tectonic setting of sandstones. Single grain, heavy mineral analysis of minerals such as zircon, rutile, apatite, magnetite, tourmaline, clinopyroxene etc. are well established in provenance studies; however detailed provenance studies from ophiolite settings are particularly scarce (Garzanti et al., 1998; 2000; 2002 and references therein)

Sandstone compositions are primarily controlled by the composition of the source rocks, and modification by processes such as transport, deposition, diagenesis and alteration (Morton and Hallsworth, 1994; 1999). Despite these processes, detrital

heavy minerals such as zircon, and to a lesser extent clinopyroxene, tend to preserve their primary compositions, reflecting the source rock lithology, and are useful as provenance indicator minerals.

The importance of both clinopyroxene and zircon as provenance indicator minerals lies in their tendency to preferentially incorporate selected major and trace-elements into their crystal structure. Clinopyroxene is common in many rock types, (particularly oceanic crust). Clinopyroxene has chemical compositions that reflect its petrogenesis, has a relatively high degree of resistance to chemical and mechanical weathering, and is stable through diagenesis and low grade metamorphism (Cawood, 1983; Beccaluva et al., 1989; Krawinkel et al., 1999). Similarly, zircon is a widespread heavy mineral in many sediments and sedimentary rocks owing to their chemical and mechanical resistance; they commonly survive weathering, sedimentary processes, high temperature metamorphism and anatexis (Belousova et al., 2001; 2002). Characterisation of major and trace-elements within detrital clinopyroxene and zircon may allow for the identification of the source lithology, and provide information on the tectonic origin of the source. Similarly, the propensity of zircon to incorporate radionuclides into their crystal structure allows for U-Pb dating of detrital zircons, providing a constraint on the age of the source lithology.

1.4 Project Aims and Objectives

This study focuses on determining volcaniclastic sandstone provenance on Macquarie Island. The individual objectives of this project are outlined below:

1. To establish the lithostratigraphic relationships between igneous rocks and interbedded sedimentary rocks, and correlate marker horizons within several stratigraphic sections using petrography and geochemistry.
2. To characterise the major and trace-element compositions of clinopyroxene grains within representative igneous rocks and sedimentary rocks on Macquarie Island.
3. To constrain the age and type of crust for the source of the sandstones using U-Pb geochronology and trace-element geochemistry of detrital zircons.
4. To develop a provenance model that is consistent with the tectonic setting at the time of sandstone deposition.

1.5 Thesis Overview

This thesis has been structured into five chapters and six appendices. Chapter 2 describes the stratigraphic context and petrography of the samples selected for this study, and presents whole-rock major element data from seven igneous rocks. The lithostratigraphic relationships between the igneous rocks and interbedded sedimentary rocks are also discussed. Chapter 3 describes the analytical methods and presents the major and trace-element geochemistry of both igneous and detrital clinopyroxene grains. Chapter 4 describes the analytical methods and presents the major and trace-element geochemistry, and U-Pb ages for detrital zircons. The final chapter incorporates all these datasets into a provenance model, summarises the conclusions of this study and provides suggestions for future work.

Chapter 2 Stratigraphy and Petrography

2.1 Introduction

This study primarily focuses on three sites along the west coast that contain laterally continuous sedimentary rocks: (i) Davis Point (sample prefix: DVP-); (ii) Double Point (DLP-); and (iii) Mount Waite (MW-). These units are interbedded with volcanic rocks and are proximal to the seafloor spreading related Major Lake fault (Figure 1.1).

Detailed basalt lithology is used to understand the stratigraphic relationships between samples (Figure 2.1). A comparison of the mineral geochemistry of igneous clinopyroxene grains and detrital clinopyroxene clasts within these units is used to test if the volcanic rocks are a potential source for the interbedded sedimentary rocks. Additionally, samples of igneous and sedimentary rocks from elsewhere on Macquarie Island have also been analysed in order to compare the igneous and detrital clinopyroxene and zircon geochemical affinities with samples from the detailed west coast section.

Samples used in this study with a numerical prefix (e.g. 0221O) were collected in the 2001-2002 summer field season by Nathan Daczko of Macquarie University, Sydney; all other samples were collected in the 2006 and 2007 summer seasons by Ryan Portner of Macquarie University, Sydney. After careful petrographic examination of the samples, 32 of the least altered samples were chosen for analysis by electron microprobe (EMP) owing to the presence of relatively unaltered clinopyroxene grains. Six of these samples were selected for detailed trace-element analysis by Laser Ablation – Inductively Coupled Plasma – Mass Spectrometry (LA-ICP-MS). Mineralogical compositions were determined by reflected and transmitted light microscopy using a Nikon Eclipse E400 POL binocular microscope, and supplemented by electron microscopy.

Seven igneous samples from the detailed section were selected for whole-rock major and trace-element analysis by X-Ray Fluorescence (XRF). The samples exhibit zeolite facies metamorphism. Three dolerite hypabyssal sills were selected for analysis, two from Davis Point (DVP1-13, DVP2-3) and one from Double Point (DLP4b-2). Similarly, four basaltic samples were selected: one tabular basalt each from Davis Point

and Double Point (DVP-1-11, DLP3-11) and two pillow basalts from Mount Waite (MW4-3, MW4-6b).

The following notations are used to describe the vesicularity: 'non-vesicular' (<1 %), 'sparsely vesicular' (1–5 %), 'moderately vesicular' (5–20 %) and 'highly vesicular' (>20 %). The abundance of phenocrysts is denoted by the terms: 'aphyric' (phenocryst content is <1 %), 'sparsely phyric' (1–5 %), 'moderately phyric' (5–20 %) and highly phyric (>20 %).

Grain sizes are given by: mudstone (<256 μm) silt (63 to 256 μm), very fine sand (63 to 125 μm), fine sand (125 to 250 μm), medium sand (250 to 500 μm), coarse sand (500 to 1000 μm), very coarse sand (1 to 2 mm), pebbles (2 to 64 mm), cobbles (64 to 256 mm) and boulders (>256 mm). Colours used in the description below are from the Munsell rock-colour chart (Geological Society of America).

2.2 Davis Point

2.2.1 Stratigraphy

The Davis Point section has the greatest vertical extent (~250 m), and contains pillow basalt and tabular basalt which is interbedded with conglomerate, hyaloclastite breccia, fine- to medium-grained sandstone and mudstone, cut by late stage, columnar jointed dolerite dykes. Bedding attitude decreases up section from 16˚ to 28˚, with the steepest dips found adjacent to faults. The single conglomerate layer is approximately 0.5 m thick, framework supported, and composed of pebble- to cobble-sized gabbro, dolerite and basalt clasts, gradually thinning to muddy sandstone. Sandstone units are medium- to coarse-grained, normally graded with fine sandstone and mudstone laminations, and commonly exhibit ripple marks at the top of units. The sandstone units vary from ~1 m thick at the base of the beds, to approximately 1.5 – 2 m thick at the top of the beds. Moderate orange-pink sandy mudstone units commonly overly sandstone units, but are also found overlying pillow basalt or hyaloclastite units ranging from ~10 cm to 1 m in thickness. An ~5 m thick, columnar jointed unit of light grey, moderately plagioclase phyric tabular basalt with a trachytic texture is found in the middle of the Davis Point section. A second 14 m thick tabular basalt unit in the middle of the section is medium grey in colour, non-vesicular, moderately to highly plagioclase phyric, with columnar jointing at the bottom of the unit, and ropey corrugations at the top of the unit.

Figure 2.1 Lithostratigraphy and basalt marker horizon correlations between measured sections at Davis Point, Double Point and Mount Waite. Modified from unpublished work (Ryan Portner, pers. comm.).

The pillow basalts range from: (i) 10 m thick medium grey, aphyric to sparsely plagioclase phyric unit at the bottom of the section; (ii) 10 m thick light grey, highly plagioclase phyric; (iii) 48 m thick unit of medium light grey, moderately plagioclase phyric, sparsely vesicular; (iv) ~1 m dark grey, moderately to highly vesicular, sparsely plagioclase phyric with dark blue glassy chill margins; to (v) highly oxidised reddish-purple, highly plagioclase phyric and moderate vesicularity at the top of the section. Hyaloclastite is found overlying pillow basalt units with a sharp contact. Units range from a thin ~5 cm unit at the bottom of the section, to a 5 m unit at the middle. Clasts are cobble- sized angular fragments with a similar lithology to the underlying pillow basalts, and show varying degrees of matrix support.

2.2.2 Igneous Petrography

This study focussed on the igneous units from this sequence in order to correlate with the stratigraphic sections at Double Point and Mount Waite. Two dolerite hypabyssal sills were sampled for geochemical comparison of clinopyroxene within interbedded sedimentary sequences.

Two pillow basalt samples were collected from Davis Point. **DVP1-11** is a dark grey, moderately to highly vesicular, sparsely plagioclase phyric pillow basalt with dark blue glassy chill margins. It has a sub-variolitic texture, with radiating acicular, altered plagioclase laths, ranging from 10 μm to 2 mm, averaging 50-70 μm. The groundmass consists of volcanic glass pseudomorphed to yellow/brown palagonite, rare ~10 μm mauve subhedral clinopyroxene grains, nucleating along plagioclase grain boundaries, and very fine-grained opaque minerals. Vesicles are sub-rounded, and are filled with a white, radially fanning zeolite mineral.

Sample **DVP1-14a** is a highly oxidised reddish-purple, highly plagioclase phyric pillow basalt. Plagioclase laths are randomly oriented, ranging from 10 to 70 μm. The groundmass consists of volcanic glass pseudomorphed to pale brown palagonite, and fine grained opaque minerals. Clinopyroxene grains are weakly pleochroic light brown – mauve augites and are found as small ~10 μm euhedral grains nucleating along plagioclase grain boundaries or as elongate grains ranging from 10 to 70 μm.

Sample **DVP1-12** collected from the thick tabular basalt unit in the middle of the section is medium grey in colour, non-vesicular and moderately to highly plagioclase phyric. The sample is holocrystalline, with sub-ophitic textured light brown - colourless

Figure 2.2 Photomicrograph in plain polarised light of dolerite, showing strongly mauve – pink coloured clinopyroxene grains (cpx) and colourless plagioclase grains (plag). Sample DVP2-3; 3.5 mm field of view.

Figure 2.3 Photomicrograph in plain polarised light of sub-ophitic textured dolerite, with large clinopyroxene grains (cpx) partially enclosing plagioclase laths (plag), with interstitial pseudomorphed volcanic glass groundmass (g). Sample DVP1-13; 3.5 mm field of view.

Figure 2.4 Photomicrograph in plain polarised light of sub-ophitic textured tabular basalt, with large clinopyroxene grains (cpx) partially enclosing plagioclase laths (plag), with interstitial pseudomorphed volcanic glass groundmass (g). Sample DVP1-12; 3.5 mm field of view.

clinopyroxene grains (20-80 μm) enclosing small, randomly oriented laths of plagioclase and fine-grained opaque minerals, surrounded by an interstitial groundmass consisting of volcanic glass pseudomorphed to yellow/green interlayered chlorite/smectite. Large phenocrysts of plagioclase range from ~3 mm to 1 cm, many of which contain melt inclusions.

Samples **DVP2-3** and **DVP1-13** are taken from hypabyssal dolerite sills. DVP2-3 has **s**trongly mauve – pink coloured, weakly pleochroic, elongate clinopyroxene grains ranging from 10 μm to 2 mm. Colourless plagioclase laths ranges from 10 μm to 2 mm, appearing dusty in plain polarised light. Irregular shaped vesicles are partially filled with zones of yellow and green chlorite/smectite and zeolite amygdales. Interstitial volcanic glass appears pseudomorphed to yellow/green interlayered chlorite/smectite and brown palagonite. DVP1-13 has a sub-ophitic texture where plagioclase laths are partially enclosed by large, light brown, euhedral clinopyroxene grains ranging from 20 μm to 2 mm. Large plagioclase grains also range from 20 μm to 2 mm. As with DVP2-3, the interstitial volcanic glass appears pseudomorphed to yellow/green interlayered chlorite/smectite and brown palagonite, but has a greater abundance of opaque minerals.

2.3 Double Point

The ~ 18 m thick section at Double Point has the thickest sedimentary sequence, consisting of massive pillow basalts and tabular basalt flows interbedded with pebbly conglomerate, hyaloclastite breccia, fine- to medium-grained sandstone, siltstone and mudstone. The ~6 m thick sedimentary package consisting of hyaloclastite breccia, conglomerate, fine- to medium-grained sandstone, siltstone and mudstone pinches out to a ~2m hyaloclastite breccia and mudstone sequence at Davis Point, and does not outcrop at Mount Waite.

Both the 1.5 m thick conglomerate unit at the base of the section and the 1m thick conglomerate unit at the top of the section are framework supported, crudely bedded and normally graded, composed of gabbro, dolerite and basalt pebbles and cobbles. Both conglomerate units show gradational transitions to sandy mudstones. Sandstones are grey-green coloured, medium- to coarse-grained, normally graded with fine sandstone and mudstone laminations at the top of units, and rare hyaloclastite

lenses. Sandstones commonly exhibit ripple marks at the top of units. Individual units range in thickness from ~0.5 m to ~20 cm, with a total thickness of approximately 1.5 m. Moderate orange-pink sandy mudstone units commonly overly sandstone units, ranging from 0.5 m to 2 m in thickness.

Compared with Davis Point and Mount Waite there are few volcanic sequences at Double Point, consisting of (i) ~4 m unit of tabular basalt; (ii) pillow basalt; and (iii) a concealed section (likely pillow basalt) overlain by tabular basalt at the top of the unit. Rare matrix supported hyaloclastite is found overlying pillow basalt units ranging from ~5 -10 cm thick units. Clasts are cobble-sized angular fragments with a similar lithology to the underlying pillow basalts.

2.3.1 Igneous Petrography

DLP3-21 and **DLP3-11** are hypocrystalline tabular basalts with elongate, weakly altered plagioclase laths (20 – 40 μm) intergrown with colourless euhedral to subhedral clinopyroxene grains that range from 5 to 100 μm, average 15 – 20 μm. Large euhedral phenocrysts of plagioclase reach up to 10 mm in diameter. Fine grained (<5 μm) opaques are common. Interstitial volcanic glass appears pseudomorphed to green/brown palagonite. DLP3-11 contains irregular shaped vesicles are partially filled with yellow chlorite/smectite alteration, reaching up to 70 μm.

DLP4b-2 is a hypabyssal sill with a coarse grained doleritic texture. Euhedral plagioclase laths are randomly oriented, ranging from 20 – 50 μm, with large phenocrysts up to 80 μm; sharing crystal faces with euhedral to subhedral light brown – pale mauve clinopyroxene grains. Rare (<5 %) volcanic glass has been pseudomorphed to brown palagonite. Opaque minerals are coarser than the tabular basalts, reaching up to 10 μm. Some staining along grain boundaries of minerals adjacent to opaque minerals is present.

2.3.2 Sandstone Petrography

The sandstone (**DLP1b-5a**, **DLP3-20**) clasts are sub-angular to sub-rounded, tightly packed, moderately sorted with no preferred grain orientation; they contain minor clay matrix and rare mudstone rip up clasts, and no visible cement. Basaltic and doleritic lithic fragments constitute up to 20-30 % of clasts. Doleritic textured lithic fragments contain actinolitic clinopyroxene and plagioclase laths, basaltic lithics consist

of fine-grained zeolitised groundmass, with small, randomly oriented plagioclase laths. Sand-sized monomineralic plagioclase feldspar clasts constitute 50-60 %, and are partially altered, appearing dusty under plain polarised light, some exhibiting minor alteration to sericite. Sand-sized monomineralic clinopyroxene clasts remain relatively little altered and compose 20-30% of the sand. The remainder of the sand-sized clasts are composed of monomineralic clasts of chlorite aggregates, epidote, prehnite and minor opaques. Rare quartz clasts are observed in DLP3-20.

2.4 Mount Waite

Extensive pillow basalts and tabular basalts together with coarse-grained sandstones and mudstones make up the extrusives-volcaniclastic succession at Mount Waite. The pillow basalts range from: (i) 7 m thick dark grey, aphyric to sparsely plagioclase phyric, moderately vesicular unit at the bottom of the section; (ii) 10 m thick light grey, highly plagioclase phyric with siliceous selvages between pillows; (iii) highly oxidised reddish-brown, highly plagioclase phyric and with moderate vesicularity at the top of the section. Sandstone units are grey-green coloured, medium- to coarse-grained, normally graded with fine sandstone and mudstone laminations, and commonly exhibit cross bedding. The sandstone units are ~0.5 m thick at the base of the sections, pinching out to ~20 cm at section 6b. Moderate orange-pink sandy mudstone units commonly overly sandstone units, but are also found overlying pillow basalt or hyaloclastite units ranging from ~30 cm to 1m in thickness. Rare hyaloclastite at the bottom of the section is ~2.5 m thick and contains pebble- to cobble-sized angular clasts of basalt and dolerite. This unit is matrix supported.

2.4.1 Igneous Petrography

Sample **MW4-6b** is a highly oxidised reddish-purple, highly plagioclase phyric, highly vesicular pillow basalt. Plagioclase laths are randomly oriented, ranging from 10 to 70 μm. The groundmass consists of volcanic glass pseudomorphed to pale brown palagonite, and fine grained opaque minerals. Clinopyroxene grains are weakly pleochroic light brown – mauve augites and are found as small ~10 μm euhedral grains nucleating along plagioclase grain boundaries or as elongate grains radiating from a central point, ranging from 10 to 70 μm.

Figure 2.5 Photomicrograph in plain polarised light showing mauve clinopyroxene grains (cpx) and colourless plagioclase laths (plag). Clinopyroxene grains commonly nucleate along plagioclase grain boundaries (shown by arrow), with interstitial pseudomorphed volcanic glass groundmass (g). Sample MW4-3; 1.75 mm field of view.

Figure 2.6 Photomicrograph in plain polarised light, showing light brown – mauve clinopyroxene phenocrysts (cpx) nucleating along plagioclase (plag) phenocryst boundaries (shown by arrow) or as elongate grains radiating from a central point, with interstitial pseudomorphed volcanic glass groundmass (g). Sample MW4-6b; 1.75 mm field of view.

Figure 2.7 Photomicrograph in plain polarised light of fine-grained vesicular basalt with rare euhedral plagioclase (plag) phenocrysts. The vesicles (v) are filled with chlorite/smectite interlayered clay and zeolite. Sample MW5-1; 3.5 mm field of view.

Sample **MW4-3** is a holocrystalline pillow basalt. Clinopyroxene grains are pale mauve – pink coloured, weakly pleochroic, elongate grains ranging from 5 – 30 μm, and are commonly found nucleating along grain boundaries of plagioclase. Plagioclase laths are randomly oriented, ranging from 10 – 80 μm, averaging 30 μm. Sub-spherical vesicles are filled with laumontite with a small rind of radially fanning zeolite. Volcanic glass groundmass has been ubiquitously pseudomorphed by palagonite and smectite/chlorite.

MW5-1 and **MW4-4** are medium grey in colour, moderately-vesicular and highly plagioclase phyric. The samples are cryptocrystalline, with rare light brown clinopyroxene grains (<5 μm) surrounded by variably sized plagioclase grains ranging from 5 – 50 μm. Interstitial volcanic glass groundmass is pseudomorphed by palagonite and smectite/chlorite. Large subhedral phenocrysts of plagioclase range from ~3 mm to 9 mm, averaging 5 mm. Irregular shaped vesicles are partially filled with zones of brown palagonite, a layer of yellow chlorite/smectite and green zeolite alteration, and infilled with a white zeolite or carbonate. MW5-1 contains more vesicles.

2.4.2 Sandstone Petrography

The sandstone texture (**MW4-1**, **MW4-2**, **MW6-2, MW6-3**) is sub-rounded, moderately to tightly packed, moderately to well sorted, with bedding seen at the thin section scale defined by different grain sizes. The samples are rich in sub-rounded to rounded zeolitised fine- grained basalt lithic fragments (up to 20-30 %) and lesser dolerite clasts, and contain a colourless, low relief, low birefringent cement, possibly analcime or wairakite. Grain boundaries are commonly coated with a reddish – brown Fe stain. Doleritic textured lithic fragments contain clinopyroxene and plagioclase laths. Basaltic lithics are finer-grained with small plagioclase laths, and are commonly cut by thin veins of laumontite, prehnite and/or epidote. Monomineralic plagioclase feldspar clasts constitute 50-60 %, and are partially altered, appearing dusty under plain polarised light, some exhibiting minor sericite, carbonate and epidote alteration. Clinopyroxene clasts are little altered compared to the plagioclase clasts. They comprise 10-20 % of the sand, with the remaining 20 % composed of monomineralic clasts of hydrothermal minerals such as chlorite aggregates, amphibole, epidote, carbonate, decussate textured prehnite and minor opaques. Colourless monomineralic laumontite clasts are common. Rare fault rock clasts containing very pale yellow epidote

porphyroclasts surrounded by a recrystallised mantle of finer-grained light brown epidote, and have anomalous blue birefringent chlorite and laumontite strung out into veins (MW4-1).

2.5 Other Localities

Additional igneous and sedimentary rock samples were collected from across the island in order to compare with samples within the detailed west coast sections described above.

0221O is a sample collected from the sheeted dolerite dyke complex from Tussock Point, containing microxenoliths of clinopyroxenite. For the purpose of this study only the coarse grains of clinopyroxene within the xenolith have been targeted for geochemical analysis. The clinopyroxene grains are colourless, randomly oriented, and rarely have minor interstitial plagioclase. The clinopyroxene grains are mostly subhedral, with some elongate grains, and show minor exsolution lamellae. The xenoliths show some interaction with the dolerite host rock shown by a pale green reaction rim in hand sample.

0116C is a sample of coarse grained, mylonitic gabbro collected from Langdon Bay, which is directly adjacent to the Finch – Langdon fault (Figure 1.1). The gabbro is ductilly deformed such that the plagioclase has largely been recrystallised. The clinopyroxene porphyroclasts have acted as relatively rigid inclusions, with some minor recrystallised mantles. The clinopyroxene porphyroclasts are beige – pale pink in colour, and show minor alteration along grain boundaries to biotite and brown amphibole. For the purpose of this study only the cores of clinopyroxene porphyroclasts have been targeted for geochemical analysis.

DP1-5c is an undeformed coarse-grained gabbro cobble collected from a cobbly sandstone at Douglas Point. Clinopyroxene grains are pale pink – pale brown in colour, and also show variable amphibolitisation along grain boundaries. Plagioclase laths are euhedral and randomly oriented.

Four samples from Mawson Point (**MP1-3**, **MP1-4**, **MP1-6**, **MP1-7**) of fine- to coarse- grain size have been collected from one continuous fining-upward section of sandstone, in order to compare the mineralogy with grain size. The characteristics of these sandstones are similar to those described from Double Point and Mount Waite.

Figure 2.8 Photomicrograph in plain polarised light showing coarse-grained dolerite with interlocking clinopyroxene (cpx) and plagioclase (plag) grains and rare opaque minerals (opq). Sample DLP4b-2; 3.5 mm field of view.

Figure 2.9 Photomicrograph in cross polarised light showing clinopyroxenite microxenolith (cpx). Sample 0221O; 3.5 mm field of view.

Figure 2.10 Photomicrograph in plain polarised light of mylonitic gabbro showing a clinopyroxene porphyroclast (cpx) surrounded by a fine-grained matrix of recrystallised plagioclase (plag), with minor amphibole (amp) and biotite (bi). Sample 0116C; 3.5 mm field of view.

Figure 2.11 Photomicrograph in plain polarised light of fault rock clast with epidote (ep) porphyroclast surrounded by a recrystallised mantle of finer-grained epidote (ep_m), with chlorite (chl) and laumontite (lmt) strung out into veins. Sample MW4-1; 1.75 mm field of view.

Figure 2.12 Photomicrograph in plain polarised light of dolerite textured lithic fragments containing small clinopyroxene and plagioclase laths, and fine-grained basalt lithics, containing small, randomly oriented plagioclase laths. Rare basalt lithic clasts show veins (shown by arrow). Sample MW4-1; 3.5 mm field of view.

Figure 2.13 Photomicrograph in cross polarised light showing aggregates of prehnite (prh) and epidote (ep). Sample MW4-1; 1.75 mm field of view.

Figure 2.14 Photomicrograph in plain polarised light showing clinopyroxene clasts (cpx) and epidote (ep), altered plagioclase clasts (plag), aggregates of chlorite (chl) and fine-grained lithic fragments (shown by arrow). Note Fe staining on grain boundaries. Sample MW4-1; 1.75 mm field of view.

Figure 2.15 Photomicrograph in plain polarised light showing clinopyroxene clasts (cpx) and epidote (ep), altered plagioclase clasts (plag), aggregates of chlorite (chl) and colourless zeolite cement (shown by arrow). Note Fe staining on grain boundaries. Sample MW6-3; 1.75 mm field of view.

Figure 2.16 Photomicrograph in plain polarised light showing clinopyroxene clasts (cpx) and epidote (ep), altered plagioclase clasts (plag), aggregates of chlorite (chl) and fine-grained lithic fragments (shown by arrow). Note lack of Fe staining on grain boundaries. Sample DLP1b-5a; 1.75 mm field of view.

Samples **0119A** (Unity point), **MI-3B** (Tussock Point) and **DB1-1** (Davis Bay) are coarse grained dolerites from sheeted dyke complexes exposed in the northern quarter and mid-coastal sections of the island. The clinopyroxene grains are euhedral, colourless – pale pink – pale brown coloured, ranging from 50 μm to 1 mm. Grains of clinopyroxene appear altered to either acicular brown amphibole or pale green, weakly pleochroic amphibole. Plagioclase grains are euhedral, randomly oriented laths, appearing variably dusty and altered under plain polarised light.

2.6 Whole-Rock analyses by X-ray Fluorescence Spectrometry

2.6.1 Analytical Method

Selected basalt and dolerite samples from the Davis Point, Double Point and Mount Waite sections were broken into small (<2 cm) pieces using a hydraulic rock splitter, with care taken to remove weathered rinds and avoid phenocryst rich portions. The rock chips were then crushed to a <63 μm powder in a tungsten carbide ring mill.

Whole-rock major and trace-element analyses were conducted at the University of New South Wales Analytical Centre using a Phillips PW2400 X-Ray Fluorescence (XRF) Spectrometer. Samples were prepared following the analytical procedure described in detail by Norrish and Hutton (1969). Major elements were determined by analysis of fused glass discs, and pressed powder pellets were utilised for trace-element determination. Loss on ignition (LOI) was determined gravimetrically. Mg-number (Mg #) is defined here as Mg # = Mg/ (Mg + Fe^{2+}) where Fe^{2+} is the molecular proportion of FeO*. FeO* is estimated to be 90% of Fe_2O_3.

2.6.2 Whole-rock Major and Trace-element Geochemistry

Whole-rock major and trace-element compositions are listed in Table 2.1. When plotted on a total alkali versus silica discrimination diagram (Figure 2.17), the basalt samples (DVP1-11, DLP3-11, MW4-3, MW4-6b) plot within the basalt field, and fall within the sub-alkaline/tholeiitic series. Dolerite samples DVP1-13 and DLP4b-2 also plot within the basalt field within the sub-alkaline/tholeiitic series, DVP2-3 plots within the alkaline series in the trachy-basalt field. The basalts and dolerites examined in this

Table 2.1 Whole-rock major and trace-element compositions for basalts and dolerites. LLD = lower limits of detection; Mg # and FeO* as defined in text.

Samples		Dolerites			Basalts			
(wt %)	LLD (wt %)	DVP2-3	DVP1-13	DLP4b-2	DVP1-11	DLP3-11	MW4-3	MW4-6b
SiO_2	0.04	48.27	47.52	49.71	47.11	45.88	44.41	46.56
TiO_2	0.02	1.93	1.81	1.74	2.02	1.71	1.32	1.83
Al_2O_3	0.02	16.85	15.21	15.24	15.57	15.54	15.37	15.73
FeO*	0.01	7.52	9.29	9.55	9.69	8.10	7.66	8.39
MnO	0.04	0.14	0.16	0.21	0.18	0.16	0.16	0.16
MgO	0.01	7.51	9.81	6.67	7.09	9.91	10.80	6.89
CaO	0.10	8.95	8.43	10.53	10.08	8.63	10.19	10.85
Na_2O	0.01	3.33	2.63	2.74	2.91	2.80	2.26	2.90
K_2O	0.01	1.59	0.31	0.31	0.50	0.84	0.61	0.63
P_2O_5	0.01	0.48	0.32	0.24	0.36	0.39	0.29	0.35
SO_3		<0.01	<0.01	0.13	<0.01	<0.01	<0.01	<0.01
LOI		N.D.	N.D.	N.D.	4.75	5.72	7.16	N.D.
Total		96.56	95.48	96.93	95.50	93.97	93.07	94.29
Mg #		0.64	0.65	0.55	0.57	0.69	0.72	0.59
Measured Fe_2O_3	0.01	8.36	10.32	10.61	10.77	9.00	8.51	9.32
(ppm)	LLD (ppm)							
Rb	1.0	39.3	6.7	6.6	13.7	15.3	13.9	11.2
Ba	8.0	570	155	115	121	428	164	208
Th	2.8	4.2	<2.8	<2.8	<2.8	<2.8	<2.8	<2.8
U	2.9	<2.9	3.4	3	3.7	<2.9	<2.9	5.7
Nb	1.0	61	27	17.5	32.4	44.7	27.8	38.6
Ce	3.0	65.9	35.8	22.3	32.4	44.6	34.7	64.3
As	2.5	3.5	<2.5	<2.5	2.5	2.9	2.8	2.5
Pb	2.0	3	<2.0	2.1	<2.0	3.2	<2.0	2.5
Sr	0.9	437	192	184	193	303	228	277
Zr	1.0	164	140	128	175	153	107	159
Y	1.0	29.5	36.6	38.6	45.2	31.1	24.9	36.4
Cr	2.9	118	218	78.1	205	322	359	165
Ni	2.0	73.1	199	48.6	141	238	258	125
V	2.9	191	284	311	296	199	179	257
Cu	2.0	64.3	28.7	70.6	36.9	18.3	16.4	54.7
Zn	1.8	65.1	76.2	98.3	88.3	67.5	59	79.9
Co	2.9	42.2	53.4	52.6	48	53	53.1	49.1
Ga	1.0	16.5	18.7	18.1	20.4	17	14.6	17.6
Sn	3.9	4.2	<3.9	<3.9	<3.9	<3.9	<3.9	<3.9
Sb	2.9	<2.9	<2.9	<2.9	<2.9	<2.9	<2.9	<2.9
Mo	1.8	<1.8	2	1.8	2.3	<1.8	<1.8	<1.8
Cd	15.4	3	<3.0	<3.0	<3.0	<3.0	<3.0	5.3
Catanorm (%)								
Quartz		0.00	1.67	5.79	1.44	0.00	0.00	0.00
Orthoclase		10.21	2.05	2.05	3.35	5.55	4.04	4.20
Plagioclase		61.09	58.74	59.41	61.41	58.76	56.51	61.35
Nepheline		0.00	0.00	0.00	0.00	0.00	0.00	0.00
Hypersthene		6.74	27.97	13.00	16.15	14.81	9.64	12.75
Diopside		7.63	4.75	15.31	12.17	6.78	13.20	16.08
Olivine		8.98	0.00	0.00	0.00	9.32	12.96	0.59
Ilmenite		0.24	0.29	0.37	0.32	0.28	0.28	0.28
Titanite		4.02	3.80	3.52	4.30	3.58	2.68	3.92
Apatite		1.09	0.74	0.56	0.86	0.91	0.68	0.83

study exhibit a range of normative compositions ranging from olivine normative to slightly quartz normative (Figure 2.18).

Major element abundances are plotted against SiO_2 in Figure 2.19, with additional basalt and dolerite whole-rock data from Griffin (1982) plotted for comparison. MgO, CaO, Al_2O_3, K_2O, FeO* and P_2O_5 show no correlation. Mg # shows a slight negative correlation with SiO_2. Positive covariance is shown by TiO_2 and Na_2O, whereby low values are correspond with low SiO_2. FeO* and P_2O_5 shows considerable scatter.

Major element abundances are plotted against Mg # in Figure 2.20, again with additional data from Griffin (1982) plotted for comparison. SiO_2, TiO_2, Na_2O and FeO* show a strong negative correlation with Mg #. MgO and Al_2O_3, and to a lesser extent, K_2O, show a positive relationship with Mg #. CaO and P_2O_5 show no correlation. FeO* and P_2O_5 shows considerable scatter.

Trace-element abundances are plotted against Mg # in Figure 2.21. Large ion lithophile elements (LILE) such as Rb, Ba, Sr show considerable scatter. High field strength (HFS) elements Y and Zr show a strong negative correlation, however Nb shows a weak positive correlation. A positive correlation is also shown by V. Ni and Cr show strong negative correlations with Mg #.

The basalts have SiO_2 contents that range from 44.41 to 47.11 wt %. The basaltic samples show a large range in major element abundances, in particular CaO (6.83-10.85 wt %) and TiO_2 (1.32- 2.02 wt %). A minimum Na_2O concentration of value 2.26 wt % was obtained for MW4-3, with the other three samples in the range 2.80 to 2.90 wt %. The basalts show significant variability in terms of their Mg #, ranging from 0.57 to 0.72. The basalts analysed in this study have loss on ignition (LOI) values that range from 4.75 to 7.16 wt %.

The dolerites have slightly higher SiO_2 compositions ranging from 47.52 to 49.71 wt %. Samples DVP1-13 and DLP4b-2 have Na_2O compositions similar to the basalts (2.63-2.74 wt %) but lower K_2O compositions of 0.31 wt %. DVP2-3 has Na_2O and K_2O compositions of 3.33 and 1.59 wt % respectively. The dolerites show little variation in terms of their Mg # (0.55-0.65). The CaO content ranges from 8.43-10.53 wt % which is essentially the same as the basalts, however the dolerites show a less pronounced variation in TiO_2 (1.74-1.93 wt %).

The basalts show little variability in Y (~25-45 ppm) and Nb (~28-45), and show Zr compositions ranging from ~107 to 175 ppm. Ba and Sr show greater variability,

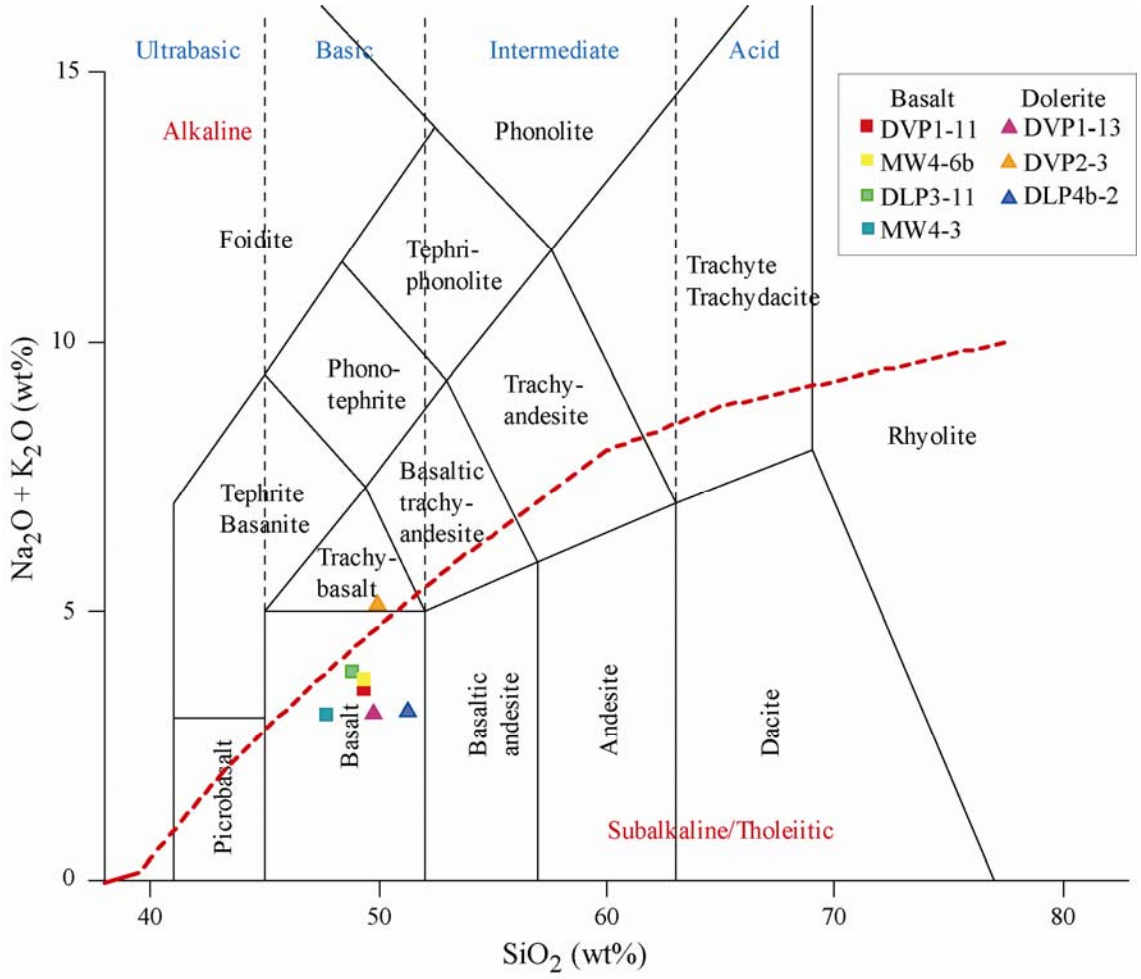

Figure 2.17 Whole-rock total alkali versus silica discrimination diagram. Data from Table 2.1. Fields are from Le Bas et al. (1986).

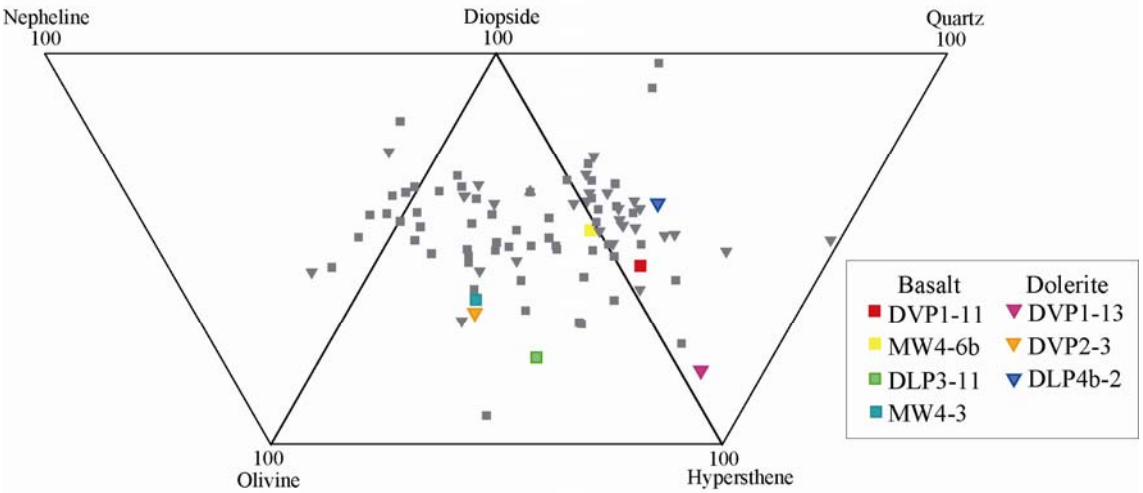

Figure 2.18 Plot of relative proportions of whole-rock normative minerals in basalts and dolerites from Davis Point, Double Point and Mount Waite. Data from Table 2.1. Basalt and dolerite whole-rock dataset from Griffin (1982) shown in grey symbols for comparison. Sample rock types shown by: squares – basalt; triangles – dolerite.

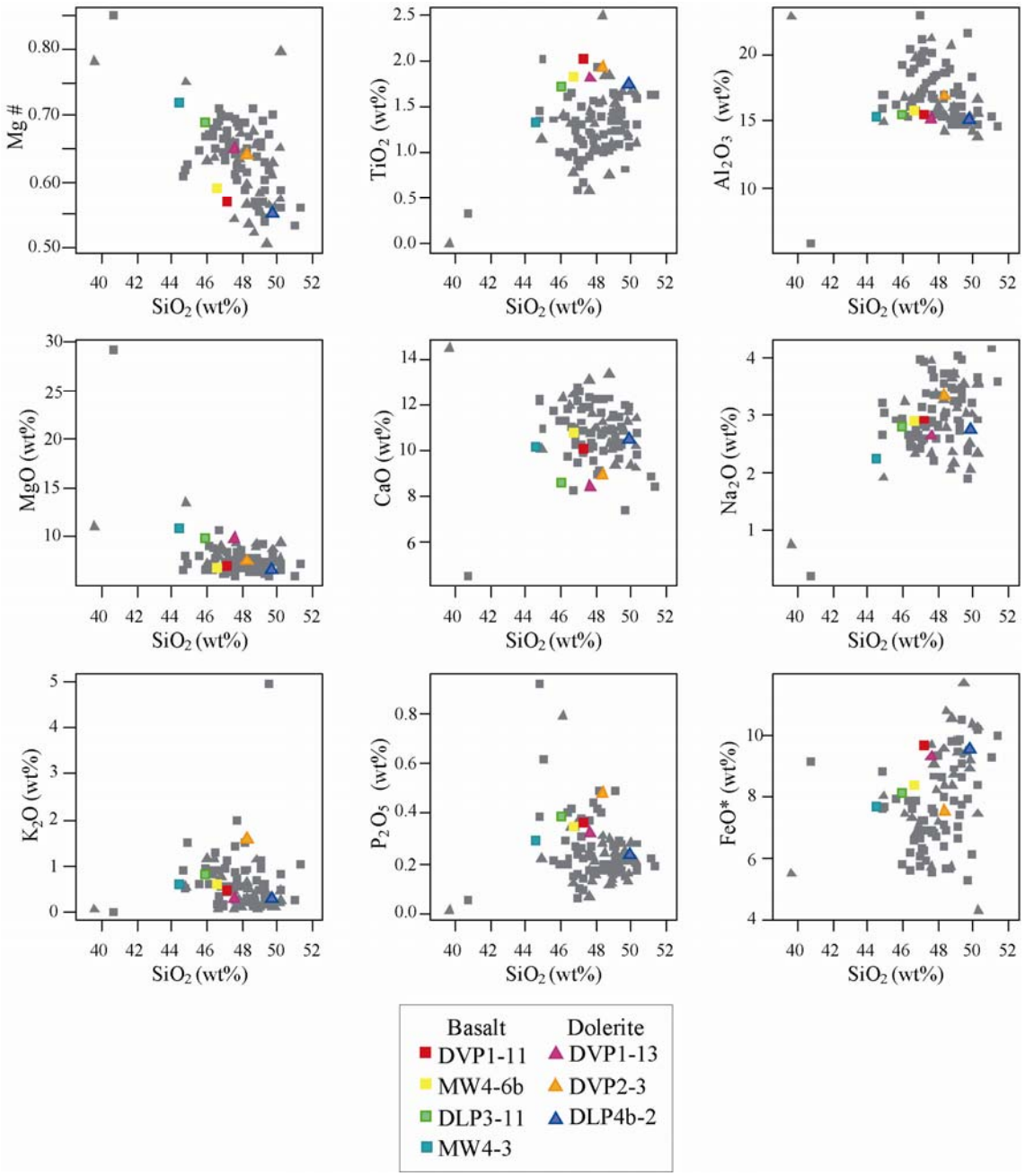

Figure 2.19 Major element abundances against SiO_2. Data from Table 2.1. Basalt and dolerite whole-rock dataset from Griffin (1982) shown in grey symbols for comparison. All axes in wt % except Mg #, calculated as defined in text. Sample rock types shown by: squares – basalt; triangles – dolerite.

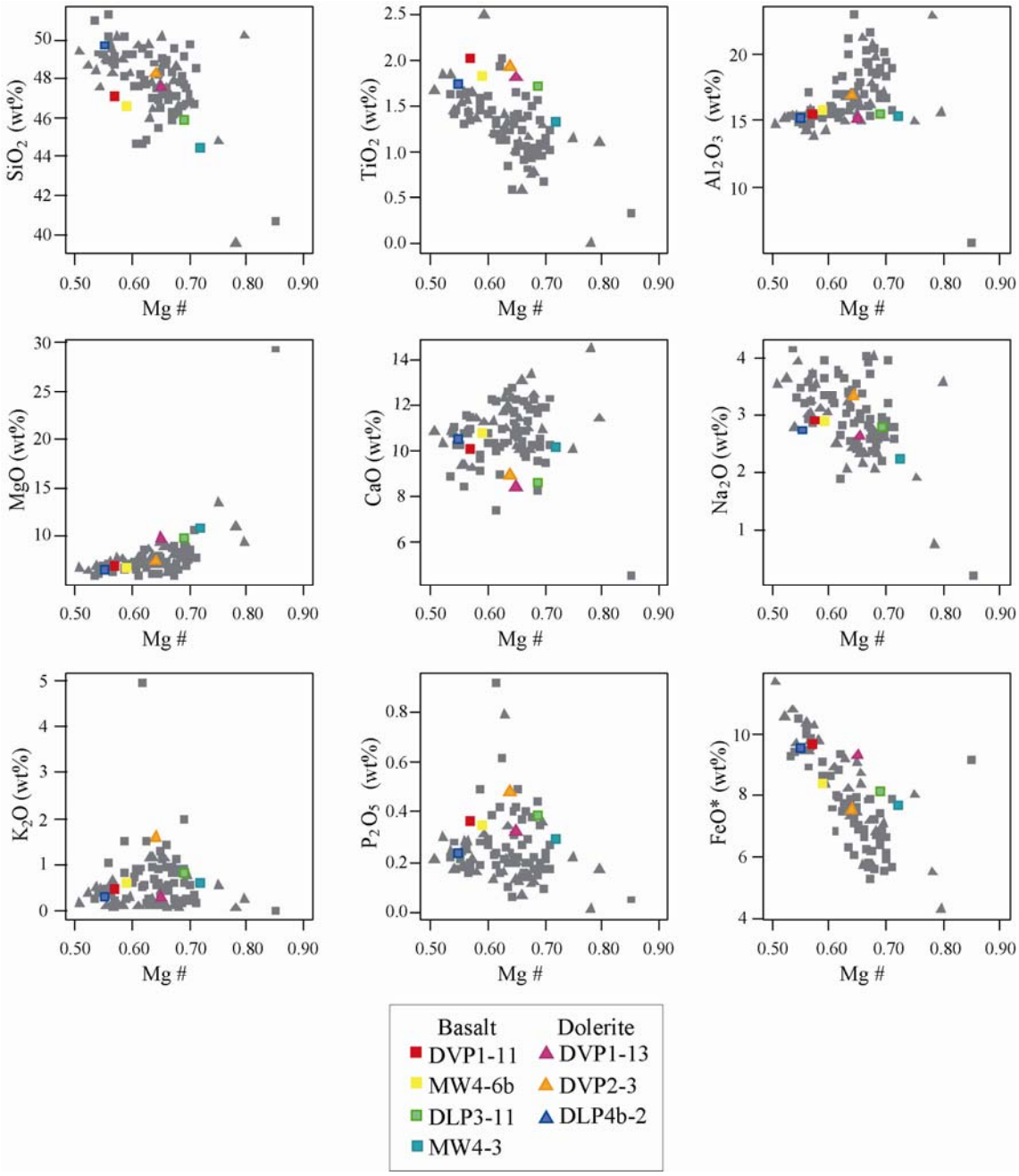

Figure 2.20 Major element abundances against Mg #. Data from Table 2.1. Basalt and dolerite whole-rock dataset from Griffin (1982) shown in grey symbols for comparison. All axes in wt % except Mg #, calculated as defined in text. Sample rock types shown by: squares – basalt; triangles – dolerite.

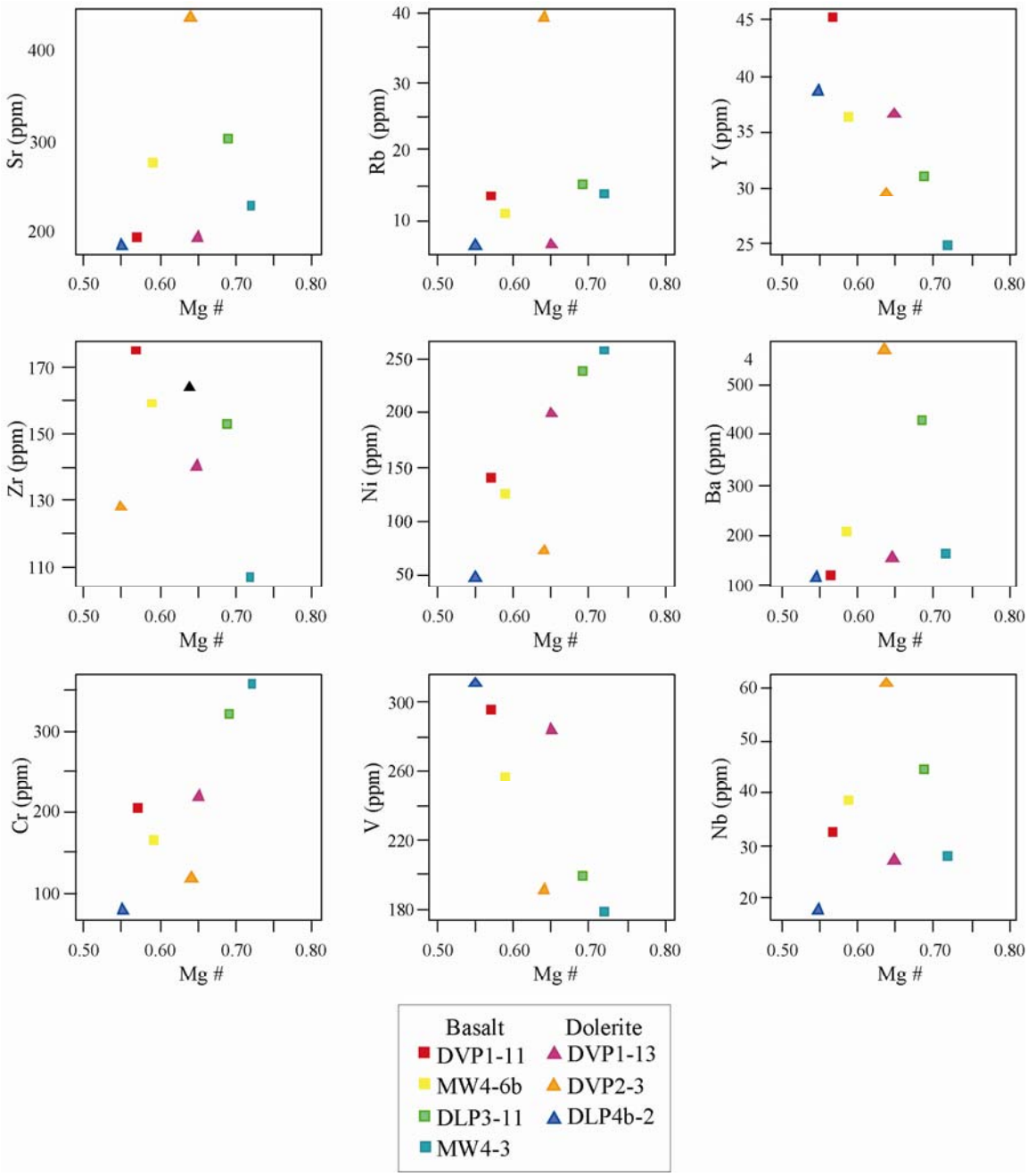

Figure 2.21 Trace-element abundances against Mg #. Data from Table 2.1. All axes in ppm except Mg #, calculated as defined in text.

with ~193 to 303 ppm and ~120 to 428 ppm respectively. These overall trace-element trends are similar in the dolerites, with Y compositions ranging from ~30 to 39 ppm, slightly higher Nb compositions ranging from ~18 to 61 ppm, Zr ranging from ~128 to 164 ppm, and greater variability in Ba (~115-570 ppm) and Sr (~184-437 ppm).

Rb content is typically low in both the basalts and the dolerites (~7-15 ppm), except for DVP2-3 which has ~40ppm. V shows similar enrichment in both the basalts and the dolerites (~180-300 ppm). Cr shows greater enrichment in the basalts, ranging from ~170 to 360 ppm, with ~80-210 ppm in the dolerites. The basalts have Ni contents ranging from ~140-250 ppm. the dolerites have typically lower concentrations of 50 to 70 ppm, except DVP1-13 which contains 200 pmm Ni.

2.7 Discussion

2.7.1 Petrographic Observations

In thin section, the optical properties of igneous clinopyroxene grains is variable, ranging from (i) elongate, weakly pleochroic dark mauve – pink; (ii) euhedral, weakly pleochroic light brown – mauve; to (iii) euhedral, colourless grains. Given the extent of variability, qualitative comparison between clinopyroxene grains within potential source rocks and clinopyroxene clasts in the sandstones is not a viable method to determine the provenance of the sands.

Relative immaturity of the sandstones are indicated by sub-angular to sub-rounded grain morphology, little to no matrix or cement, high percentage of basaltic and doleritic lithic fragments, and the partially altered plagioclase feldspars. Daczko et al. (2005) note a lack of exotic clasts such as and propose a local source with no continental input.

The high abundance of hydrothermal monomineralic clasts including epidote, prehnite, quartz, sulphides, carbonates and zeolites, and clasts of fault rock within the sedimentary rocks is used by Daczko et al. (2005) to interpret a fault-scarp provenance for the volcaniclastic deposits on Macquarie Island. The close proximity of the sandstones to the major seafloor spreading related faults led Daczko et al. (2005) to interpret these adjacent faults as the source where the sediment was produced by the physical disintegration and tectonic abrasion of oceanic crust in the adjacent fault zones.

The petrography of the sedimentary samples in this study confirms the high abundance of monomineralic and fault rock clasts identified by Daczko et al. (2005).

However, a significant proportion of chlorite in addition to the hydrothermal minerals identified by Daczko et al. (2005) is noted. The identification of laumontite as the key zeolite group mineral here suggests hydrothermal temperatures up to 200 - 250 ˚C (Griffin, 1982). In addition, it is noted that the monomineralic plagioclase feldspar clasts show variable alteration to sericite, carbonate and epidote, typical of hydrothermal alteration. These observations support the interpretation of a fault-scarp provenance. However, common pebble- to cobble-sized gabbro clasts within the conglomerate units at Davis and Double points imply that lower crustal units below the sheeted dolerite dykes comprise part of the source. As gabbro is only exposed in the north of Macquarie Island, either these clasts are derived from there or from sub-marine crust offshore. However, south to north palaeo-current indicators including ripple bedding indicate that an offshore provenance is likely (Ryan Portner, pers. comm.)

The observation of pebble- to cobble-sized conglomerates at Davis and Double points that either lens out or grade into sandstone at Mount Waite suggests a west to east fining of sediment. Repeated fining-upwards cycles from the conglomerates through massive sandstone, ripple bedded sandstone to finely laminated silt and mud are characteristic of a Bouma sequence (Bouma, 1962). These observations best match a turbidity flow transport mechanism for the sediment.

Rare laumontite and carbonate cement lithify some sedimentary rocks; however a general lack of visible cement and the presence of Fe oxide coatings on grains suggest that Fe oxide may be the principle cement. The sandstones are moderately to tightly packed, suggesting significant compaction of unconsolidated sediment due to the overlying volcanic and sedimentary units. Though the glassy component of the basalts shows variable seafloor weathering to greenschist facies metamorphism, this is less evident in the interbedded sedimentary rocks. This may be a result of the relative susceptibility to metamorphism of the volcanic glass versus sedimentary clasts.

2.7.2 Lithostratigraphic and Petrographic Basalt Correlations

Based on lithostratigraphy the basalts may be tentatively correlated across the three sample sites in the detailed section (Figure 2.1). Two petrographic correlations can be inferred on the basis of mineralogy and textures for basalts in which samples were collected. The first correlation is between samples DVP1-14a and MW4-6b. Both samples are highly oxidised reddish-purple, highly plagioclase phyric, highly vesicular

pillow basalts. In both samples, small weakly pleochroic light brown – mauve clinopyroxene grains are found along plagioclase grain boundaries, or as elongate radiating grains.

A second correlation between MW4-4 and MW5-1 may be made on the basis of mineralogy and texture. The samples are medium grey in colour, moderately-vesicular and highly plagioclase phyric, with phenocrysts ranging from 3 mm to 9 mm. Rare light brown clinopyroxene grains in both samples are small, (<5 μm) surrounded by variably sized plagioclase grains. Interstitial volcanic glass groundmass is pseudomorphed by palagonite and smectite/chlorite. MW5-1 contains a higher percentage of vesicles; MW4-4 has a greater abundance of fine-grained opaque minerals.

These preliminary correlations will be examined further by characterising the major element geochemistry of the clinopyroxene grains in Chapter 3.

2.7.3 Whole-rock Geochemistry

Previous geochemical studies (Varne et al., 1969; Griffin and Varne, 1980; Kamenetsky et al., 2000; Varne et al., 2000) have shown that most of the dolerites and basalts on Macquarie Island exhibit Pacific Mid Ocean Ridge Basalt (MORB) signatures, with Mg # ranging from ~0.51 to 0.72, which is consistent with the values of 0.55 to 0.72 obtained in this study. When compared to the larger Macquarie Island basalt and dolerite whole-rock dataset of Griffin (1982), the samples of this study show similar overall trends (Figures 2.19, 2.20), and are broadly representative of the range of basalt and dolerite compositions exposed on the island.

Griffin and Varne (1980) and Varne et al. (2000) reported normative compositions for the basalts and dolerites ranging from olivine bearing tholeiitic varieties (similar to N-MORB), through nepheline bearing variants (similar to E-MORB), to compositions that are more primitive, alkalic and silica under-saturated, with higher nepheline normative compositions than MORB reported elsewhere (Varne et al., 2000). The basalts and dolerites examined in this study exhibit a range of normative compositions ranging from olivine normative to slightly quartz normative and are typical of tholeiitic MORB. Compared with the whole-rock dataset of Griffin (1982), the samples do not represent the alkalic nepheline normative compositions. This might indicate that there are no nepheline normative compositions in the sampled Davis Point, Double Point and Mount Waite sections, or that if present they have not been

sampled. The dolerites (including those from the whole-rock dataset of Griffin (1982)) tend to be less nepheline and diopside rich than the basalts, and generally constitute the quartz normative compositions.

From the petrography, it is evident that both the basalts and dolerites have suffered extensive seafloor alteration and low grade metamorphism (up to lower greenschist facies), indicated by the ubiquitous alteration of volcanic glass by palagonite and/or chlorite/smectite, and the presence of carbonate and zeolite minerals (Chapter 2.2, 2.3, 2.4). This is also reflected in the high values for loss on ignition (LOI).

Multi-element plots normalised to N-MORB and E-MORB are shown in Figure 2.22 using values recommended by Sun and McDonough (1989). When normalised to N-MORB, both the dolerites and basalts show similar overall negative trend, with incompatible elements up to 100 times more enriched than N-MORB, and compatible elements such as Ti and Y ~ 1. When the samples are normalised to E-MORB, the samples exhibit relatively flat overall patterns, with similar elemental abundances to E-MORB, however shows minor enrichment in incompatible elements, with abundances up to one order of magnitude higher than E-MORB element abundances.

In both diagrams, compatible elements such as Ti and Y show abundance of ~1. These compatible elements, along with Zr and Nb are generally regarded to be immobile during seafloor alteration and low grade metamorphism (Pearce and Norry, 1979). This suggests that the composition of these rocks is quite similar to MORB. Conversely, elements such as Rb, Ba, K and Sr are known to be highly mobile elements; hence the enrichment and high degree of variability of these elements are likely a result of extensive seafloor alteration and greenschist metamorphism.

The general scatter and lack of trends of the LILE's (Ba, K, Rb, Sr) when plotted against Mg # (Figures 2.20, 2.21) also appears to reflect the extensive seafloor alteration and greenschist metamorphism. Strong correlations between HFS elements (Ti, Zr, Y, and to a lesser extent Nb) with Mg # is in agreement with their immobile character.

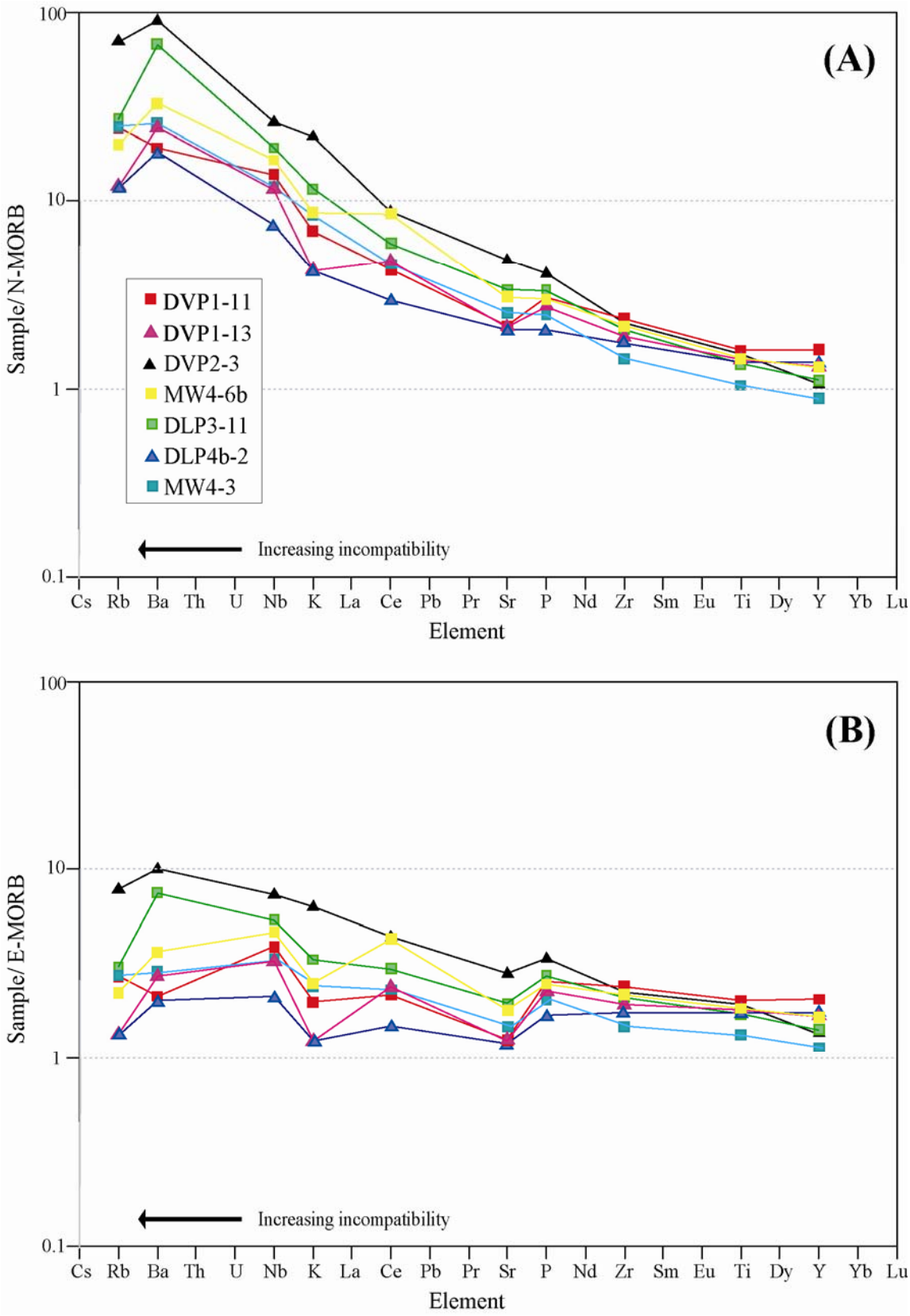

Figure 2.22 Whole-rock multi-element (A) N-MORB and (B) E-MORB normalised spider diagrams. Data from Table 2.1. N-MORB and E-MORB values are from Sun and McDonough (1989).

Chapter 3 Clinopyroxene Geochemistry

3.1 Introduction

Detrital clinopyroxene is well established in its use as a provenance indicator mineral due to its relatively high degree of resistance to chemical and mechanical weathering, and its stability through diagenesis and low grade metamorphism (Cawood, 1983; Beccaluva et al., 1989; Krawinkel et al., 1999). Clinopyroxene is a common mineral in many rock types exposed on Macquarie Island (peridotite, gabbro, dolerite, basalt), and is a common constituent within the sedimentary rocks.

This study investigates detrital clinopyroxene as a provenance indicator mineral by examining the major and trace-element geochemistry of potential clinopyroxene-bearing source rocks and clinopyroxene rich sedimentary rocks in the detailed west coast section. Additional igneous rock samples from the sheeted dolerite dyke complex and gabbros from the north of Macquarie Island have also been analysed in order to sample a larger potential source rocks. Similarly, peridotite clinopyroxene data from Wertz (2003) is also used for comparison with detrital clinopyroxene within the sandstones.

The focus of this study has not been to explore the magmatic processes or tectonic environments, but rather has been to characterise the geochemistry of clinopyroxene within sedimentary rocks and potential source rocks to determine if the sands are derived from a single, or perhaps multiple sources.

The major and trace-element analyses of clinopyroxene were conducted at the Geochemical Analysis Unit housed in the Australian Research Council (ARC) National Key Centre for Geochemical Evolution and Metallogeny of Continents (GEMOC) based in the Department of Earth and Planetary Sciences at Macquarie University, Sydney.

3.2 Analytical Methods

3.2.1 Clinopyroxene Major Element Analyses by Electron Microprobe

Clinopyroxene grains were analysed for major element oxides (SiO_2, TiO_2, Al_2O_3, FeO, MnO, MgO, CaO, Na_2O, and K_2O) and minor oxides (NiO, Cr_2O_3) were

determined on carbon-coated polished thin-sections (~30 μm) using a Cameca SX-100 electron microprobe, equipped with five wavelength dispersive spectrometers (WDS) and a PGT energy dispersion system (EDS). Major and minor elements were analysed on Kα emission lines at an accelerating voltage of 15 keV, a beam current of 20 nA and a focused beam size of 1-2 μm. Counting times of 10 seconds were used for both peak and background determination. Natural mineral and synthetic silicate and oxide standards were analysed for the elements cited in brackets – albite (Na), kyanite (Al), orthoclase (K), Fe_2O_3 (Fe), Mn-garn (Mn), Olivine (Mg), Cr (Cr), TiO_2 (Ti), Casio3 (Si, Ca). The PAP matrix correction procedure (Pouchou and Pichoir, 1984) was applied to convert the raw X-ray intensity data to weight percent oxide. Lower limits of detection and precision data are presented in Table 3.1.

Table 3.1 Lower limits of detection and precision data (expressed as relative standard deviations, RSD) for major elements obtained by Electron Microprobe. Background measured on clinopyroxene.

Element	LLD (wt %)	% rsd
SiO_2	0.03	0.27
TiO_2	0.02	0.19
Al_2O_3	0.01	0.18
Cr_2O_3	0.04	0.56
FeO	0.03	0.34
MnO	0.03	0.55
MgO	0.03	0.22
CaO	0.02	0.27
Na_2O	0.02	0.56
K_2O	0.01	0.49
NiO	0.03	0.30

Analyses of clinopyroxene grains with totals of 100 ± 1.5 weight percent oxide (wt %) were used in this study, but the majority were within 100 ± 1 wt%. All Fe was analysed as FeO (wt %); Fe^{2+}/Fe^{3+} compositions were calculated on the basis of a clinopyroxene mineral stoichiometry of four cations for six oxygens. Clinopyroxene end-member components for wollastonite (Wo), enstatite (En) and ferrosillite (Fs) were calculated following the method detailed by Lindsley (1983) to remove non-quadrilateral components. They are defined here as Wo = Wo/ (Wo + En + Fs); En = En/ (Wo + En + Fs) and Fs = Fs/ (Wo + En + Fs). The Niggli's Molecular Norm (Catanorm) for the whole-rock and clinopyroxene analyses were calculated using the algorithm given by Hutchinson (1975).

3.2.2 Trace-element Determinations by Laser Ablation - Inductively Coupled Plasma - Mass Spectrometry

Polished thick (100 μm) sections for samples of interest were prepared for trace-element analysis by LA-ICP-MS. Trace-element concentrations of clinopyroxene grains were determined *in-situ* using a New Wave UP 266 nm Nd: YAG laser ablation system, linked to an Agilent 7500cs ICP-MS, with no reaction cell. Most analyses were carried out with a beam diameter of 60 μm, with smaller grains 30-40 μm, a 5 Hz (pulses per second) repetition rate, and output energy of ~0.117 mJ per pulse. Ablation was conducted in a He atmosphere (~1 l min^{-1}). The sample + He mixture was combined with Ar (~0.9 l min^{-1}) in a teflon mixing chamber prior to being transported to the ICP. Data acquisition was performed by peak hopping (one point per isotope) in pulse counting mode. Each analysis took 180 s, with a "gas blank" measurement of the carrier gas (He) taken over the first ~50 s, before initiation of ablation of the sample for ~130 s. Data were acquired on 50 isotopes for trace-element determinations, with short dwell times to provide quasi-simultaneous measurements. LA-ICP-MS operating conditions and data acquisition parameters are given in Table 3.2.

Table 3.2 Operating conditions and data acquisition parameters for trace-element determinations by LA-ICP-MS.

ICP-MS		**LA**	
Model	Agilent 7500cs	Model	New Wave, 266 nm
Forward power	1350 KW	Repetition rate	5 Hz
Gas flows:		Pulse duration (FWHM)	6 ns
Plasma (Ar)	13 L min^{-1}	Focussing objective	10x, UV laser achromat, f.l. = 20 mm
Auxiliary (Ar)	0.8 L min^{-1}	Degree of defocussing	200 μm (above sample)
Carrier (He)	~1 l min^{-1}	Spot size	30-40 μm (small); 60 μm (large)
Make-up (Ar)	~0.9 l min^{-1}	Measured pulse energy	~0.117 mJ
Data acquisition parameters			
Data acquisition protocol	Time-resolved analysis		
Scanning mode	Peak hopping, 1 point per peak		
Detector mode	Pulse counting, dead time correction applied		
Isotopes Determined	^{7}Li, ^{9}Be, ^{11}B, ^{23}Na, ^{25}Mg, ^{27}Al, ^{29}Si, ^{31}P, ^{39}K, ^{42}Ca, ^{43}Ca, ^{45}Sc, ^{49}Ti, ^{51}V, ^{53}Cr, ^{55}Mn, ^{57}Fe, ^{59}Co, ^{60}Ni, ^{62}Ni, ^{63}Cu, ^{66}Zn, ^{69}Ga, ^{71}Ga, ^{72}Ge, ^{75}As, ^{85}Rb, ^{86}Sr, ^{88}Sr, ^{89}Y, ^{90}Zr, ^{93}Nb, ^{95}Mo, ^{133}Cs, ^{137}Ba, ^{139}La, ^{140}Ce, ^{141}Pr, ^{146}Nd, ^{147}Sm, ^{153}Eu, ^{157}Gd, ^{159}Tb, ^{161}Dy, ^{165}Ho, ^{167}Er, ^{169}Tm, ^{173}Yb, ^{175}Lu, ^{178}Hf, ^{181}Ta, ^{208}Pb, ^{232}Th, ^{238}U,		
Dwell Times	30 ms for all elements		
Data acquisition time	180 s (50 s gas blank, 130 s ablation of sample)		

Samples were analysed in 'runs' of 15 analyses consisting of two analyses of synthetic NIST-610 glass calibration standards, one analysis of BCR-2G, a basaltic glass reference material, 10 analyses of unknowns, followed by a further two NIST-610 standards. ^{43}Ca was used as an internal standard, using the electron microprobe measurements of CaO (wt %) in the same clinopyroxene grains. The certified values for the NIST-610 standard glass are given in Norman et al. (1996).

Data reduction was completed using the online software package GLITTER (GEMOC Laser ICPMS Total Trace Element Reduction), Version 4.4 (van Achterbergh et al., 1999). The time-resolved analysis software, in which the signal intensity data for each mass and each ratio is displayed as a function of time during the analysis, allows for the most stable portion of the signal to be selected for integration, thereby enabling compositional heterogeneities such as inclusions to be identified and avoided.

Accuracy and precision were monitored by analysis of a basalt glass standard BCR-2G using values given in Norman et al. (1998), and are presented in Table 3.3.

3.3 Results

3.3.1 Clinopyroxene Major Element Geochemistry

Complete tables of all clinopyroxene major element analyses, molar, end-member calculations and normative data are presented in Appendix A. Major element analyses from other minerals are included in Appendix B. Peridotite clinopyroxene major element data from a previous study by (Wertz, 2003) are included for comparison.

The analysed igneous and detrital clinopyroxenes plot in the augite to diopside field using a Wollastonite - Enstatite – Ferrosilite diagram (Figure 3.1). The clinopyroxenes analysed in this study exhibit a range of normative compositions ranging from slightly nepheline normative, through diopside normative to hypersthene normative (Figure 3.2).

Variation diagrams of major element cation proportion are presented in Figures 3.3 to 3.6. Mg-number is calculated using cation proportions, whereby Mg # = Mg/(Mg + Fe^{2+}), where Fe^{2+}/Fe^{3+} compositions were calculated on the basis of a clinopyroxene mineral stoichiometry of four cations for six oxygens.

Table 3.3 Trace-element accuracy and precision data for BCR-2G obtained by LA-ICP-MS in this study and comparison with previously reported data (Norman et al., 1998).

BCR-2G	Norman et al. (1998)		This study n = 9	
(ppm)	Mean	1σ	Mean	SD
Sc	33	0.8	40.1	8.8
V	414	8	428	6
Co	35.8	1.3	37.6	1.2
Ni	10.8	0.7	12.0	0.8
Cu	19.4	1	17.9	1.0
Zn	147	12	149	12
Ga	22.7	0.9	23.3	1.2
Rb	49	2	52.2	1.8
Sr	342	6	338	8
Y	35.3	0.7	31.8	1.4
Zr	194	4	179	10
Nb	12.8	0.4	12.6	1.1
Mo	244	7	260	11
Cs	1.13	0.08	1.25	0.07
Ba	660	19	670	17
La	24.5	0.7	24.8	0.9
Ce	50.5	1.6	51.6	1.1
Pr	6.8	0.3	6.68	0.3
Nd	29	1.1	28.8	0.82
Sm	6.6	0.4	6.47	0.3
Eu	1.92	0.12	1.98	0.09
Gd	6.5	0.4	6.16	0.3
Dy	6.5	0.4	5.97	0.2
Ho	1.31	0.08	1.21	0.07
Er	3.6	0.2	3.41	0.2
Yb	3.5	0.2	3.19	0.2
Lu	0.51	0.03	0.46	0.03
Hf	5.0	0.3	4.64	0.2
Ta	0.78	0.05	0.73	0.11
Pb	11.5	0.6	11.1	1.0
Th	6.1	0.3	5.88	0.3
U	1.73	0.09	1.81	0.07

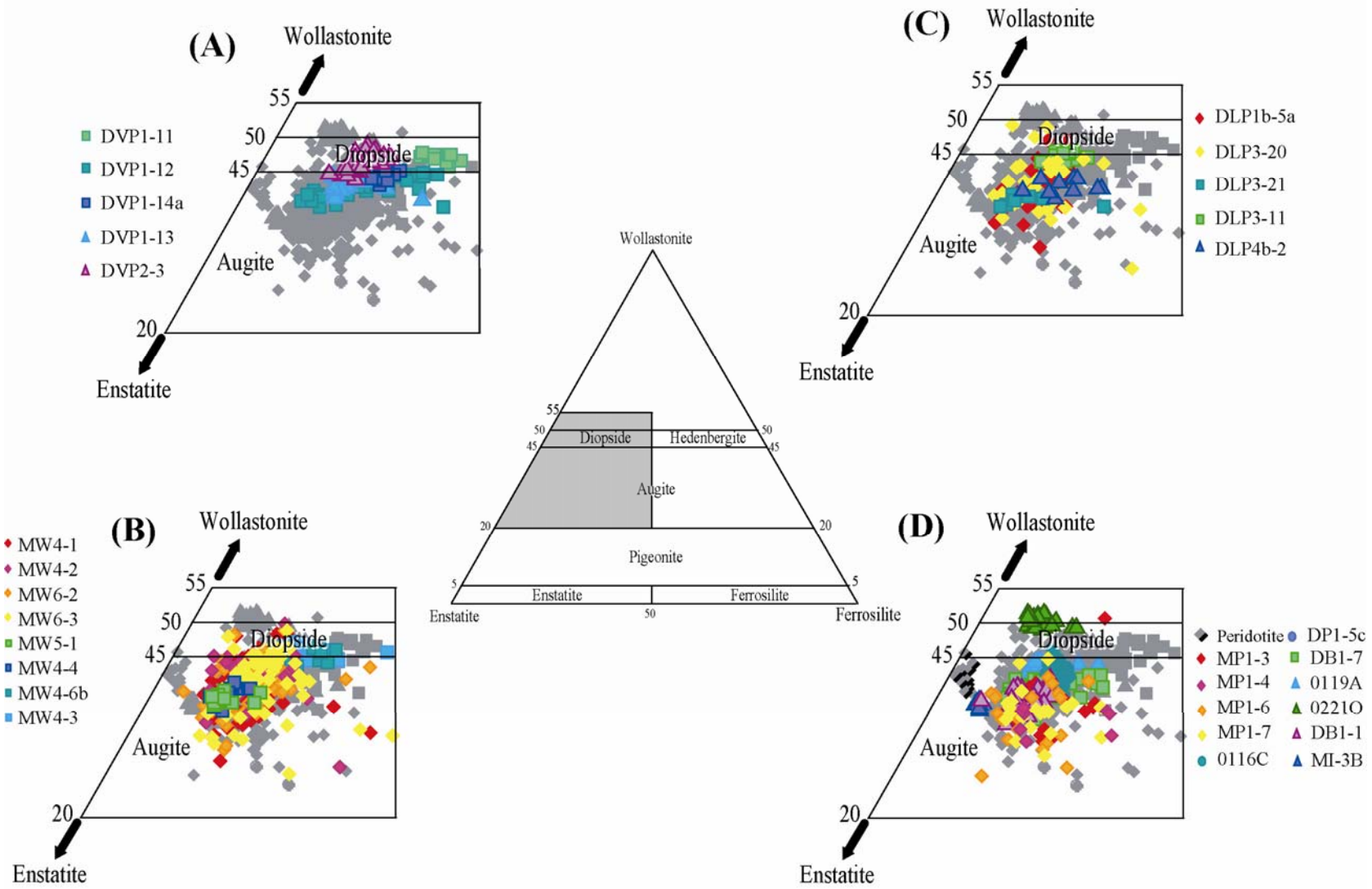

Figure 3.1 Wollastonite – Enstatite – Ferrosilite clinopyroxene discrimination diagram. Fields after Morimoto et al. (1988). Data from Appendix A. Peridotite data from Wertz (2003). Complete dataset shown in grey symbols for comparison. (A) Davis Point; (B) Mount Waite; (C) Double Point; (D) other localities. Sample rock types shown by: squares - basalt; triangle - dolerite; diamond - sandstone; circle – gabbro.

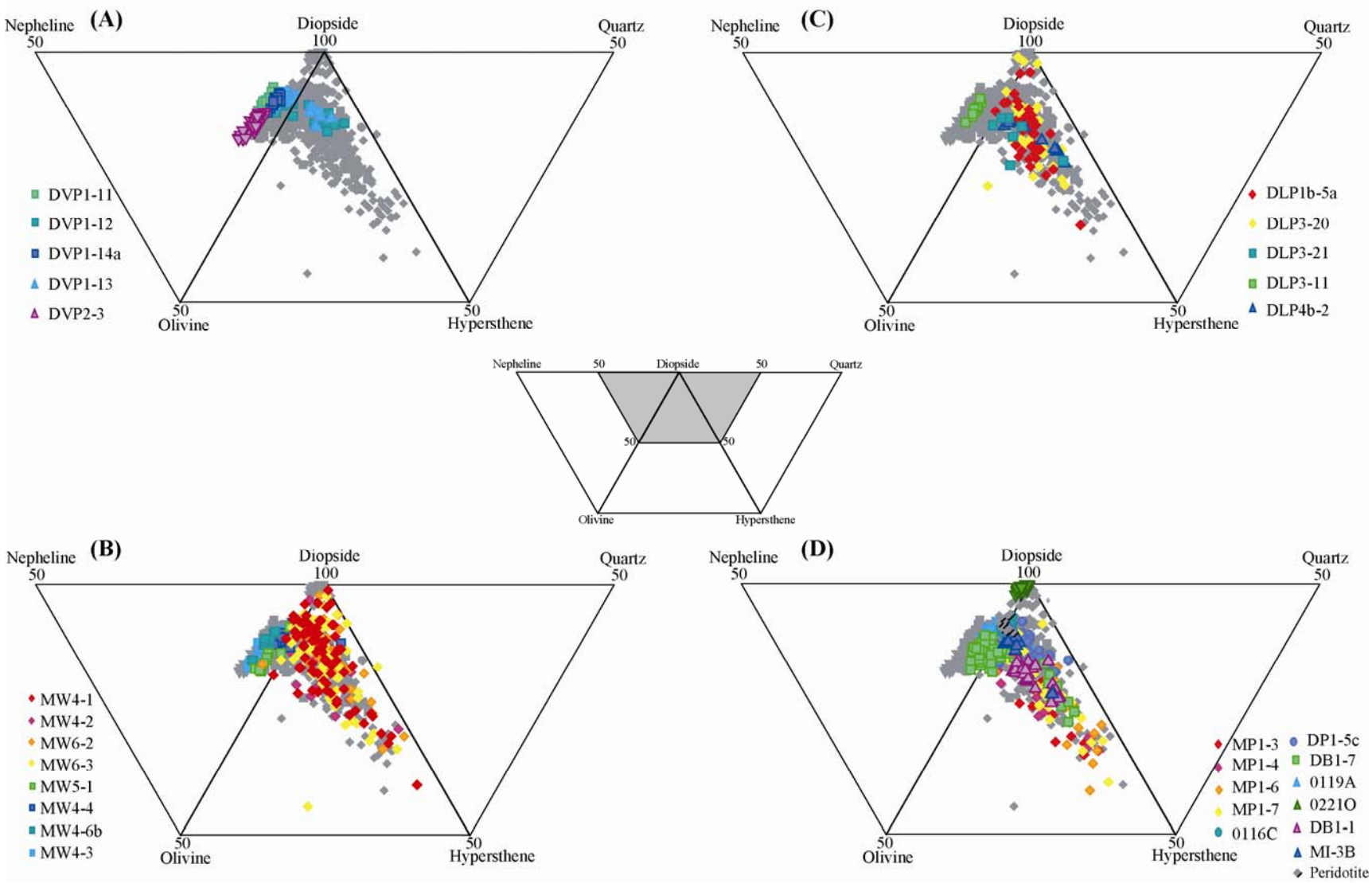

Figure 3.2 Plot of relative proportions of normative minerals for clinopyroxene. Data from Appendix A. Peridotite data from Wertz (2003). Complete dataset shown in grey symbols for comparison. (A) Davis Point; (B) Mount Waite; (C) Double Point; (D) other localities. Sample rock types shown by: squares - basalt; triangle – dolerite; diamond - sandstone; circle – gabbro.

Clinopyroxene grains from basalts from Davis Point (DVP1-11, DVP1-12, DVP1-14a) are characterised by Mg # ranging from 0.55 to 0.87, low to intermediate Ti (0.002-0.18), intermediate Na (0.02-0.05), very low Cr (<0.002) and intermediate Al that ranges from 0.07 to ~0.30, with basalts from DVP1-11 constituting the highest concentrations. The grains are typically olivine normative, and contain $Wo_{0.39-0.46}En_{0.30-0.53}Fs_{0.08-0.25}$.

Clinopyroxene grains from hypabyssal dolerite sills from Davis Point (DVP1-13 and DVP2-3) are characterised by Mg # ranging from 0.63 to 0.83, low to intermediate Ti (0.02-0.16), intermediate Na (0.03-0.05), low Cr (<0.02) and intermediate to high Al that ranges from 0.07 to ~0.47. The grains are typically olivine to slightly nepheline normative, and contain $Wo_{0.40-0.46}En_{0.38-0.48}Fs_{0.09-0.22}$.

Clinopyroxene grains from basalts from Double Point (DLP3-11 and DLP3-21) are characterised by Mg # ranging from 0.66 to 0.86, low to intermediate Ti (0.01-0.11), intermediate Na (0.02-0.04), very low Cr (<0.01) and intermediate Al that ranges from 0.09 to ~0.35. The grains from DLP3-11 are hypersthene normative; grains from DLP3-21 are slightly nepheline normative, and contain $Wo_{0.37-0.45}En_{0.42-0.52}Fs_{0.09-0.21}$.

Clinopyroxene grains from hypabyssal dolerite sills from Double Point (DLP-4b-1a) are characterised by Mg # ranging from 0.68 to 0.83, very low Ti (0.02-0.04), intermediate Na (0.02-0.03), low Cr (<0.01) and intermediate Al that ranges from 0.07 to ~0.15. The grains are typically hypersthene normative, and contain $Wo_{0.39-0.41}En_{0.41-0.50}Fs_{0.1-0.20}$.

Clinopyroxene clasts from the Double Point sandstones (DLP1b-5a, DLP3-20) have Mg # that range from 0.59 to 0.91, very low-intermediate Ti (<0.01 to 0.04), low Na (0.02 to 0.03), low Cr from below detection to 0.04, and low to intermediate values of Al that range from 0.02 to 0.11. The clinopyroxene clasts within the sandstones are hypersthene normative and contain $Wo_{0.35-0.48}En_{0.37-0.56}Fs_{0.05-0.26}$.

Clinopyroxene grains from basalts from Mount Waite (MW4-3, MW4-4, MW4-6b and MW5-1) are characterised by Mg # ranging from 0.53 to 0.86, low to intermediate Ti (0.02-0.14), intermediate Na (0.02-0.05), very low Cr (<0.02) and intermediate Al that ranges from 0.12 to 0.40. The grains are slightly nepheline normative, and contain $Wo_{0.37-0.45}En_{0.29-0.54}Fs_{0.08-0.26}$.

Clinopyroxene clasts from the Mount Waite sandstones (MW4-1, MW4-2, MW6-2 and MW6-3) have Mg # that range from 0.51 to 0.94, very low-intermediate Ti (<0.01 to 0.03), low-intermediate Na (0.02 to 0.07), low Cr from below detection to

0.01, and low to intermediate values of Al that range from 0.02 to 0.28. The clinopyroxene clasts within the sandstones are hypersthene normative and contain $Wo_{0.37-0.45}En_{0.29-0.54}Fs_{0.08-0.26}$.

Clinopyroxene grains from within the clinopyroxenite microxenoliths from sample 0221O are characterised by Mg # ranging from 0.76 to 0.89, low Ti (<0.002), intermediate Na (~0.02), very low Cr (<0.001) and low Al that ranges from 0.01 to ~0.06. The grains are typically slightly nepheline normative, and contain $Wo_{0.48-0.50}En_{0.39-0.44}Fs_{0.05-0.12}$.

Clinopyroxene grains from gabbro samples 0116C and DP1-5c are characterised by Mg # ranging from 0.68 to 0.82, low-intermediate Ti (0.005 to 0.15), intermediate Na (0.02 to 0.04), very low Cr (0.001-0.003) and Al that ranges from 0.07 to ~0.18. The gabbros are typically olivine to slightly quartz normative, and contain $Wo_{0.26-0.45}En_{0.44-0.42}Fs_{0.08-0.24}$.

Clinopyroxene grains from the sheeted dolerite dyke complex (samples 0119A, MI-3B and DB1-1) have Mg # that range from 0.68 to 0.96, low-intermediate Ti (0.01 to 0.06), intermediate Na (0.02 to 0.03), low-intermediate Cr (0.01-0.04) and Al that ranges from low values of ~ 0.06 to intermediate values of 0.27. The sheeted dolerite dykes range from nepheline normative (0119A); through olivine normative (DB1-1); to hypersthene normative. The clinopyroxenes contain $Wo_{0.68-0.96}En_{0.39-0.57}Fs_{0.06-0.18}$.

Clinopyroxene grains from the Douglas Bay basalts (DB1-7) have Mg # that range from 0.67 to 0.86, intermediate Ti (0.03 to 0.07), intermediate Na (0.02 to 0.04), low Cr (0.004-0.02) and intermediate values of Al that range from 0.16 to 0.26. The basalts from Douglas are olivine normative and contain $Wo_{0.39-0.40}En_{0.40-0.52}Fs_{0.09-0.20}$.

Clinopyroxene clasts from the Mawson Point sandstones (MP1-2, MP1-4, MP1-6, MP1-7) have Mg # that range from 0.50 to 0.89, low-intermediate Ti (0.01 to 0.04), low Na (0.01 to 0.02), low Cr from below detection to 0.02, and low to intermediate values of Al that range from 0.01 to 0.22. The clinopyroxene clasts within the sandstones range from hypersthene to olivine normative and contain $Wo_{0.32-0.50}En_{0.33-0.54}Fs_{0.07-0.34}$.

Figure 3.3 Clinopyroxene major element diagrams of samples from Davis Point: (A) Ti *vs.* Mg #; (B) Na *vs.* Mg #; (C) Cr *vs.* Mg #; (D) Al *vs.* Mg #; (E) Ti *vs.* Al; (F) Na *vs.* $Al_{(M1)}$; (G) $Al_{(T)}$ *vs.* $Al_{(M1)}$. All axes are cation proportions. Data from Appendix A. Complete dataset shown in grey symbols for comparison. Mg # as defined in text.

Figure 3.4 Clinopyroxene major element diagrams of samples from Double Point: (A) Ti *vs.* Mg #; (B) Na *vs.* Mg #; (C) Cr *vs.* Mg #; (D) Al *vs.* Mg #; (E) Ti *vs.* Al; (F) Na *vs.* $Al_{(M1)}$; (G) $Al_{(T)}$ *vs.* $Al_{(M1)}$. All axes are cation proportions. Data from Appendix A. Complete dataset shown in grey symbols for comparison. Mg # as defined in text.

Figure 3.5 Clinopyroxene major element diagrams of samples from Mount Waite: (A) Ti *vs.* Mg #; (B) Na *vs.* Mg #; (C) Cr *vs.* Mg #; (D) Al *vs.* Mg #; (E) Ti *vs.* Al; (F) Na *vs.* $Al_{(M1)}$; (G) $Al_{(T)}$ *vs.* $Al_{(M1)}$. All axes are cation proportions. Data from Appendix A. Complete dataset shown in grey symbols for comparison. Mg # as defined in text.

Figure 3.6 Clinopyroxene major element diagrams of samples from other localities: (A) Ti *vs.* Mg #; (B) Na *vs.* Mg #; (C) Cr *vs.* Mg #; (D) Al *vs.* Mg #; (E) Ti *vs.* Al; (F) Na *vs.* $Al_{(M1)}$; (G) $Al_{(T)}$ *vs.* $Al_{(M1)}$. All axes are cation proportions. Data from Appendix A. Peridotite data from Wertz (2003). Complete dataset shown in grey symbols for comparison. Mg # as defined in text.

3.3.2 Clinopyroxene Trace-element Geochemistry

The trace-element compositions of clinopyroxene grains are given in Appendix C. Chondrite-normalised trace-element and multi-element patterns are shown in Figures 3.7 to 3.13.

Clinopyroxene clasts from sandstone samples DLP1b-5a and MW6-2 show broadly similar REE patterns, with a slight depletion in LREE's (~0.1 to 10 times chondrite), and with a slight enrichment in HREE's (up to 150 times chondrite). At higher REE concentrations, a distinct negative Eu anomaly can be seen (Eu/Eu* = 0.15 to 0.67 (DLP1b-5a) and 0.24 to 0.58 (MW6-2) where the size of the Eu anomaly (Eu/Eu*) is given by Eu_N/ ((Sm_N + Gd_N)/2), using chondrite values of Sun and McDonough (1995). The individual clinopyroxene measurements show a significant degree of scatter, with variability of up to an order of magnitude between measurements. From the multi-element spider diagram it can be seen that the clinopyroxene clasts have concentrations of most elements approximately 10 times chondrite, however these have slightly lower concentrations of large ion lithophile elements (LILE's) such as Cs, Rb and Ba. Strong negative peaks are observed for Ni and Pb, (~0.01-0.1 times chondrite) and to a lesser extent Nb (~1-0.1 times chondrite). La_N/Yb_N values vary from 0.07 to 0.78 (MW6-2) and 0.14 to 0.40 (DLP1b-5a)

Sample MI-3B from the sheeted dolerite dyke complex exposed in the north of the island shows a similar REE trend, although at lower absolute element abundances, and less variability within the clinopyroxene grains. The REE pattern is characterised by a slight depletion in LREE's (~0.5 to 1.5 times chondrite), with a slight enrichment in HREE's (up to 10 times chondrite). At higher REE concentrations (~10 times chondrite), a distinct negative Eu anomaly can be seen, with Eu/Eu* values ranging from 0.41 to 0.56. The multi-element spider diagram has an overall positive slope. It can be seen that the clinopyroxene grains have very low concentrations of Cs, Rb and Ba, ~0.01 times chondrite, which steadily increases in order of decreasing incompatibility to concentrations of ~5 times chondrite at Cs. The sample contains anomalously low concentration of Pb (~0.01 times chondrite). The multi-element pattern shows concentrations of up to 10 times chondrite for high field strength (HFS) elements such as Zr, Hf, Y, and show a strongly negative Ni spike. La_N/Yb_N values range from 0.22 to 0.56.

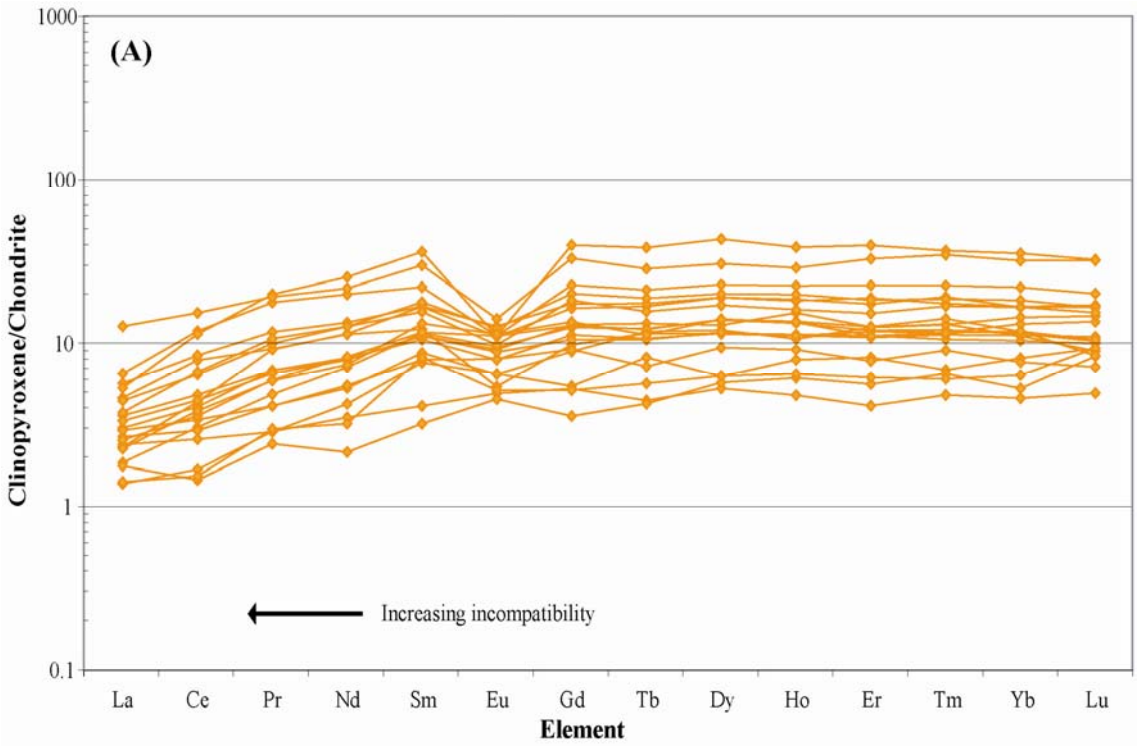

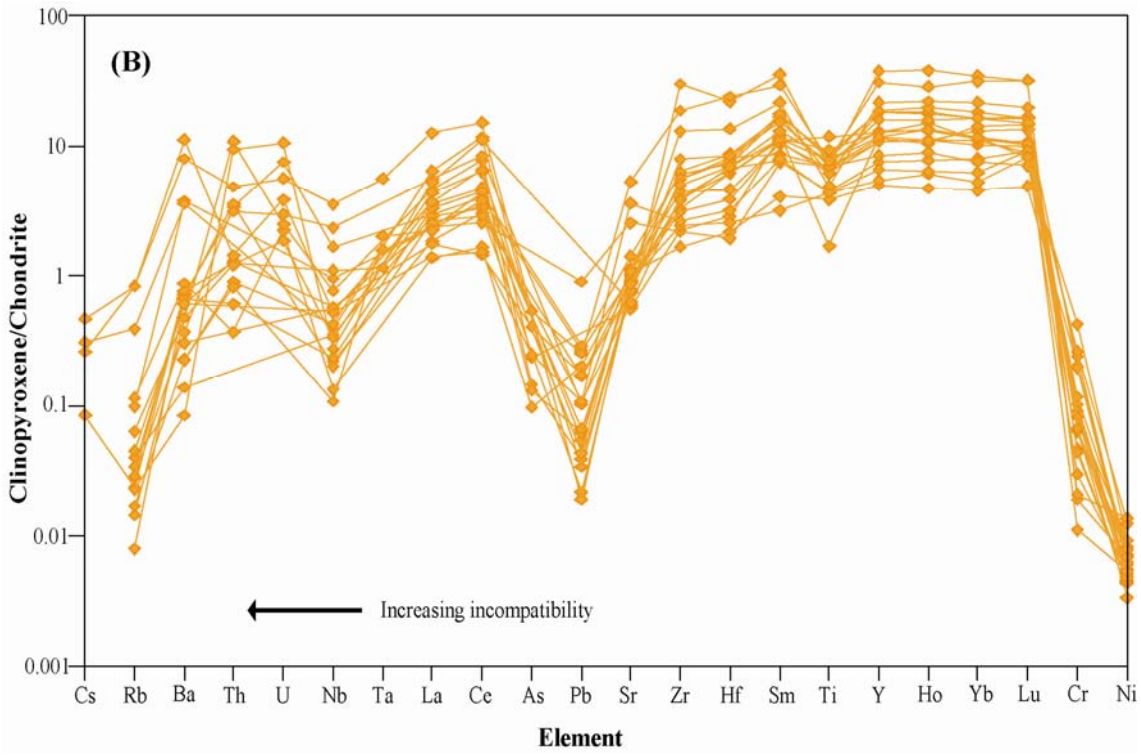

Figure 3.7 Chondrite-normalised clinopyroxene REE profiles (A) and multi-element chondrite-normalised spider diagrams (B) for sandstone DLP1b-5a. Data from Appendix C. Chondrite values from Sun and McDonough (1995).

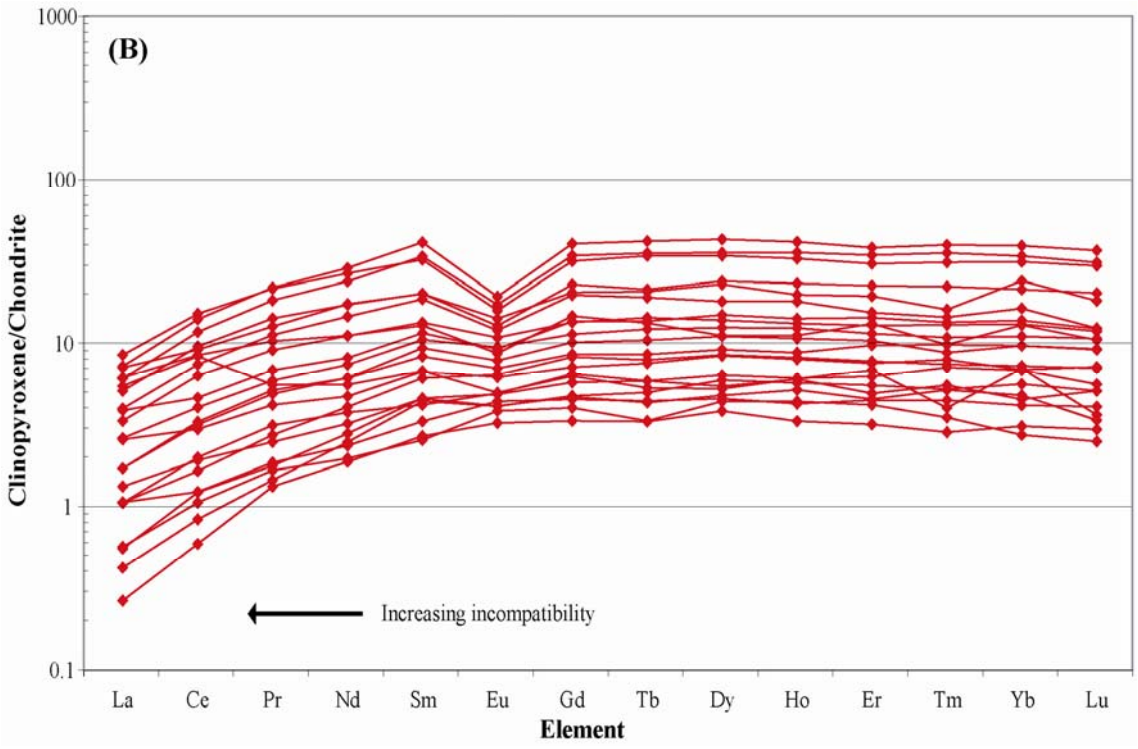

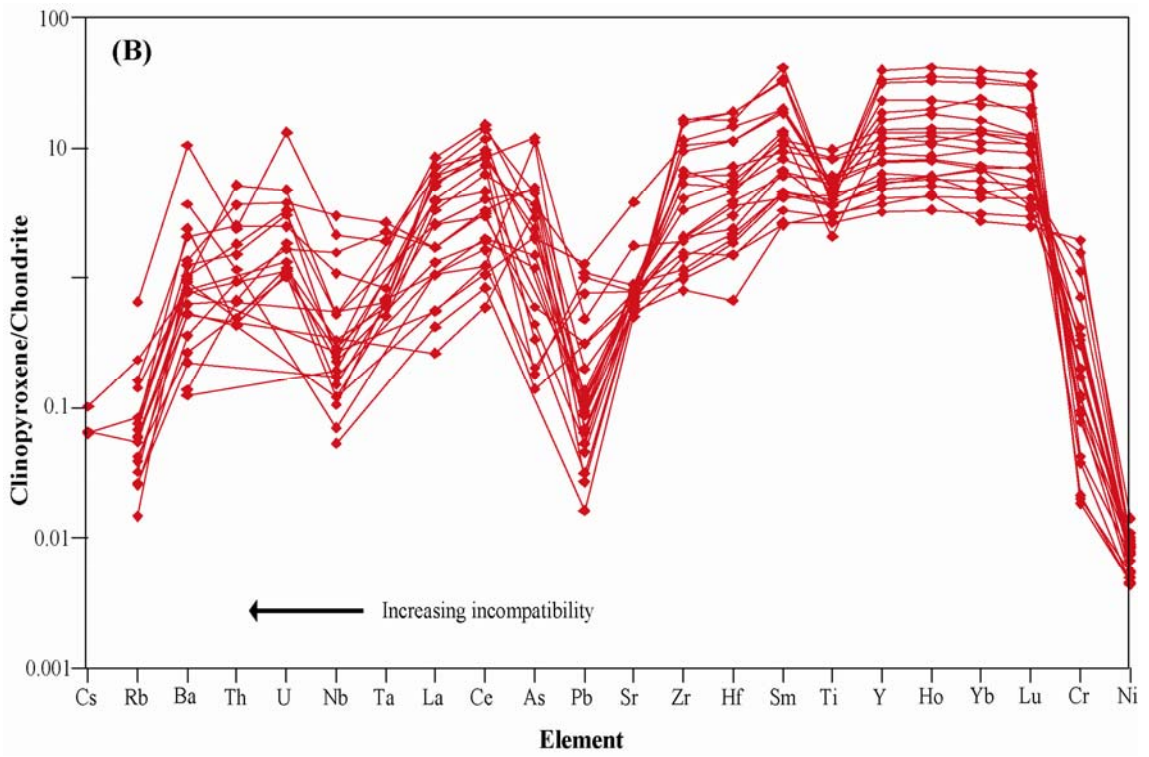

Figure 3.8 Chondrite-normalised clinopyroxene REE profiles (A) and multi-element chondrite-normalised spider diagrams (B) for sandstone MW6-2. Data from Appendix C. Chondrite values from Sun and McDonough (1995).

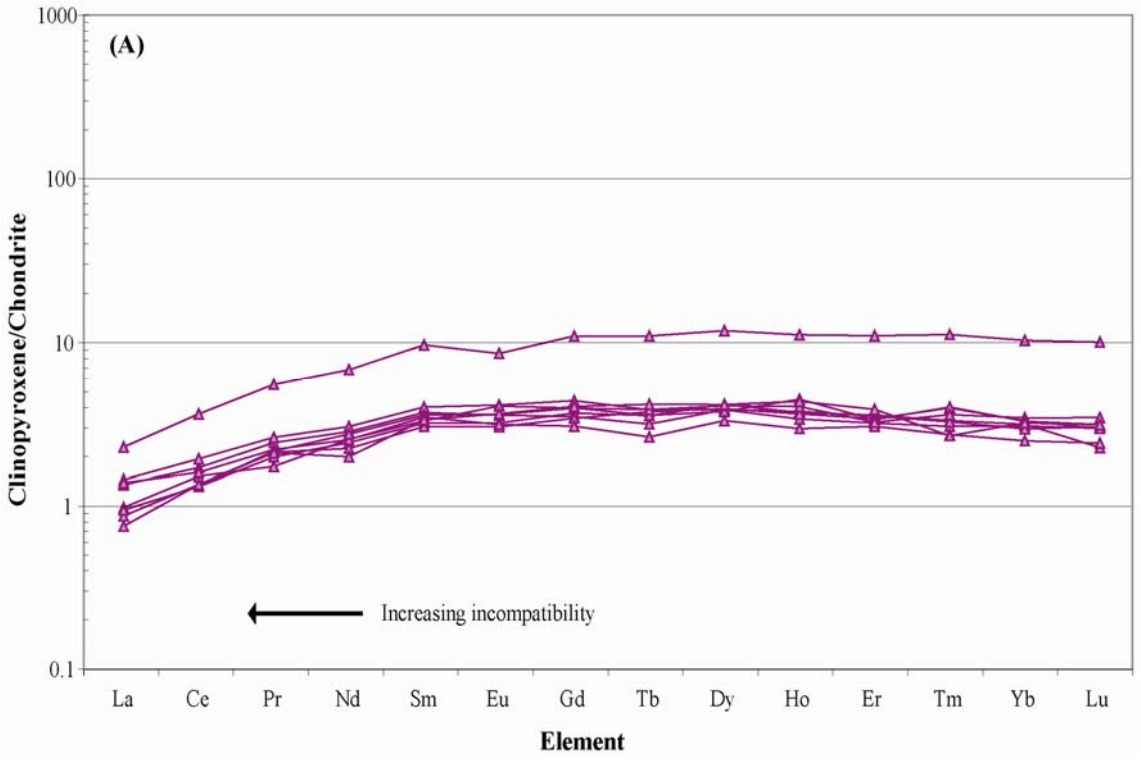

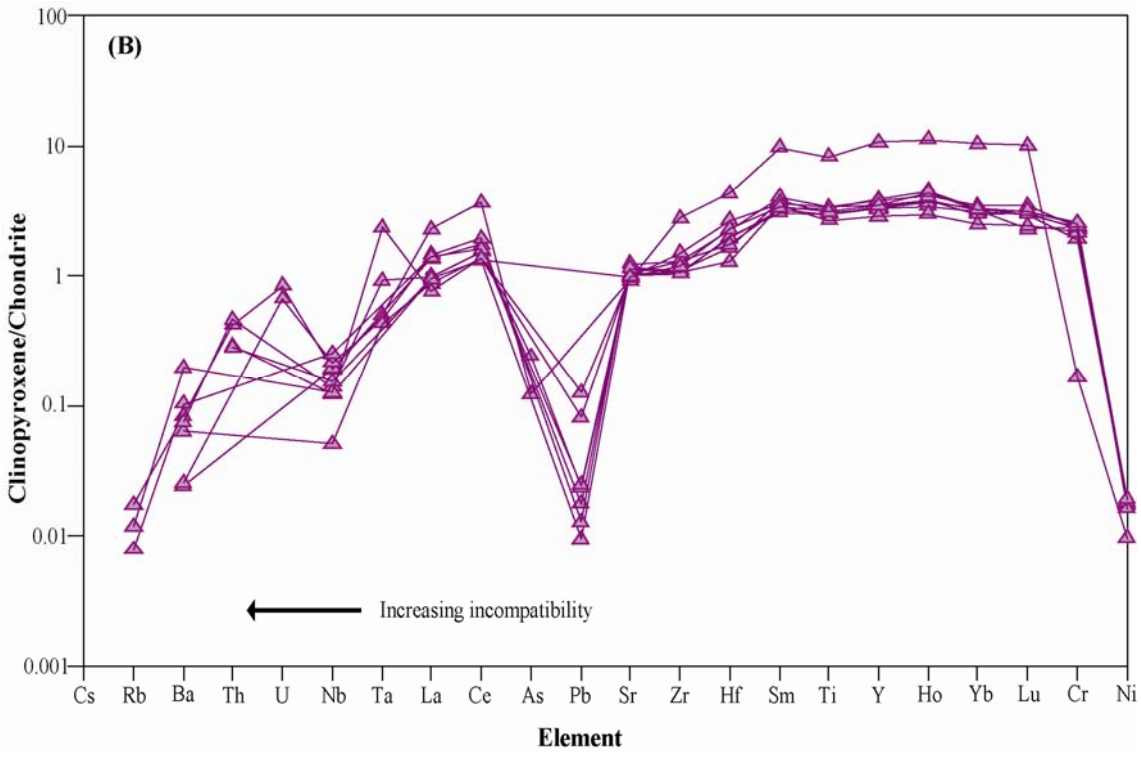

Figure 3.9 Chondrite-normalised clinopyroxene REE profiles (A) and multi-element chondrite-normalised spider diagrams (B) for sheeted dolerite dyke sample MI-3B. Data from Appendix C. Chondrite values from Sun and McDonough (1995).

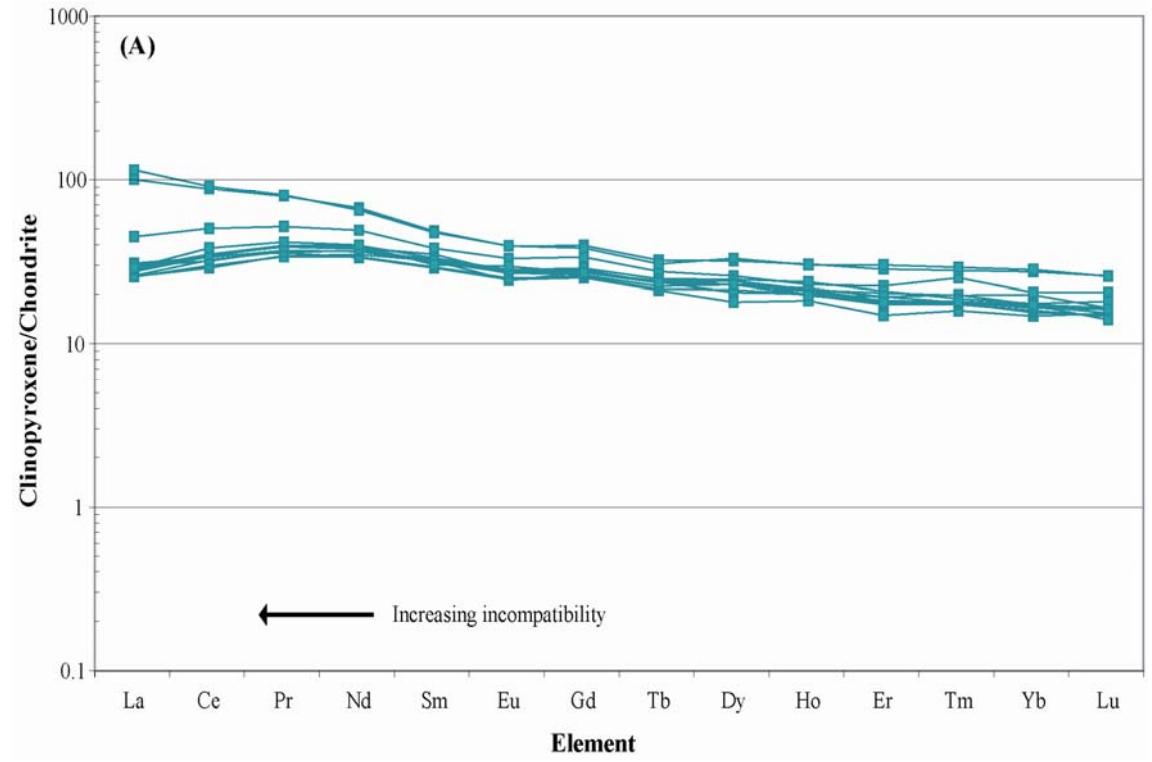

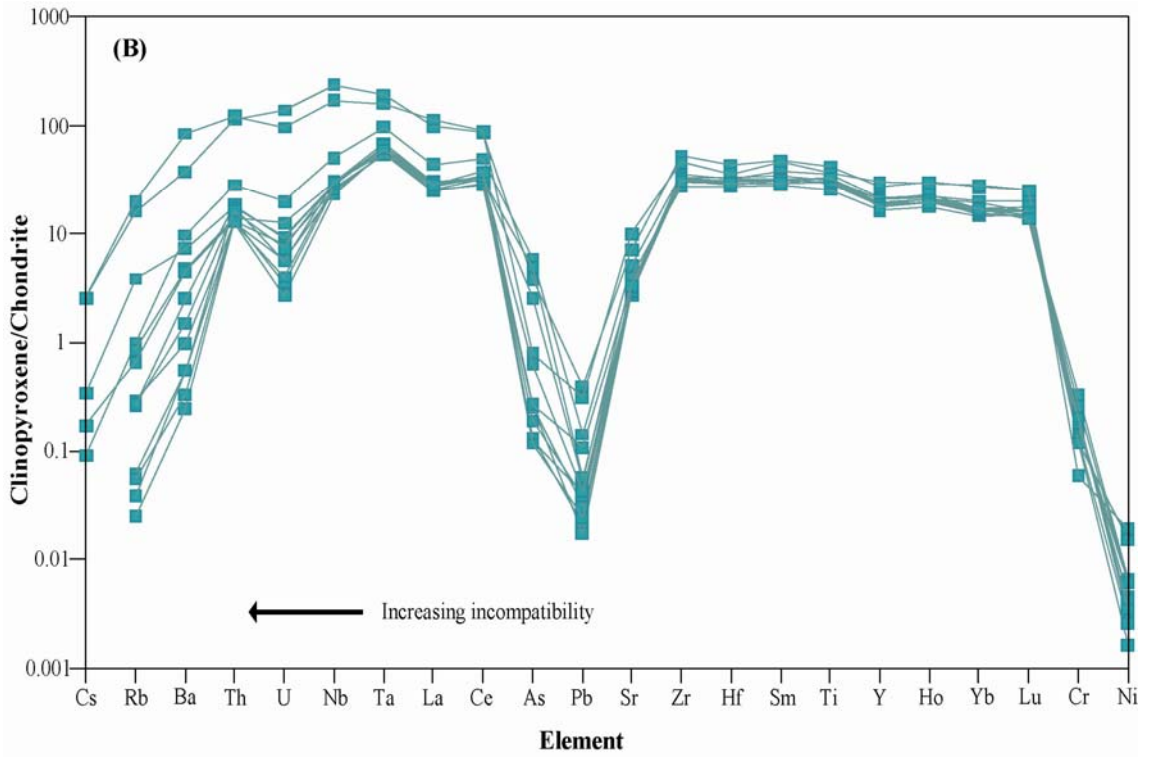

Figure 3.10 Chondrite-normalised clinopyroxene REE profiles (A) and multi-element chondrite-normalised spider diagrams (B) for pillow basalt sample MW4-3. Data from Appendix C. Chondrite values from Sun and McDonough (1995).

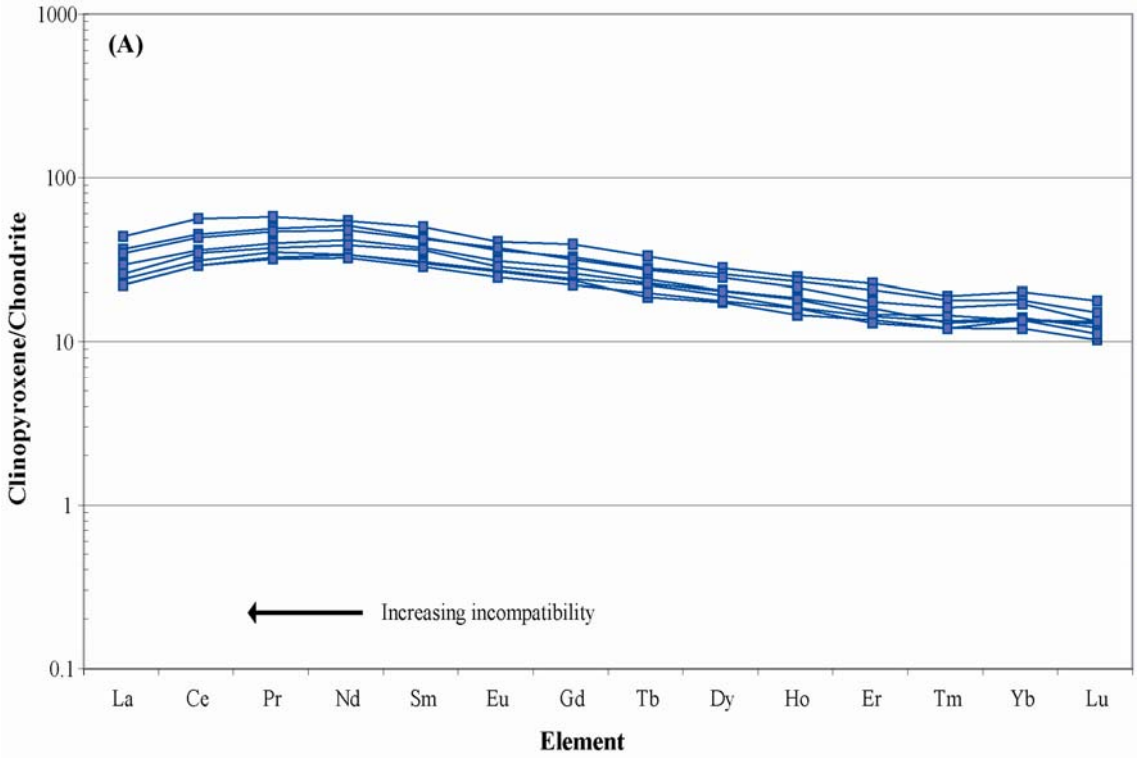

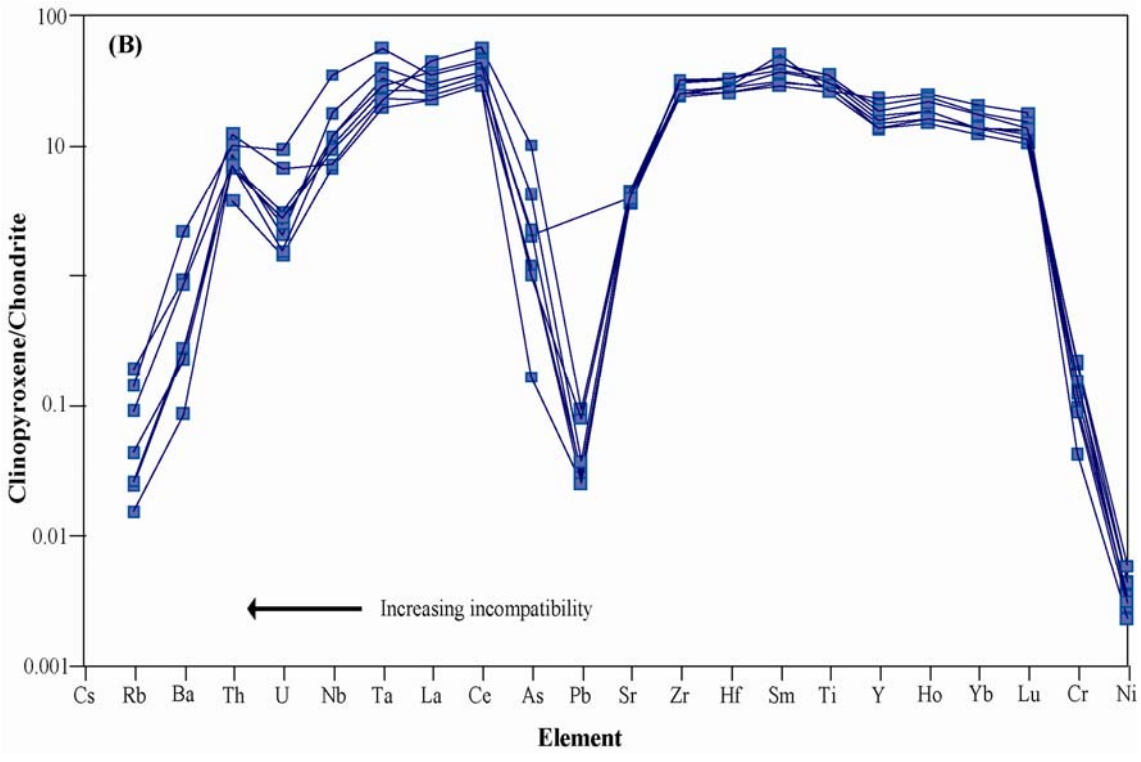

Figure 3.11 Chondrite-normalised clinopyroxene REE profiles (A) and multi-element chondrite-normalised spider diagrams (B) for tabular basalt sample DLP3-11. Data from Appendix C. Chondrite values from Sun and McDonough (1995).

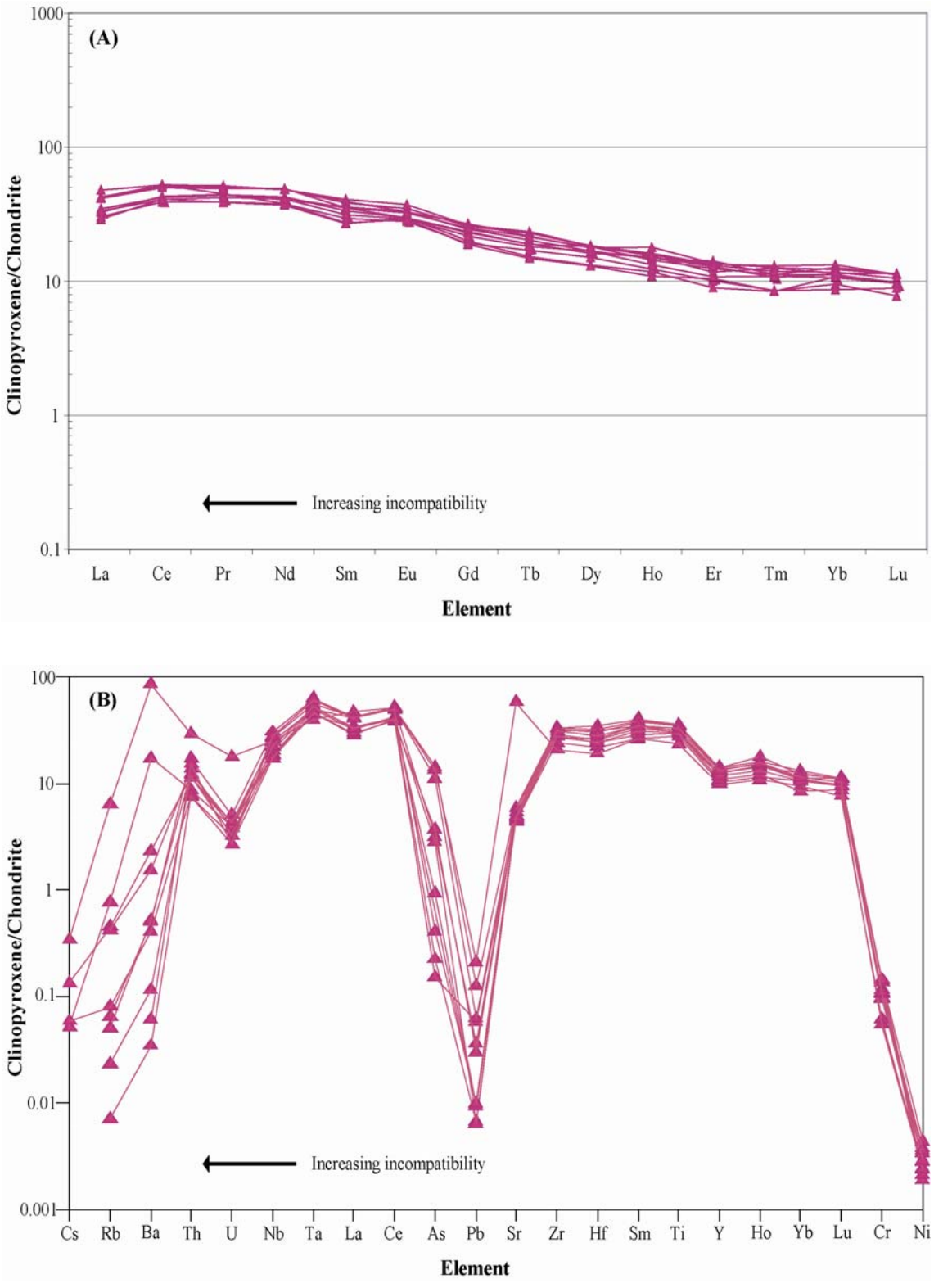

Figure 3.12 Chondrite-normalised clinopyroxene REE profiles (A) and multi-element chondrite-normalised spider diagrams (B) for hypabyssal dolerite sample DVP2-3. Data from Appendix C. Chondrite values from Sun and McDonough (1995).

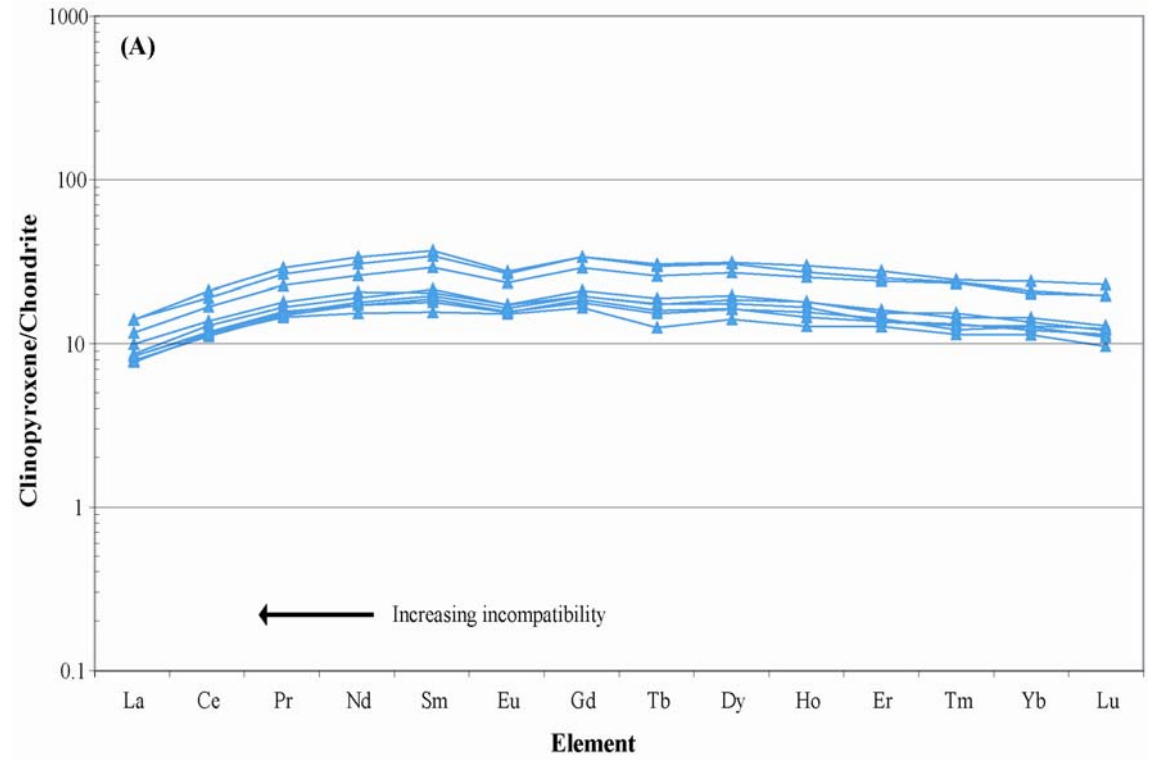

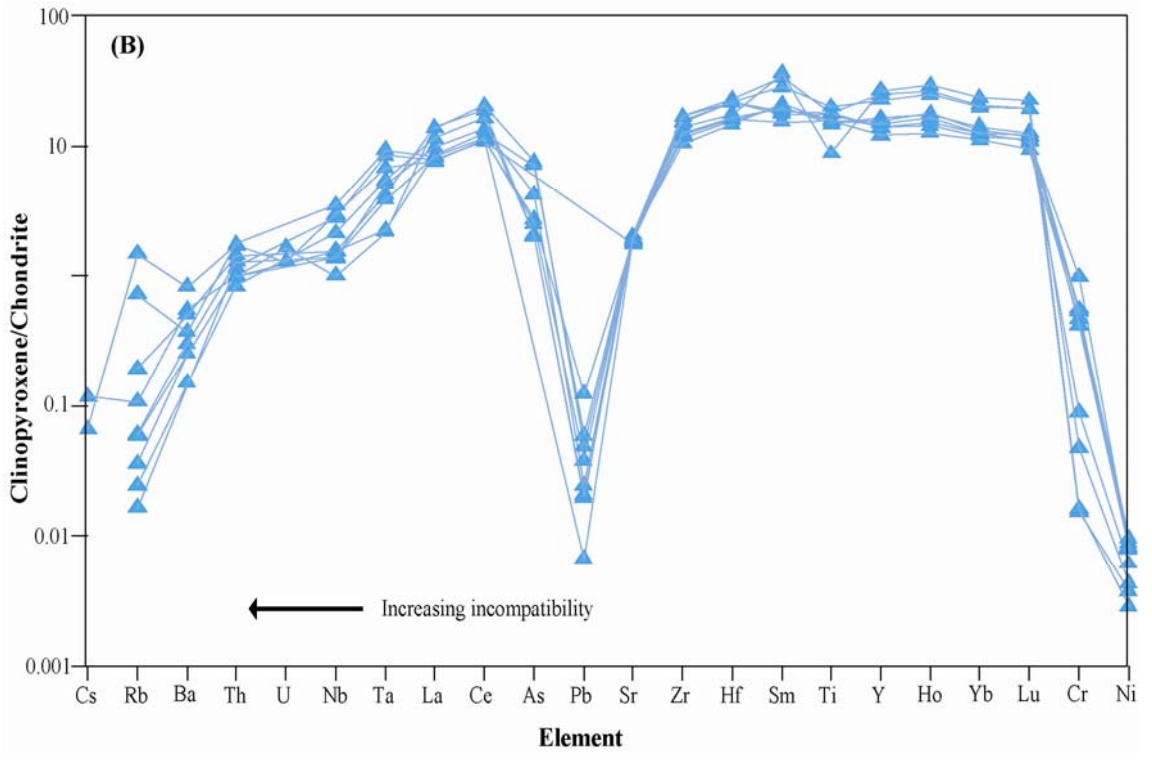

Figure 3.13 Chondrite-normalised clinopyroxene REE profiles (A) and multi-element chondrite-normalised spider diagrams (B) for hypabyssal dolerite sample DVP1-13. Data from Appendix C. Chondrite values from Sun and McDonough (1995).

Basalt samples MW4-3, DLP3-11, and hypabyssal dolerite sample DVP2-3 show similar REE trends, with concentrations of LREE's of ~100 times chondrite, gently tapering off to ~ 10 times chondrite at the HREE's. The multi-element spider diagrams follow the same overall trend as the sheeted dolerite dyke sample, but at much higher concentrations of ~ 100 times chondrite. La_N/Yb_N values vary between 2.1 and 4.5 (MW4-3); 1.6 to 2.2 (DLP3-11) and 2.7 to 5.0 (DVP2-3). The size of the Eu anomaly ranges from 0.41 to 0.52 (MW4-3) 0.46 to 0.51 (DLP3-11) and 0.50 to 0.63 (DVP2-3)

Sample DVP1-13 is a hypabyssal dolerite, and shows the same trends as the basalt and previous hypabyssal dolerite sample in both the REE and multi-element diagrams, however has much lower REE concentrations of ~10 times chondrite. La_N/Yb_N values range from 0.58 to 0.69. The negative Eu anomaly ranges from 0.39 to 0.47.

3.4 Discussion

3.4.1 Comparison of Major and Trace-elements

From Figures 3.3-3.7, clinopyroxene clasts within sedimentary rocks typically plot at Mg # ranging from ~0.51 to 0.94, very low to intermediate Ti compositions, low-intermediate Na up to ~0.3, very low Cr compositions and ranges of Al up to ~ 0.20. Basalts and dolerites typically show similar Mg # that range from ~0.55 to 0.88, however show Ti concentrations of ~0.08 to 0.18, with Na and Al concentrations in excess of 0.3. It can be seen that there is very little overlap between the sedimentary units and interbedded basalts. Similarly, clinopyroxene grains from within the clinopyroxenite microxenoliths show very low Ti, Na, Cr and Al contents, and show no overlap with the sedimentary rocks.

Clinopyroxene grains from gabbro and sheeted dolerite dyke complex samples are typically characterised by Mg # ranging from 0.68 to 0.96, low-intermediate Ti and Na contents and Al that ranges from ~0.07 to ~0.27. The compositions of these rock types show considerable overlap with the sedimentary units.

In summary, detrital clinopyroxene major and trace-element geochemistry shows little overlap with clinopyroxene grains within the interbedded volcanic sequences, excluding the proximal volcanism as a likely source for the sediment. Comparison of detrital clinopyroxene clasts with peridotite clinopyroxene data from

Wertz (2003) shows a lack of peridotite signature in the sandstones, suggesting that upper mantle provided very little (if any) input to the sediment. Overlapping major element geochemical affinities between clinopyroxene grains in the gabbro and sheeted dolerite dyke sequences from Macquarie Island with the clinopyroxene clasts in the sedimentary rocks may suggest a lower crustal rock derived provenance. Broad similarities in the overall REE patterns between MI-3B from the sheeted dolerite dyke exposed in the north of the island and the sedimentary units further supports this.

3.4.2 Geochemical Basalt Correlations

In the Chapter 2, tentative basalt correlations between samples DVP1-14a and MW4-6b; and MW4-4 and MW5-1 were made based on lithostratigraphy and petrography.

Further examination of the major element geochemistry between samples DVP1-14a and MW4-6b; and MW4-4 and MW5-1 shows remarkable similarities. In Figure 3.14, distinct overlap between samples DVP1-14a and MW4-6b; and MW4-4 and MW5-1 can be seen with Ti, Cr, Fe^{2+} and $Al_{(M1)}$ when plotted against Mg #.

Given the degree of overlap, it can be concluded that there is a strong correlation between the samples, and thereby confirms the stratigraphic correlation.

Comparison of clinopyroxene geochemistry from other basalt and dolerite samples from within the stratigraphic columns show that the above correlations are unique, with all other samples showing different geochemical character.

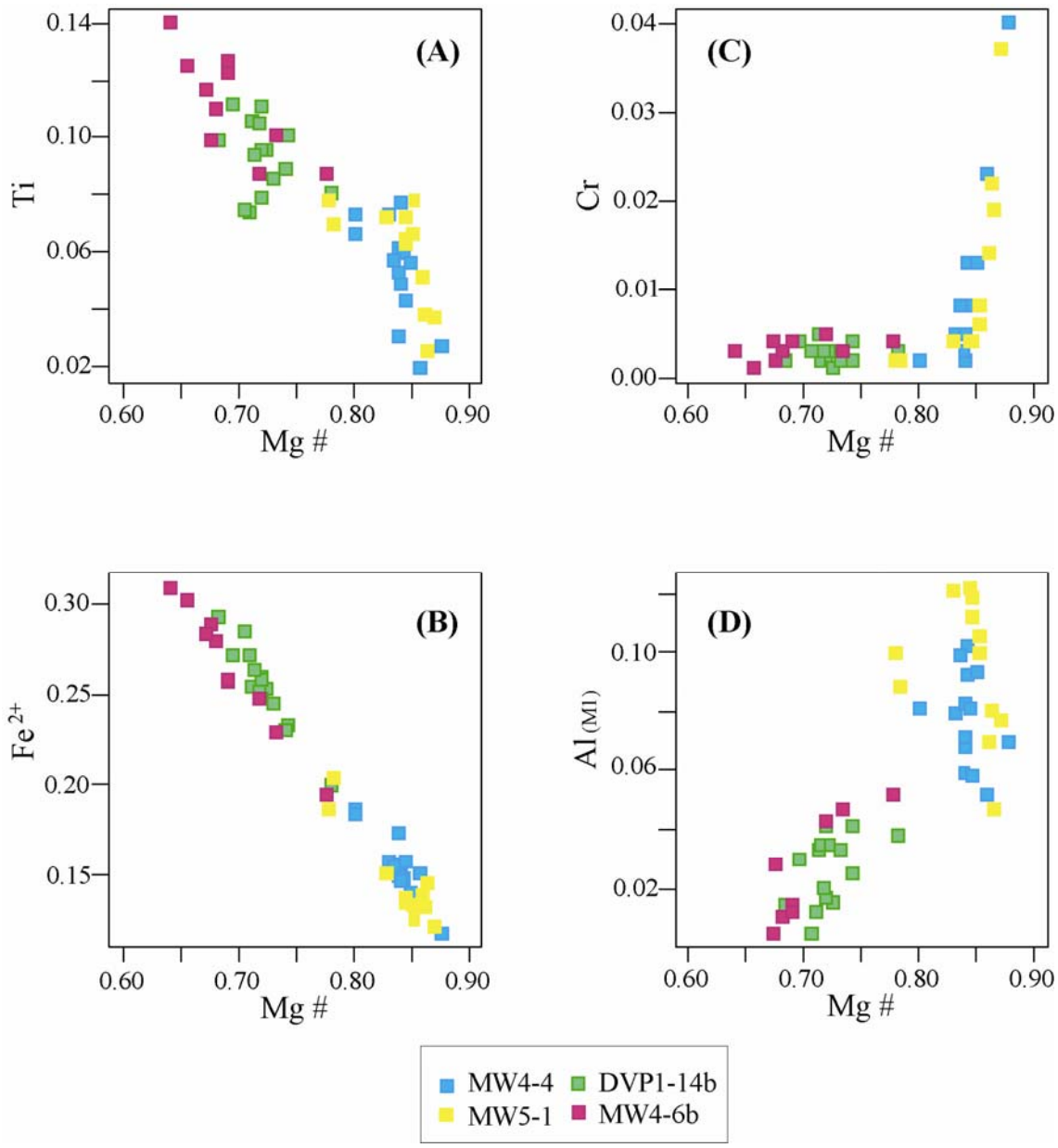

Figure 3.14 Clinopyroxene major element diagrams showing correlations between basalt samples (A) Ti *vs.* Mg #; (B) Fe^{2+} *vs.* Mg #; (C) Cr *vs.* Mg #; (D) $Al_{(M1)}$ *vs.* Mg #. All axes are cation proportions. Mg # as defined in text.

Chapter 4 Zircon Geochemistry and Geochronology

4.1 Introduction

Zircon is a widespread heavy mineral in many sediments and sedimentary rocks due to their chemical and mechanical resistance, however they are relatively rare in mafic rocks, commonly only found in plagiogranites and pegmatititic rocks.

Heavy mineral separation was performed on five sandstones from across the island, two from the detailed stratigraphy (DLP1b-5a and MW6-2) and three from elsewhere on the island (Mawson Point: MP1-4; Cormorant Point: CP1-5; and Mount Martin: MM1-1; Figure 1.1). In this study, zircon grains were analysed by Laser Ablation – Inductively Coupled Plasma – Mass Spectrometry (LA-ICP-MS) for U-Pb isotope and trace-elements to determine the age and rock type of the source rocks, and to determine if the sediments were supplied by the same source area.

The analyses of the zircons outlined were conducted at the Geochemical Analysis Unit housed in the Australian Research Council (ARC) National Key Centre for Geochemical Evolution and Metallogeny of Continents (GEMOC) based in the Department of Earth and Planetary Sciences at Macquarie University, Sydney.

4.2 Methods

4.2.1 Sample Preparation

Zircon and heavy mineral concentrates for each sample were prepared by Geotrack, Melbourne using high-density liquids and Franz magnetic separation. Zircon grains from each sample were hand-picked from the heavy mineral concentrates using a Leica binocular microscope. Grains were selected to include the ranges of sizes, shapes and colours present within each sample. The grains were mounted in epoxy resin blocks, and the surface of the grain mount polished to expose the zircon grains. Prior to analysis, notable grain features and internal zoning were documented for each zircon using combined back-scattered electron/ cathodoluminescence (BSE/CL) imaging using a Cameca SX-100 electron microprobe (EMP) with operating conditions of 15 kV accelerating voltage and 20 nA beam current. Grain mounts containing the samples and

calibration standards were cleaned in 1 N nitric acid for ~ 10 minutes prior to U-Pb dating to remove surface Pb contamination.

4.2.2 Zircon Major Element Analyses by Electron Microprobe

Major element oxides (SiO_2, ZrO_2) and minor oxides (Y_2O_3, HfO_2) of the zircons were determined using a Cameca SX-100 electron microprobe, equipped with five wavelength dispersive spectrometers (WDS) and a PGT energy dispersion system (EDS). SiO_2 was analysed on Kα emission lines, whilst ZrO_2, HfO_2 and Y_2O_3 were analysed on Lα emission lines. An accelerating voltage of 15 keV, a beam current of 20 nA and a focused beam size of 1-2 μm were utilised. Counting times of 20 seconds were used for both peak and background determination of SiO_2 and ZrO_2, and 60 seconds for HfO_2 and Y_2O_3. Natural mineral and synthetic standards were analysed for the elements cited in brackets – zircon (Zr, Si), yag (Y), Hf wire (Hf). The PAP matrix correction procedure (Pouchou and Pichoir, 1984) was applied to convert the raw X-ray intensity data to weight percent oxide. Lower limits of detection and precision data are presented in Table 4.1.

Table 4.1 Lower limits of detection and precision data (expressed as relative standard deviations, RSD) for SiO_2, ZrO_2, Y_2O_3 and HfO_2 obtained by Electron Microprobe. Background measured on zircon

Element	LLD (wt %)	% rsd
SiO_2	0.03	0.19
HfO_2	0.05	0.19
ZrO_2	0.09	0.30
Y_2O_3	0.03	0.34

4.2.3 Simultaneous U-Pb Dating and Trace-element Determinations by Laser Ablation - Inductively Coupled Plasma - Mass Spectrometry

In-situ U-Pb dating and trace-element analysis of zircon grains were determined simultaneously, using a New Wave 213 nm Nd: YAG laser system, linked to an Agilent 7500s ICP-MS. The technique has been described by Jackson et al. (2004). Analyses were carried out with a beam diameter of 30-40 μm, a 5 Hz (pulses per second) repetition rate, and output energy of ~0.9 mJ per pulse. Ablation was conducted in a He atmosphere (~1 l min^{-1}). The sample + He mixture was combined with Ar (~0.9 l min^{-1})

in a teflon mixing chamber prior to being transported to the ICP. Data acquisition was performed by peak hopping (one point per isotope) in pulse counting mode. Each analysis took 180 s, with a "gas blank" measurement of the carrier gas (He) taken over the first ~50 s, before initiation of ablation of the sample for ~130 s. Data were acquired on ten isotopes for U-Pb dating; and ten isotopes for trace-element determinations, with short dwell times to provide quasi-simultaneous measurements.

Table 4.2 Operating conditions and data acquisition parameters for U-Pb isotope and trace-element determinations by LA-ICP-MS.

ICP-MS		**LA**	
Model	Agilent 7500s	Model	New Wave, 213 nm
Forward power	1350 KW	Repetition rate	5 Hz
Gas flows:		Pulse duration (FWHM)	6 ns
Plasma (Ar)	13 L min^{-1}	Focussing objective	10x, UV laser achromat, f.l. = 20 mm
Auxiliary (Ar)	0.8 L min^{-1}	Degree of defocussing	200 μm (above sample)
Carrier (He)	~1 l min^{-1}	Spot size	30-40 μm
Make-up (Ar)	~0.9 l min^{-1}	Measured pulse energy	~0.9 mJ
Data acquisition parameters			
Data acquisition protocol	Time-resolved analysis		
Scanning mode	Peak hopping, 1 point per peak		
Detector mode	Pulse counting, dead time correction applied		
Isotopes Determined	^{206}Pb, ^{207}Pb, ^{208}Pb, ^{232}Th, ^{238}U, ^{49}Ti, ^{89}Y, ^{139}La, ^{140}Ce, ^{141}Pr, ^{147}Sm, ^{151}Eu, ^{157}Gd, ^{173}Yb, ^{178}Hf		
Dwell Times	10 ms (^{208}Pb, ^{232}Th, all trace elements), 15 ms (^{206}Pb, ^{238}U), 30 ms (^{207}Pb)		
Data acquisition time	180 s (50 s gas blank, 130 s ablation of sample)		

Samples were analysed in 'runs' of 20 analyses consisting of two analyses of a gem quality GJ zircon standard for calibration of U-Pb isotopes, two analyses of synthetic glass NIST-610 standards for calibration of trace-elements respectively; one analysis of each of a Mud Tank and 91500 zircon reference materials to monitor the accuracy of the method, 10 analyses of unknowns, followed by a further two GJ zircon standards, and two NIST-610 standards. ^{178}Hf was used as an internal standard for trace-element quantification, using the electron microprobe measurements of HfO_2 (wt %) of the same zircon grains. The overall accuracy and precision of U-Pb isotope measurements were controlled by analysing two external reference standards, zircon 91500 (accepted $^{206}Pb/^{238}U$ age of 1065.4 ± 0.6 Ma, Wiedenbeck et al. (1995)); and Mud-Tank (732 ± 5 Ma, Black and Gulson (1978)), and are presented in Table 4.3. Accuracy and precision of trace-element measurements were controlled by repeat measurement of a zircon of known composition (Zircon 91500, values from Wiedenbeck et al., 2004) and are presented in Table 4.4.

Table 4.3 U-Pb isotope accuracy and precision data for the 91500 and Mud-Tank reference standards obtained by LA-ICP-MS in this study and comparison with previously reported data (Black and Gulson, 1978; Wiedenbeck et al., 1995).

91500	This study (n = 14)				Jackson et al. (2004) (n = 83)				Wiedenbeck et al. (1995)	
	Isotopic ratios		Mean age (Ma)		Isotopic ratios		Mean age (Ma)		TIMS age (Ma)	
	Mean	2 RSD	Mean	2 sd	Mean	2 RSD	Mean	2 sd	Mean	2σ
$^{207}Pb/^{206}Pb$	0.0742	2.11%	1047	43	0.0750	1.30%	1068	26	1065.4	0.3
$^{207}Pb/^{235}U$	1.8103	5.53%	1049	36	1.8491	4.40%	1063	29	-	
$^{206}Pb/^{238}U$	0.1769	5.20%	1050	50	0.1789	3.70%	1061	36	1062.4	0.4
$^{208}Pb/^{232}Th$	0.0535	3.77%	1053	39	0.0538	15.50%	1058	159	-	

Mud Tank	This study (n = 14)				Jackson et al. (2004) (n = 73)				Black and Gulson, (1978)	
	Isotopic ratios		Mean age (Ma)		Isotopic ratios		Mean age (Ma)		TIMS age (Ma)	
	Mean	2 RSD	Mean	2 sd	Mean	2 RSD	Mean	2 sd	Mean	2σ
$^{207}Pb/^{206}Pb$	0.0641	8.70%	744	183	0.0638	1.90%	735	40	-	2σ
$^{207}Pb/^{235}U$	1.0621	8.99%	735	47	1.0569	5.30%	732	28	-	2σ
$^{206}Pb/^{238}U$	0.1201	2.68%	731	19	0.1202	4.90%	731	34	732	5
$^{208}Pb/^{232}Th$	0.0380	15.18%	754	112	0.0372	9.70%	738	70	-	

Table 4.4 Trace-element accuracy and precision data for the 91500 reference standards obtained by LA-ICP-MS in this study and comparison with previously reported data (Wiedenbeck et al., 2004).

91500	Wiedenbeck et al. (2004)		This study n = 9	
(ppm)	Mean	SD	Mean	SD
Ti	6	1	4.92	0.5
Y	140	14	147	1.3
La	0.006	0.003	<LLD	<LLD
Ce	2.6	0.3	2.40	0.1
Pr	0.024	0.015	0.014	0.01
Sm	0.5	0.08	0.43	0.03
Eu	0.24	0.03	0.23	0.02
Gd	2.2	0.3	2.32	0.1
Yb	74	4	72.8	1.7
Lu	13	1	13.0	0.2
Hf	5900	300	5936	9.65E-13
Pb	15	2	16.8	1.1
Th	30	3	30.7	1.6
U	80	8	85.4	3.8

U-Pb ages were calculated from the raw signal data using the online software package GLITTER, Version 4.4 (van Achterbergh et al., 1999). The time-resolved analysis software, in which the signal intensity data for each mass and each ratio is displayed as a function of time (ablation depth) during the analysis, allows for the most stable portion of the signal to be selected for integration, thereby enabling isotopic heterogeneities such as inherited cores or inclusions to be identified and avoided. The ^{204}Pb isotope cannot be precisely measured with this technique, due to a combination of low signal and isobaric interference from ^{204}Hg contaminants in the Ar gas supply. Consequently, the common-Pb contents were evaluated using the algorithm described by Anderson (2002) where applicable. Because of low concentrations of ^{207}Pb present in young (i.e. <1 Ga) zircons and low count rates and large analytical uncertainties, the determination of the ages for 'young' zircons is based on their ^{206}Pb/^{238}U ratios.

Pb is presented as total Pb, and has been recalculated on the basis of isotopic abundances of the ^{206}Pb, ^{207}Pb and ^{208}Pb isotopes.

Concordia and Mean Square Weighted Deviation (MSWD) ages were determined using Isoplot Version 2.32 (Ludwig, 2000).

4.3 Results

4.3.1 Zircon Morphology

The morphology of the zircons within the sandstones are characterised by irregular, broken grains, ranging from mostly colourless to pale pink and rarely pale yellow. The zircons range in size from 80 to 300 μm, with the average grain size approximately 100 μm. Over 100 individual zircon grains from samples DLP1b-5a and MW6-2 from the detailed west coast section were separated and mounted, however few zircon grains were extracted from samples elsewhere on the island (CP1-5, MM1-1 and MP1-4).

BSE/CL images of the zircons are characterised by a near complete lack of crystal faces, with rare euhedral faces preserved (<1 %). The zircons dominantly show sharp irregular grain shapes (>90 %), and rarely exhibit a sub-rounded shape. No obvious zoning was discernable and grains commonly appeared fractured.

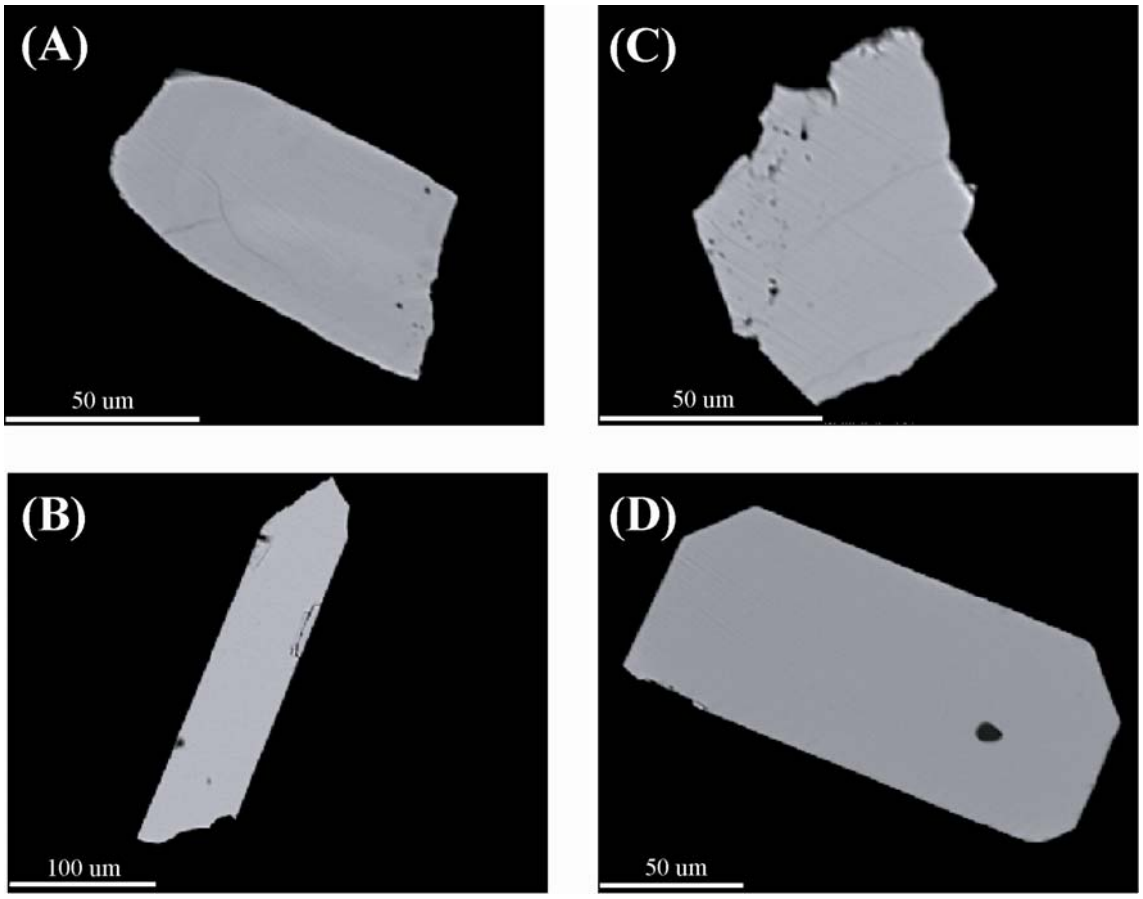

Figure 4.1 Back-scattered electron/ cathodoluminescence images of dated zircons (A) sub-rounded morphology in DLP1b-5a-48; (B) broken morphology with fractures in MW6-2-78; (C) irregular morphology in DLP1b-5a-70; (D) well developed crystal faces DLP1b-5a-105.

4.3.2 Zircon Major and Trace-element Geochemistry

The major and trace-element compositions of detrital zircons are given in Appendices D and E respectively. Zircons in the five samples have similar ZrO_2 contents that range from 60.29 to 68.63 wt %. The SiO_2 composition varies from 26.43 to 32.72 wt %. The zircons have HfO_2 contents of 0.90 to 2.06 wt %, and Y_2O_3 compositions of less than detection to 1.87 wt %.

The chondrite-normalised patterns are similar for all five sandstones (Figure 4.2). The zircons are characterised by chondrite-normalised REE patterns enriched in HREE's, with a pronounced positive Ce anomaly and a negative Eu anomaly.

Figure 4.2 Chondrite-normalised trace-element patterns using chondrite values recommended by Sun and McDonough (1995). (A) Sample DLP1b-5a; (B) CP1-2; (C) MM1-1; (D) MW6-2; (E) MP1-4. Data from Appendix E.

Zircons from samples DLP1b-5a, MW6-2, CP1-2 and MM1-1 have Th contents from as low as ~3 ppm, to moderate concentrations of ~250 ppm. Significant variations were detected within samples, with DLP1b-5a recording an extreme value of 747 ppm. Sample MP1-4 has much lower Th contents ranging from ~3-12 ppm. A similar trend is observed with U, with all samples except MP1-4 showing significant variability within samples, from ~5 to 500 ppm. Sample MP1-4 show much lower concentrations from ~5-25 ppm.

Concentrations of Y fall in the range from hundreds to thousands of ppm. Concentrations of Yb range from ~113-2700 ppm, with the highest concentrations in DLP1b-5a, MW6-3 and MM1-1. Samples CP1-2 and MP1-4 show maximum Yb concentrations of ~650 ppm. Zircons from all samples contain comparable Ti contents of ~5-35 ppm. Most concentrations of La and Pr fall below the detection limit. Concentrations of Pb are generally below detection, however may reach concentrations up to ~142 ppm (CP1-2). Concentrations of Gd are typically ~5-100 ppm; higher contents reach ~230 ppm in MW6-2.

There is a slight increase of incompatible element compositions from samples CP1-2, MP1-4, MM1-1, DLP1b-5a to MW6-2 (average $\Sigma_{(Sm\text{-}Lu)}$ = 539, 557, 711, 810 and 917 respectively).

Th/U ratios from ~0.4 to 1 are typical of samples DLP1b-5a, MW6-2, CP1-2 and MM1-1, however may reach as high as 1.47 (DLP1b-5a). Sample MP1-4 maximally reaches ratios of 0.78. The Yb/Sm ratio ranges from 35 (CP1-2) up to 293 (MW6-2), however is typically in the range of ~80 to 250.

A positive Ce anomaly is typical of the zircons analysed in this study, ranging from ~3 to 50, with one zircon from MW6-2 reaching as high as 96. The size of the Ce anomaly (Ce/Ce*) is given by $Ce/Ce^* = Ce_N / ((La_N + Pr_N)/2)$. All zircons have a slight negative Eu anomaly, ranging from 0.07 to 0.33. The size of the Eu anomaly (Eu/Eu*) is given by $Eu/Eu^* = Eu_N / ((Sm_N + Gd_N)/2)$. The depth of the Eu anomaly shows a slight positive correlation with Y (Figure 4.3).

The discrimination diagram (Figure 4.4A) proposed by Belousova et al. (2002) using Y versus U content show that most of the zircons have higher Y and slightly lower U contents than the main array from kimberlitic - granitic composition. The zircons appear to plot their own field (with a few outliers) between the main array and the nepheline syenite and syenite pegmatite fields, and clearly do not plot within the basic rock field.

A second discrimination diagram (Figure 4.4B) proposed by Belousova et al. (2002) using the Y content and the size of the Ce anomaly shows that there is a general positive correlation between the amplitude of the Ce anomaly and the Y content. The zircons plot within the larvakite, lamproite, syenite pegmatite and granite fields, and again do not plot within the basic rock field.

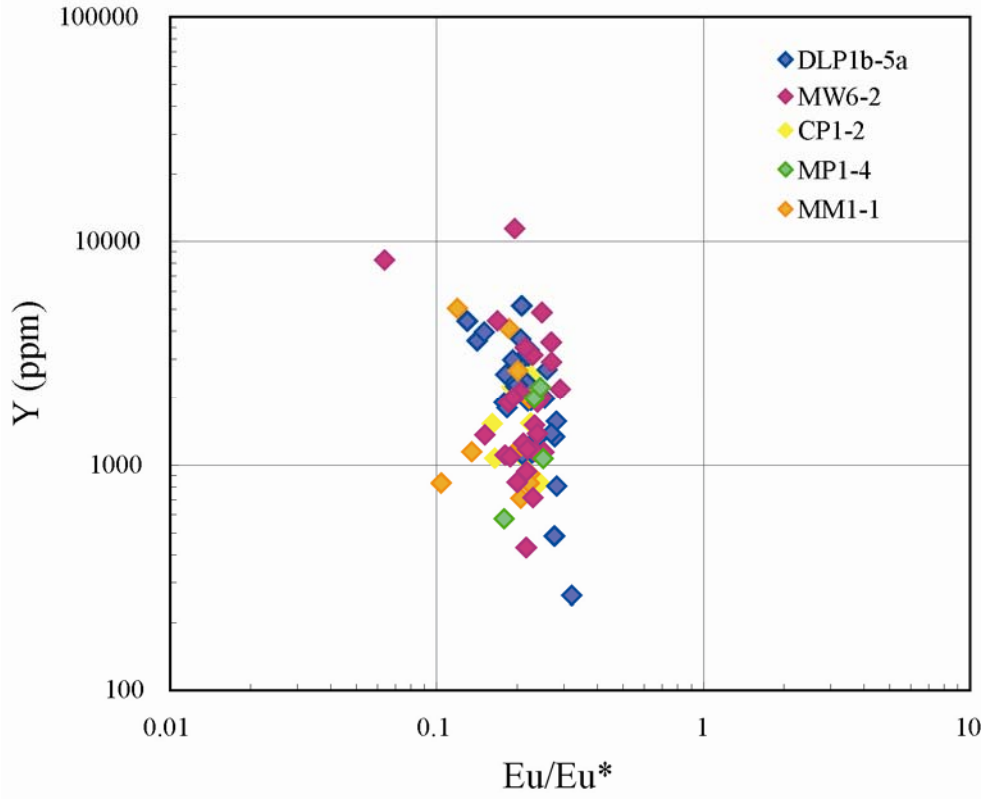

Figure 4.3 Y (ppm) *vs*. Eu/Eu*. Data from Appendix E. Eu/Eu* as defined in text.

4.3.3 Zircon U-Pb Geochronology

U-Pb ages for detrital zircons were obtained from five samples (DLP1b-5a, MP1-4, CP1-5, MM1-1, and MW6-2) and are given in Appendix F. Concordia diagrams, weighted average and $^{206}Pb/^{238}U$ age cumulative probability diagrams are shown for each sample in Figures 4.4 to 4.8.

Zircon analyses from DLP1b-5a (n = 30, 0 rejected) yielded a concordia age of 27.25 ± 0.31 Ma (2σ), although a distribution of ages from 23 ± 6 Ma to 32 ± 4 Ma (2σ) is observed. Most of the data points are concordant or plot close to the concordia, giving a MSWD of concordance of 0.38. The probability of concordance is 0.54. The zircons have Th/U mainly from ~ 0.4-0.93, with a few exceptions that had ratios of 1.38 and 1.48.

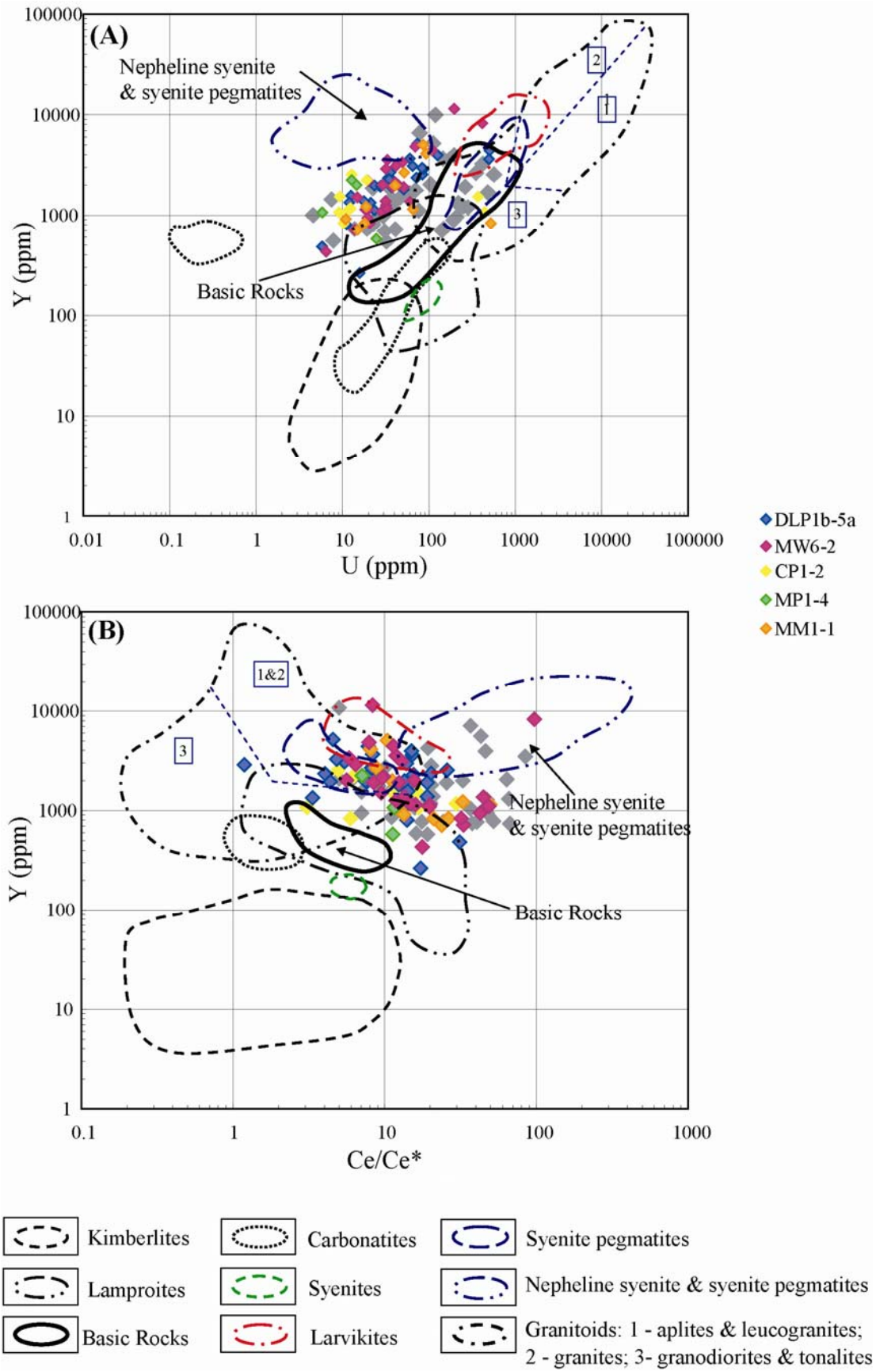

Figure 4.4 Rock type discrimination diagrams using fields by Belousova et al. (2002). (A) Y *vs*. U; (B) Y *vs*. Ce/Ce*. All axes in ppm except Ce/Ce*, as defined in text. Data from Appendix E. Oceanic gabbro zircon trace-element dataset from Kaczmarek et al. (2008) shown in grey symbols for comparison.

All twenty-seven analyses of zircon from MW6-2 gave a weighted mean $^{206}Pb/^{238}U$ age of 27.16 ± 0.57 Ma (2σ), with a MSWD of 3.6 and probability of less than 0.001. Ages show a range from 25.5 ± 0.8 Ma through to 33 ± 2 Ma (2σ). The zircons have Th/U mainly from ~ 0.33-0.88, with a few exceptions that had ratios of 1.01 and 1.25.

A small number of analyses were performed on zircons from MP1-4 (n = 4, 0 rejected) gave a concordia age of 30.9 ± 1.7 Ma (2σ). The data points are largely concordant, giving a MSWD of concordance of 0.36. The probability of concordance is 0.55. A distribution of ages from 30 ± 6 Ma to 47 ± 10 Ma (2σ) is observed. Ratios of Th/U range from 0.45 to 0.78.

Ten analyses of zircon from MM1-1 show two age populations, with one analysis obtained with a $^{206}Pb/^{238}U$ age of 1200 ± 22 Ma (2σ), with a young population (n = 9) giving a weighted mean $^{206}Pb/^{238}U$ age of 27.08 ± 0.76 (2σ), with a MSWD of 1.9 and probability of less than 0.062. Ages within the 'young' population range from 24 ± 4 Ma to 28.3 ± 1 Ma (2σ). The 'young' population of zircons contained Th/U of 0.5-1.0, the single 1200 Ma grain had a ratio of 0.53.

Zircon analyses from CP1-2 (n = 8) also show two age populations, with one analysis obtained with a $^{206}Pb/^{238}U$ age of 1568 ± 36 Ma (2σ), with a young population (n = 7) yielding a weighted mean $^{206}Pb/^{238}U$ age of 32.9 ± 2.2 (2σ), with a MSWD of 0.52 and probability of less than 0.80. Ages within the 'young' population range from 32 ± 4 Ma to 39 ± 14 Ma (2σ). Ratios of Th/U in the 1568 Ma grain = 0.70, and is comparable with the ratios of 0.38-1.03 in the 'young' population.

4.4 Discussion

4.4.1 Trace-element Geochemistry

Although the absolute major and trace-element concentrations vary between samples, the chondrite-normalised patterns are similar for all five sandstones, indicating that the zircons in the sedimentary rocks from across the island were all derived from a similar oceanic rock type. All of the zircons have a pronounced positive Ce anomaly. When Ce^{3+} is oxidised to Ce^{4+} it behaves similar to Zr or Hf, thus is preferentially incorporated by zircon over the LREE's. Similarly, Eu^{3+} is more compatible than Eu^{2+}, The slightly negative Eu anomalies are suggestive of fractionation of plagioclase in the magma (Belousova et al., 2001).

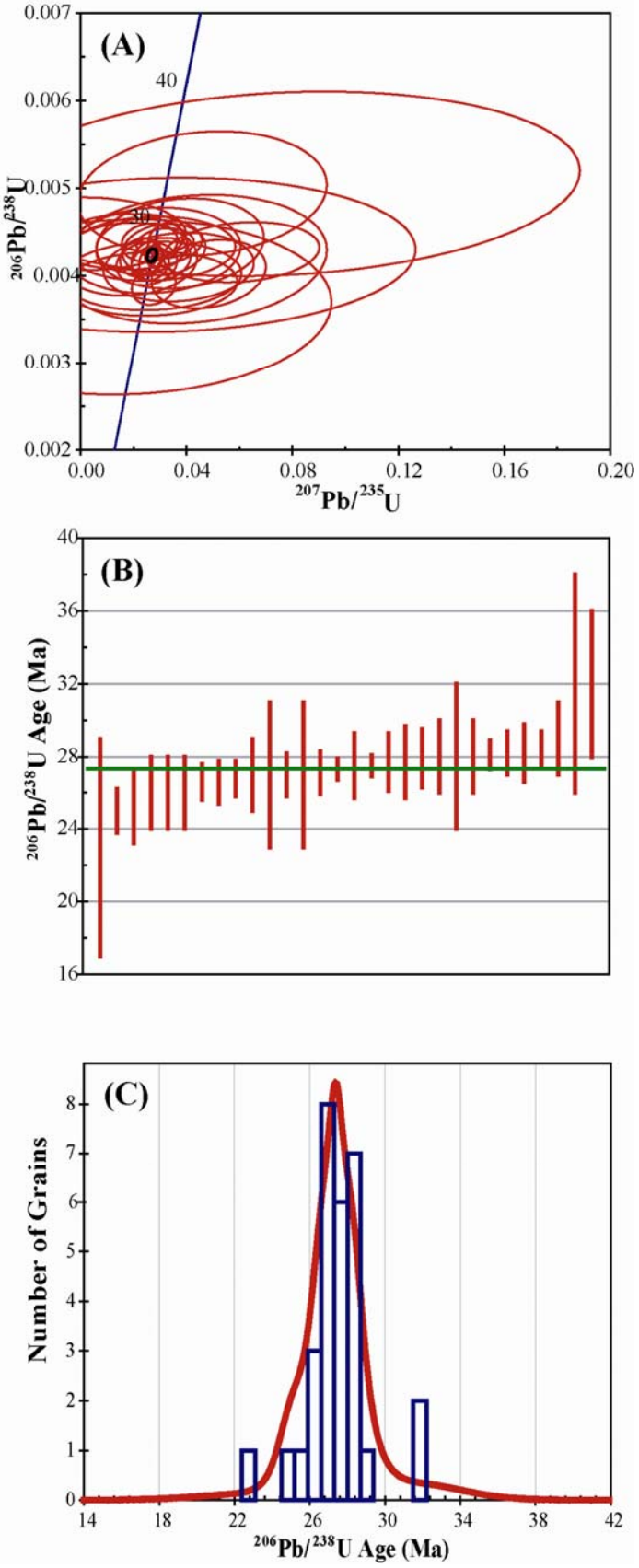

Figure 4.5 Sample DLP1b-5a (n = 30). (A) Concordia plot (B) Weighted average diagram: Weighted mean by data-point errors = 27.32 ± 0.34 Ma (2σ), MSWD = 2 and probability = 0.002. Error bars are 2σ. (C) $^{206}Pb/^{238}U$ age distribution.

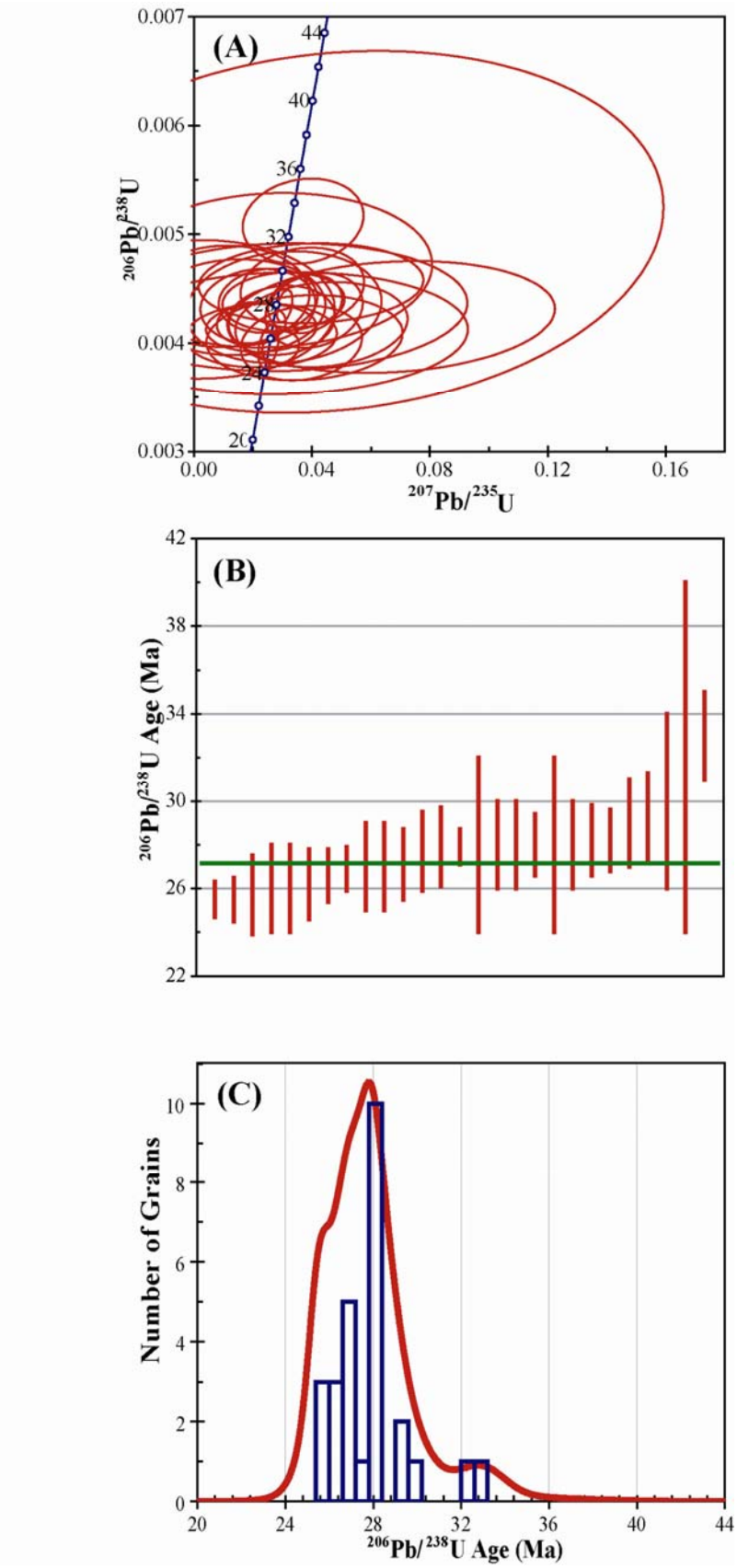

Figure 4.6 Sample MW6-2 (n = 27). (A) Concordia plot (B) Weighted average diagram: Weighted mean by data-point errors = 27.16 ± 0.57 Ma (2σ), MSWD = 3.6 and probability = <0.001. Error bars are 2σ. (C) $^{206}Pb/^{238}U$ age distribution.

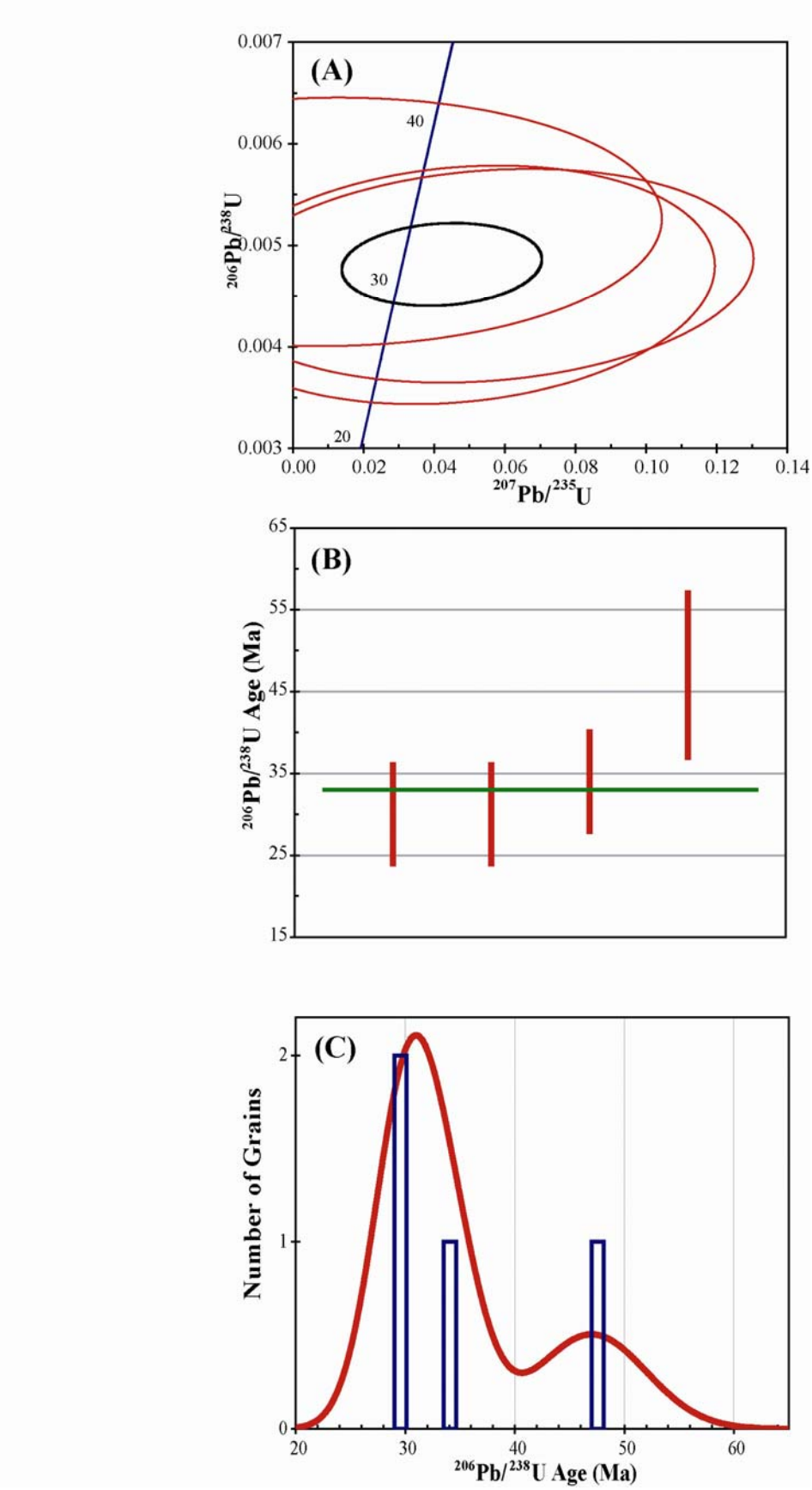

Figure 4.7 Sample MP1-4 (n = 4). (A) Concordia plot (B) Weighted average diagram: Weighted mean by data-point errors = 33 ± 9.5 Ma (2σ), MSWD = 3.3 and probability = 0.019. Error bars are 2σ. (C) $^{206}Pb/^{238}U$ age distribution.

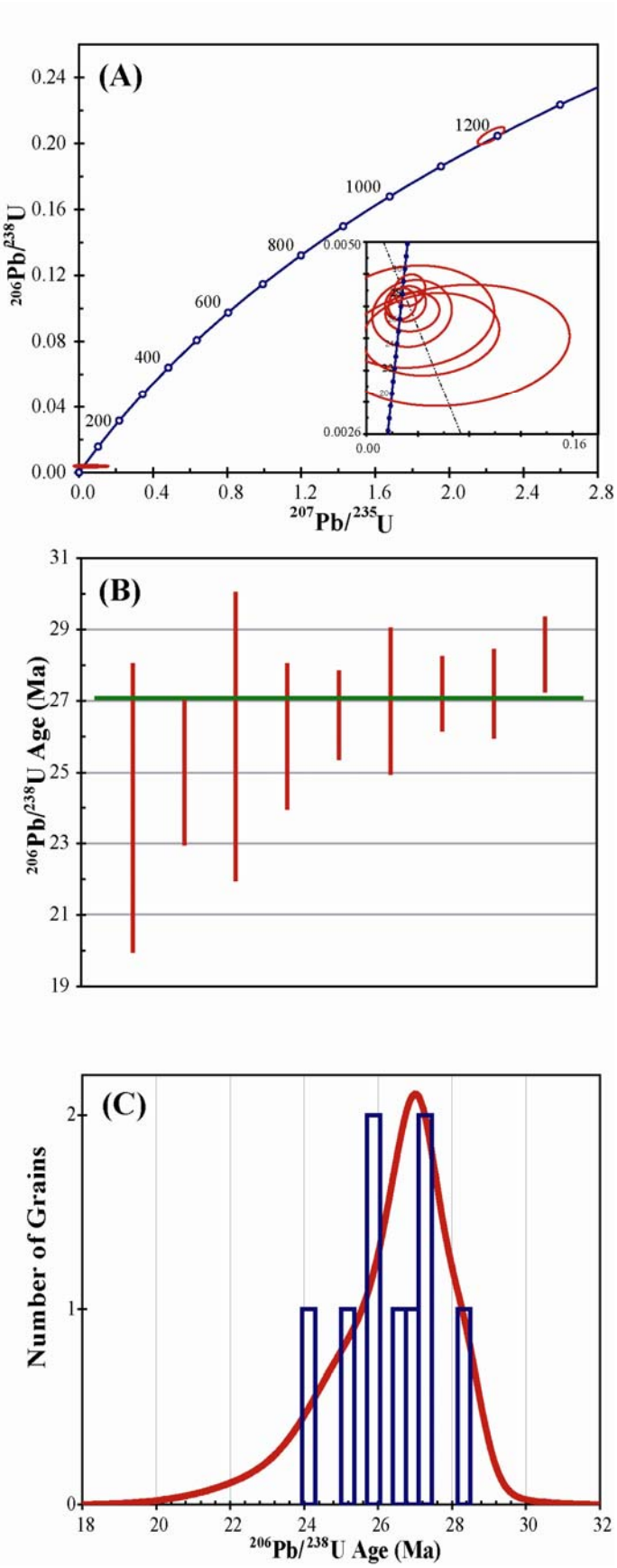

Figure 4.8 Sample MM1-1 (n = 10). (A) Concordia plot, inset shows 'young' population (n = 9) (B) Weighted average diagram of the 'young' population: Weighted mean by data-point errors = 27.08 ± 0.76 Ma (2σ), MSWD = 1.9 and probability = 0.062. Error bars are 2σ. (C) $^{206}Pb/^{238}U$ age distribution.

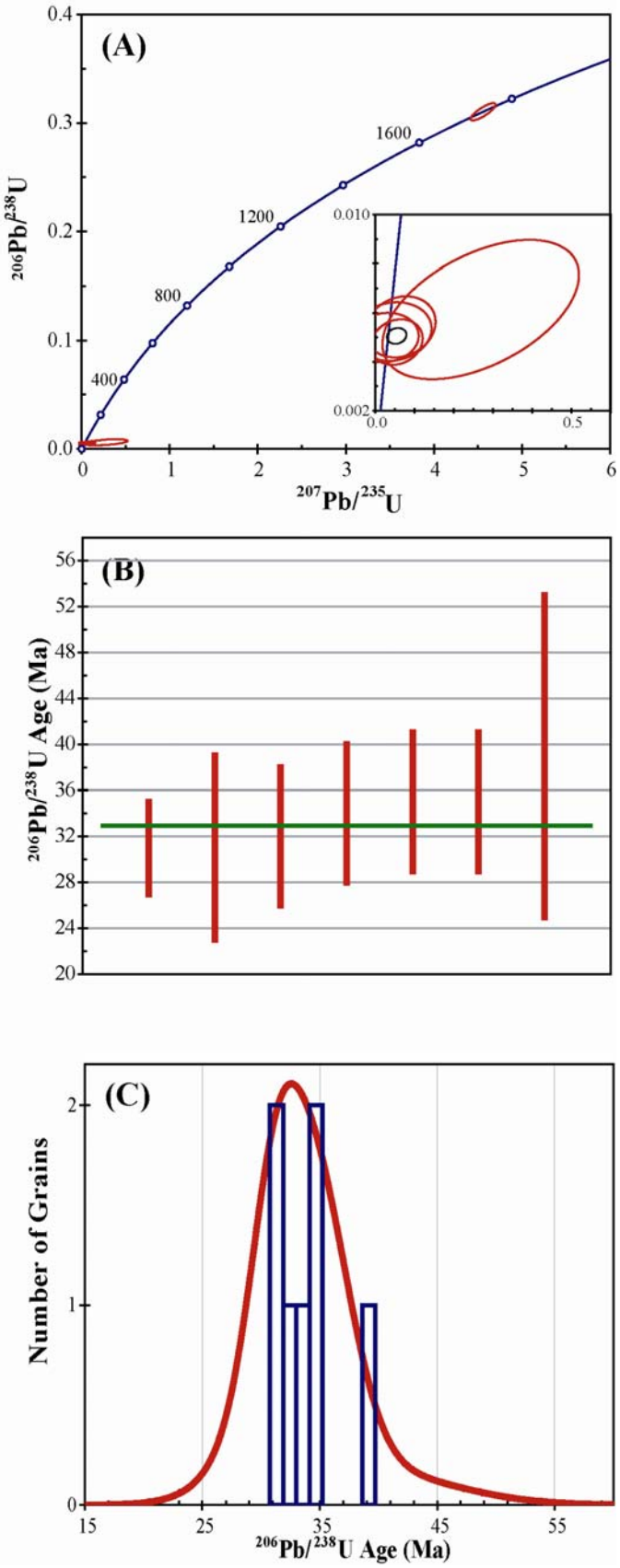

Figure 4.9 Sample CP1-2 (n = 8). (A) Concordia plot, inset shows 'young' population (n = 7) (B) Weighted average diagram of the 'young' population: Weighted mean by data-point errors = 32.9 ± 2.2 Ma (2σ), MSWD = 0.52 and probability = 0.8. Error bars are 2σ. (C) $^{206}Pb/^{238}U$ age distribution.

When plotted on the rock type discrimination diagrams (Figure 4.4) using fields by Belousova et al. (2002), the samples do not plot within the main array of continental crust zircons, and appear to form a tight cluster outside of this array. Comparing the data from this study with zircon data from oceanic gabbro (Kaczmarek et al., 2008), the two datasets overlap. The similar trace-element characteristics of the two datasets suggests that although zircon is rare in mafic rocks, the processes that allowed saturation of zirconium and crystallisation of zircon in these two mid-ocean ridge settings are likely to be similar.

4.4.2 U-Pb Geochronology

The new U-Pb data provides geochronological constraints on the ages of the source rocks for the zircons. The age of the main population of detrital zircons yielded ages of ~27 Ma, which is *ca* 20 Ma older than published ages of the island (Chapter 1). The provenance of the zircons must therefore involve much older crust. This demonstrates a significantly more distal provenance than has previously been proposed for these sedimentary rocks. A total lack of appropriately aged zircons excludes Macquarie Island as the source of the zircons. In addition, this lack of appropriately aged zircons suggests that the remainder of the sediment is also unlikely to have been locally derived from the island itself.

The unusual Proterozoic aged zircons are unlikely to have been derived from oceanic crust as they are far older than the adjacent oceanic crust. These anomalous ages may represent contamination during the zircon separation process. However, Proterozoic aged zircons were found in two sandstone samples that were separated at different times and perhaps limit the likelihood of this scenario. An alternate idea is that these Proterozoic aged zircons were ice-rafted from Antarctica where Proterozoic continental crust is common. Rare beach cobbles of metamorphic rocks on Macquarie Island have been interpreted to be from grounded icebergs that supports this idea.

Two likely sources of the dominantly Oligocene population of oceanic derived zircon clasts include: (i) Proto-Macquarie Spreading Ridge (PMSR) crust and (ii) South East Indian Ridge crust (SEIR). The nearest appropriately aged PMSR crust is >200 km along the spreading corridor, whilst the nearest appropriately aged SEIR crust is <35 km to the west. The proximity of SEIR crust makes it a more likely candidate.

Chapter 5 Provenance Model and Conclusions

5.1 Introduction

The lithostratigraphy, petrography, clinopyroxene geochemistry and detrital zircon geochemistry and geochronology have been described and discussed in the preceding chapters. This concluding chapter integrates the evidence from this study, and proposes a provenance model that is consistent with the tectonic setting at the time of sandstone deposition. Recommendations for further work are also presented at the end of this chapter.

5.2 Tectonic Overview

The tectonic evolution of the Australian-Pacific plate boundary is complex. Seafloor spreading at the Proto-Macquarie Spreading Ridge (PMSR) experienced a 60-90˚ change in spreading direction since 40 Ma, resulting in the transition from seafloor spreading to a transform plate boundary (Mosher and Massell-Symons, 2008). Changes to subsequent plate motions resulted in transpression at the plate boundary today.

The isotope geochronology of Macquarie Island crust and microfossil paleontology of pelagic oozes interstitial to pillow basalt indicate a 6-12 Ma age of seafloor spreading that formed the island at the PMSR (Chapter 1). Dijkstra and Cawood (2004) suggest that Macquarie Island crust grew from the base up. Peridotites cooled first, into which gabbro plutons were intruded, followed by cooling, deformation and intrusion of dolerite dykes that fed a sheeted dolerite dyke-basalt complex. The age of the gabbroic intrusions, determined at ~8 Ma (Armstrong et al., 2004; Murphy et al., 2008) and basalt glass ages of ~6 Ma (Wertz, 2003) support this base-up oceanic crust model, and suggest that the majority of Macquarie Island crust and the volcanic and sedimentary units formed toward the younger end of the 6-12 Ma age spectrum.

Plate tectonic reconstructions (Meckel, 2003) show that the Australian-Pacific plate boundary had largely transitioned into a through-going transform by 5.9 Ma (Figure 1.2). The crust of Macquarie Island therefore formed at the very end of seafloor spreading along the PMSR. Mosher and Massell-Symons (2008) suggest that only three PMSR spreading ridge segments of the original thirteen were still active by 5.9 Ma. Figure 5.1 shows the widths of the three spreading ridge segments were 5 km (A4/P4 – A5/P5), 21 km (A7/P7 – A8/P8) and 48 km long (A2/P2 – A4/P4). The segments were

offset by 160 and 117 km long transforms. Much longer offset transforms linked the A7/P7 – A8/P8 and A2/P2 – A4/P4 corridors to the New Zealand continental transform and Australia-Antarctic-Pacific triple junction respectively (Figure 5.1). Macquarie Island formed in the 48 km wide A2/P2 – A4/P4 corridor.

5.3 Provenance Model

The key indicator of the provenance of the sedimentary rocks of this study includes the U-Pb geochronology and trace-element geochemistry of detrital zircon (Chapter 4). This dataset demonstrates a significantly more distal provenance than has previously been proposed for these sedimentary rocks (Daczko et al., 2005) and excludes the island as the source of the zircons. Overlapping detrital zircon REE patterns (Chapter 4) indicate the zircons in the sedimentary rocks from across the island were all derived from a similar oceanic rock type. The most proximal crust of the appropriate age (~27 Ma) is crust that formed at the South East Indian Ridge (SEIR) on the western side of the Australia-Pacific plate boundary (Figure 5.1). This interpretation permits a provenance model whereby oceanic crust that formed at the SEIR ~20 Ma prior is shed towards the active A2/P2 – A4/P4 corridor of the PMSR and becomes interbedded with mid-ocean ridge volcanic rocks.

The geochemistry of detrital clinopyroxene clasts shows little overlap with clinopyroxene grains within the interbedded volcanic sequences. This observation excludes the proximal volcanism as a likely source for the sediment. Additionally, the geochemistry of detrital clinopyroxene clasts lacks a peridotite signature (high Mg #, low Ti), excluding the upper mantle as a likely source. Clasts of dolerite and gabbro are present within the sedimentary units, implying that these rock types provide at least one component of the likely source. This is supported further by overlapping geochemical affinities between clinopyroxene grains from the lower crustal gabbro and sheeted dolerite dyke sequences from Macquarie Island with the clinopyroxene clasts in the sedimentary rocks. The detrital zircon ages exclude the island itself as a likely source for the zircon clasts; however the island itself cannot be excluded as a potential source for the detrital clinopyroxene. Nonetheless, the most likely source of both the detrital zircon and clinopyroxene is the adjacent SEIR gabbro and sheeted dolerite dyke complex.

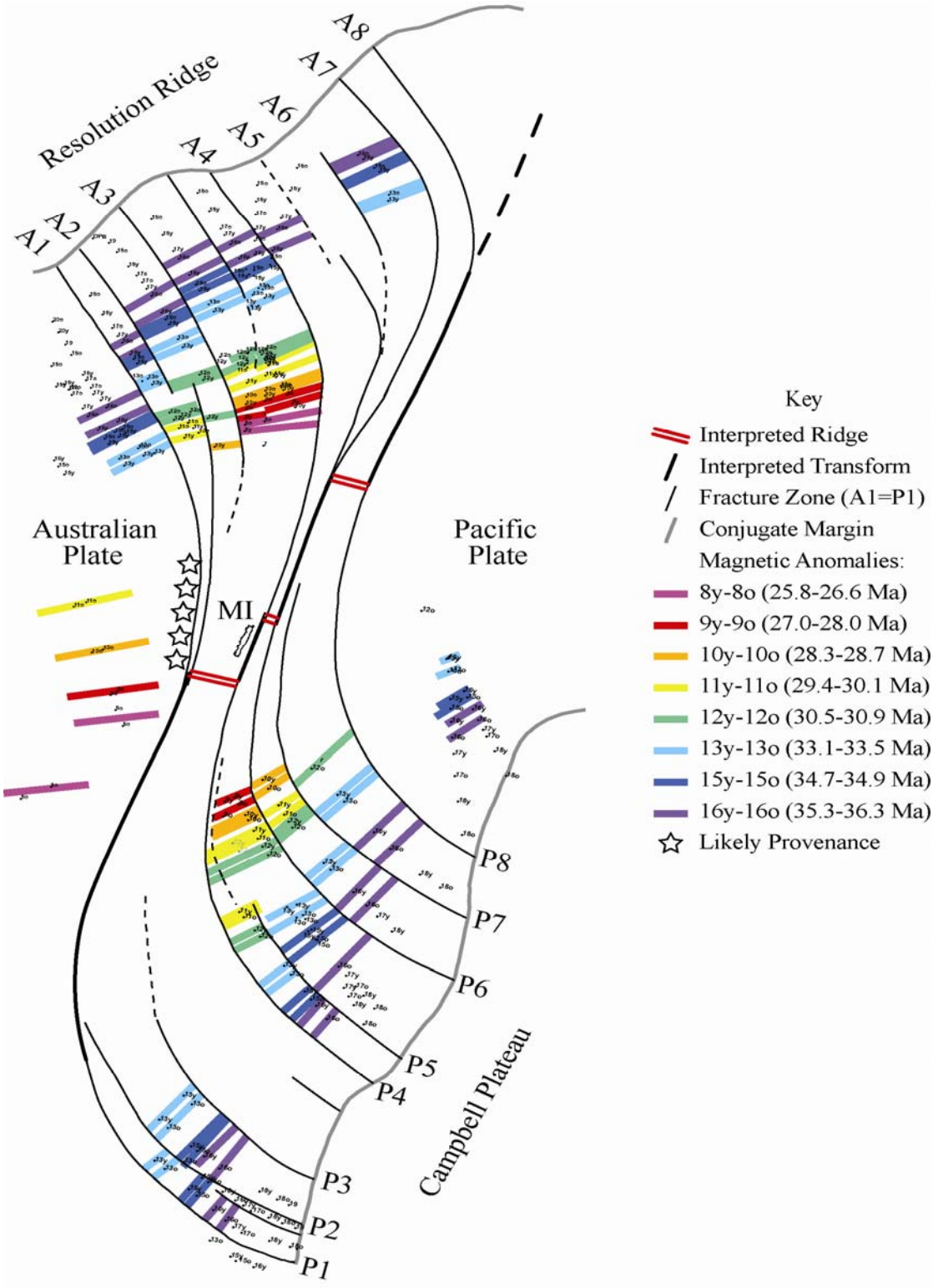

Figure 5.1 Reconstruction of arcuate fracture zones on the Australian and Pacific plates at 6 Ma prior to ~200 km of dextral transform motion along the Australian-Pacific plate boundary. Numbered fracture zones are from Massell et al. (2000), Meckel et al. (2003) and Keller, (2004). The reconstruction was produced using PLATES reconstruction software (University of Texas at Austin, Unit for Geophysics) and the Cande and Stock (2004) finite poles of rotation. Input data also included the Resolution Ridge and Campbell Plateau conjugate margins and magnetic anomalies for the region (Keller, 2004). MI = Macquarie Island. The locations of the three spreading ridge segments are estimated by placing them halfway between the two conjugate margins within the three active spreading corridors identified by Mosher and Symons-Massell, (2008).

The mineralogy of the sandstones is consistent with a fault-scarp derived provenance. The unusually large volume of sediment exposed on Macquarie Island suggests a large fault, such as a plate boundary scale transform fault, was required in order to produce that much sediment. The long offset transform that links the A2/P2 – A4/P4 corridor to the Australia-Antarctic-Pacific triple junction is the most proximal and therefore most likely transform fault. The classic Bouma sequences examined here indicate that the sediment was transported by turbidity flows, with palaeo-current indicators suggesting an offshore southerly source.

The main limitation of this model is the age difference between the crust formed at the SEIR and the active PMSR (~20 Ma). It would be expected that the older and colder SEIR crust would be significantly bathymetrically deeper than the active PMSR. This negates the gravitational potential energy required to drive a turbidity flow from the SEIR crust toward the PMSR.

However, the PMSR was in the waning stages of seafloor spreading at the time that the crust of Macquarie Island formed. The dwindling magmatic activity at the PMSR most likely indicates the spreading ridge was atypically cold, and therefore uncharacteristically bathymetrically deep. Additionally, Meckel et al. (2005) propose that the development of the irregular bathymetry of the MRC commenced prior to the formation of Macquarie Island crust. These authors show a relationship between the amount of boundary normal convergence (transpression) over time and topographic development of the Macquarie Ridge Complex (MRC), and suggest that transpression along the long-offset transforms at the latitude of Macquarie Island coincided with the waning stages of spreading at the PMSR, with some segments still actively spreading whilst others were being uplifted. Therefore, the unusual tectonic setting of Macquarie Island may have involved uplifted SEIR crust adjacent to the waning PMSR, permitting sediment from the developing MRC to be shed towards the active PMSR, resulting in interbedded PMSR volcanic rocks with sediment partly derived from the SEIR.

5.4 Further Research

This research project represents the first geochemical provenance study conducted on the Macquarie Island sandstones, and as such, could benefit from additional research:

- Determination of the radiometric ^{40}Ar-^{39}Ar ages of basalts interbedded with sedimentary rocks, which will constrain the age of sediment deposition.
- Expand the detrital zircon geochronology and trace-element database.
- Determine Hf isotopic compositions of the zircons to investigate the origin of the host magma.
- Expand the clinopyroxene major and trace-element database to include lower oceanic crustal units from the northern third of the island.
- Conducting geochemical analyses of other heavy minerals such as spinel group minerals and ilmenite.

Appendix A Clinopyroxene Major Elements

Appendix B Other Mineral Major Elements

Appendix C Clinopyroxene Trace-elements

Appendix D Zircon Major Elements

Appendix E Zircon Trace-elements

Appendix F Zircon U-Pb Ages

References

Anderson, T., 2002, Correction of common-lead in U-Pb analyses that do not report ^{204}Pb: Chemical Geology, v. 192, p. 59-79.

Armstrong, R.A., Kohn, B., Goscombe, B.D., and Everard, J.L., 2004, U-Pb fission track ages from oceanic crust at Macquarie Island: Abstracts - Geological Society of Australia, v. 73, p. 197.

Beccaluva, L., Macciotta, G., Piccardo, G.B., and Zeda, O., 1989, Clinopyroxene composition of ophiolite basalts as petrogenetic indicator: Chemical Geology, v. 77, p. 165-182.

Belousova, E.A., Griffin, W.J., Shree, S.R., Jackson, S.E., and O'Reilly, S.Y., 2001, Two age populations of zircons from the Timber Creek kimberlites, Northern Territory, as determined by laser-ablation ICP-MS analysis: Australian Journal of Earth Sciences, v. 48, p. 757-765.

Belousova, E.A., Griffin, W.L., O'Reilly, S.Y., and Fisher, N.I., 2002, Igneous zircon: trace element composition as an indicator of source rock type: Contributions to Mineralogy and Petrology, v. 143.

Bhatia, M.R., and Crook, K.A.W., 1986, Trace element characteristics of graywackes and tectonic setting discrimination of sedimentary basins: Contributions to Mineralogy and Petrology, v. 92, p. 181-193.

Black, L.P., and Gulson, B.L., 1978, The age of the Mud Tank carbonatite, Strangways Range, Northern Territory: BMR Journal of Australian Geology and Geophysics, v. 3, p. 227–232.

Bouma, A.H., 1962, Sedimentology of some Flysch deposits; a graphic approach to facies interpretation: Amsterdam, Elsevier, 168 p.

Cande, S.C., and Stock, J.M., 2004, Pacific-Antarctic-Australia motion and the formation of the Macquarie Plate: Geophysical Journal International, v. 157, p. 399-414.

Cawood, P.A., 1983, Modal composition and detrital clinopyroxene geochemistry of lithic sandstones from the New England Fold Belt (east Australia): A Paleozoic forarc terrane: Geological Society of America Bulletin, v. 94, p. 1199-1214.

Christodoulou, C., Griffin, B.J., and Foden, J., 1984, The Geology of Macquarie Island: Australian National Antarctic Research Expeditions Research Notes v. 21, p. 15.

Daczko, N.R., Mosher, S., Coffin, M.F., and A., M.T., 2005, Tectonic implications of fault-scarp-derived volcaniclastic deposits on Macquarie Island: Sedimentation at a fossil ridge-transform intersection?: Geological Society of America Bulletin, v. 117, p. 18-31.

Daczko, N.R., Wertz, K.L., Mosher, S., Coffin, M.F., and Meckel, T.A., 2003, Extension along the Australian-Pacific transpressional transform plate boundary near Macquarie Island, Geochemistry Geophysics Geosystems, Volume 4.

Dickinson, W.R., and Suczek, C., 1979, Plate tectonics and sandstone compositions: American Association of Petroleum Geologists Bulletin, v. 63, p. 2164-2182.

Dijkstra, A.H., and Cawood, P., 2004, Multiple stages of magmatic ocean crust formation and extensional deformation in the Macquarie Island 'Ophiolite': Abstracts - Geological Society of Australia, v. 73, p. 205.

Duncan, R.A., and Varne, R., 1988, The Age and Distribution of the Igneous Rocks of Macquarie Island: Papers and Proceedings of the Royal Society of Tasmania, v. 122, p. 45-50.

Garzanti, E., Andò, S., and Scutellà, M., 2000, Actualistic Ophiolite Provenance: The Cyprus Case: The Journal of Geology, v. 108, p. 199-218.
Garzanti, E., Scutellà, M., and Vidimari, C., 1998, Provenance from ophiolites and oceanic allochtons: modern beach and river sands from Liguria and the Northern Apennines (Italy): Ofioliti, v. 23.
Garzanti, E., Vezzoli, G., and Andò, S., 2002, Modern Sand from Obducted Ophiolite Belts (Sultanate of Oman and United Arab Emirates): The Journal of Geology, v. 110, p. 371-391.
Goscombe, B., and Everard, J., 2001, Tectonic evolution of Macquarie Island: extensional structures and block rotations in oceanic crust: Journal of Structural Geology, v. 23, p. 639-673.
Goscombe, B.D., and Everard, J.L., 1998, Geology of Macquarie Island. Sheets 1-7, Geological Atlas 1:10,000 series: Hobart, Australia, Mineral Resources Tasmania, Australian Antarctic Division.
Griffin, B.J., 1982, Igneous and Metamorphic Petrology of Lavas and Dykes of the Macquarie Island Ophiolite Complex: Hobart, University of Tasmania.
Griffin, B.J., and Varne, R., 1980, The Macquarie Island Ophiolite Complex: Mid-tertiary Oceanic Lithosphere from a Major Ocean Basin: Chemical Geology, v. 30, p. 285-308.
Hutchinson, C.S., 1975, Laboratory Handbook of Petrographic Techniques, p. 1-527.
Jackson, S.E., Pearson, N.J., Griffin, W.J., and Belousova, E.A., 2004, The application of laser ablation-inductively coupled plasma-mass spectrometry to in situ U-Pb zircon geochronology: Chemical Geology, v. 211, p. 47-69.
Kaczmarek, M.A., Müntener, Æ.O., and Rubatto, Æ.D., 2008, Trace element chemistry and U–Pb dating of zircons from oceanic gabbros and their relationship with whole rock composition (Lanzo, Italian Alps): Contributions to Mineralogy and Petrology, v. 155.
Kamenetsky, V.S., Everard, J.L., Crawford, A.J., Varne, R., Eggins, S.M., and Lanyon, R., 2000, Enriched End-member of Primitive MORB Melts: Petrology and Geochemistry of Glasses from Macquarie Island (SW Pacific): Journal of petrology, v. 41, p. 411-430.
Keller, W., 2004, Cenozoic plate tectonic reconstructions and plate boundary processes in the Southwest Pacific: Pasadena, California Institute of Technology.
Krawinkel, H., Wozazek, S., Krawinkel, J., and Hellmann, W., 1999, Heavy-mineral analysis and clinopyroxene geochemistry applied to provenance analysis of lithic sandstones from the Azuero–Sona´ Complex (NW Panama): Sedimentary Geology, v. 24, p. 149-168.
Le Bas, M.J., Le Maitre, R.W., Streckeisen, A., and Zanettin, B., 1986, A chemical classification of volcanic rocks based on the total alkali-silica diagram: Journal of Petrology, v. 27, p. 745-750.
Lindsley, D.H., 1983, Pyroxene Thermometry: American Mineralogist, v. 68, p. 477-493.
Ludwig, K.R., 2000, Isoplot - a geochronological toolkit for Microsoft Excel: Berkeley Geochronology Centre Special Publication 1a.
Massell, C., Coffin, M.F., Mann, P., Mosher, S., Frohlich, C., Duncan, C.S., Karner, G., Ramsay, D., and Lebrun, J.F., 2000, Neotectonics of the Macquarie Ridge Complex, Australia-Pacific plate boundary: Journal of Geophysical Research, v. 105, p. 13,457-13,480.

Meckel, T.A., 2003, Tectonics of the Hjort region of the Macquarie Ridge Complex, southernmost Australian-Pacific Plate Boundary, southwest Pacific Ocean: Austin, University of Texas.

Meckel, T.A., Coffin, M.F., Mosher, S., Symonds, P., Bernardel, G., and Mann, P., 2003, Underthrusting at the Hjort Trench, Australian-Pacific plate boundary: Incipient subduction?: Geochemistry, Geophysics, Geosystems, v. 4.

Meckel, T.A., Mann, P., Mosher, S., and Coffin, M.F., 2005, Influence of cumulative convergence on lithospheric thrust fault development and topography along the Australian-Pacific plate boundary south of New Zealand: Geochemistry, Geophysics, Geosystem, v. 6, p. 1-20.

Morimoto, N., Fabries, J., Ferguson, A.K., Ginzburg, I.V., Ross, M.F., Seifert, A., Zussman, J., Aoki, K., and Gottardi, G., 1988, Nomenclature of pyroxenes: American Mineralogist, v. 73, p. 1123-1133.

Morton, A., and Hallsworth, C., 1999, Processes controlling the composition of heavy mineral assemblages in sandstones: Sedimentary Geology, v. 124, p. 3-29.

Morton, A.C., and Hallsworth, C.R., 1994, Identifying provenance specific features of detrital heavy mineral assemblages in sandstones: Sedimentary Geology, v. 90, p. 241–256.

Mosher, S., and Massell-Symons, C., 2008, Ridge reorientation mechanisms: Macquarie Ridge Complex, Australia Pacific plate boundary: The Geological Society of America, v. 36, p. 119-122.

Murphy, M.J., Portner, R.A., Daczko, N., Dickinson, J., and Allchurch, S., 2008, Provenance of ophiolitic sand: comparison of ancient and modern sand, Australian Earth Sciences Convention: Perth, Australia.

Norman, M.D., Griffin, W.L., Pearson, N.J., Garcia, M.O., and O'Reilly, S.Y., 1998, Quantitative analysis of trace element abundances in glasses and minerals: a comparison of laser ablation ICPMS, solution ICPMS, proton microprobe, and electron microprobe data: Journal of Analytical Atomic Spectroscopy, v. 13, p. 477-482.

Norman, M.D., Pearson, N.J., Sharma, A., and Griffin, W.L., 1996, Quantitative Analysis of Trace Elements in Geological Materials by Laser Ablation ICPMS: Instrumental Operating Conditions and Calibration Values of NIST Glasses: Geostandards Newsletter, v. 20, p. 247–261.

Norrish, K., and Hutton, J.T., 1969, An accurate X-ray spectrographic method for the analysis of a wide range of geological samples: Geochimica et Cosmochimica Acta, v. 33.

Pearce, J.A., and Norry, M.J., 1979, Petrogenetic Implications of Ti, Zr, Y, and Nb variations in Volcanic Rocks: Contributions to Mineralogy and Petrology, v. 69, p. 33-47.

Pouchou, J.L., and Pichoir, F., 1984, A new model for quantitative X-ray microanalysis of homogeneous samples: Recherche Aerospatiale, v. 5, p. 13-38.

Quilty, P., and Crundwell, M., 2004, The age of seafloor spreading that formed the foundation rocks of Macquarie Island: Abstracts - Geological Society of Australia, v. 73, p. 220.

Quilty, P.G., Rubenach, M., and Wilcoxon, J.A., 1973, Miocene Ooze from Macquarie Island: Search, v. 4, p. 163-164.

Sun, S.S., and McDonough, W.F., 1989, Chemical and isotopic systematics of oceanic basalts: implications for mantle composition and processes, Geological Society of London Special Publication, 313-345 p.

—, 1995, The composition of the earth: Chemical Geology, v. 120, p. 223-253.

van Achterbergh, E., Ryan, C.G., and Griffin, W.L., 1999, GLITTER: On-line interactive data reduction for the laser ablation ICPMS microprobe, The 9th V. M. Goldschmidt Conference: Massachusetts, Cambridge, p. 305.

Varne, R., Brown, A.V., and Falloon, T., 2000, Macquarie Island: Its geology, structural history, and the timing and tectonic setting of its N-MORB to E-MORB magmatism: Geological Society of America Special Oaper, v. 349, p. 301-320.

Varne, R., Gee, R.D., and Quilty, P., 1969, Macquarie Island and the Cause of Oceaninc Linear Magnetic Anomalies: Science, v. 166, p. 230-233.

Wertz, K., 2003, From seafloor spreading to uplift: The structural and geochemical evolution of Macquarie Island on the Australian-Pacific plate boundary: Austin, University of Texas.

Wiedenbeck, M., Allé, P., Corfu, F., Griffin, W.L., Meier, M., Oberli, F., von Quadt, A., Roddick, J.C., and Spiegel, W., 1995, Three natural zircon standards for U–Th–Pb, Lu–Hf, trace element and REE analyses: Geostandards and Geoanalytical Research, v. 19, p. 1-23.

Wiedenbeck, M., Hanchar, J.M., Peck, W.H., Sylvester, P., Valley, J., Whitehouse, M., Kronz, A., Morishita, Y., Nasdala, L., Fiebig, J., Franchi, I., Girard, J.P., Greenwood, R.C., Hinton, R., Kita, N., Mason, P.R.D., Norman, M., Ogasawara, M., Piccoli, P.M., Rhede, D., Satoh, H., Schulz-Dobrick, B., Skår, O., Spicuzza, M.J., Terada, K., Tindle, A., Togashi, S., Vennemann, T., Xie, Q., and Y.F., Z., 2004, Further Characterisation of the 91500 Zircon Crystal Geostandards and Geoanalytical Research, v. 28, p. 9-39.